

University of Warwick institutional repository: <http://go.warwick.ac.uk/wrap>

A Thesis Submitted for the Degree of PhD at the University of Warwick

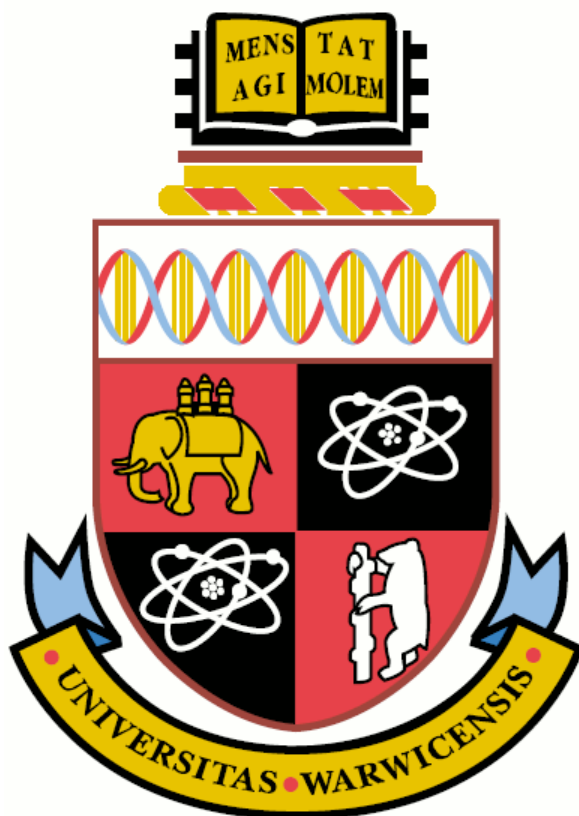
<http://go.warwick.ac.uk/wrap/66078>

This thesis is made available online and is protected by original copyright.

Please scroll down to view the document itself.

Please refer to the repository record for this item for information to help you to cite it. Our policy information is available from the repository home page.

Transient Absorption Studies of Biologically Relevant Systems; Photostability and Photoactivation



Simon Edward Greenough

Submitted in partial fulfilment of the qualification of

Doctor of Philosophy in Chemistry

The University of Warwick

October 2014

List of Contents

List of Figures.....	v
List of Tables.....	ix
Acknowledgements.....	x
Declaration.....	xi
Abstract.....	xii
Chapter 1: Introduction	1
1.1. Overview	2
1.2. The Fates of Excited States	3
1.2.1. Radiative Processes	4
1.2.2. Non-Radiative Vibrational Energy Transfer.....	6
1.2.3. Internal Conversion and Intersystem Crossing.....	9
1.2.4. Photodissociation.....	10
1.3. Femtochemistry.....	10
1.3.1. Born-Oppenheimer Approximation	10
1.3.2. Franck-Condon Principle.....	12
1.3.3. Wavepackets.....	14
1.3.4. Electronic State Degeneracy.....	15
1.4. Pump-Probe Spectroscopy.....	18
1.4.1. Ultrafast Transient Absorption Spectroscopy.....	18
1.4.2. Time-Resolved Photoelectron Imaging Spectroscopy	22
1.5. Photostability in Biologically Relevant Molecules.....	23
1.5.1. Introduction.....	23
1.5.2. Phenol	24
1.6. Photoactivation for Therapy	29
1.6.1. Introduction.....	29
1.6.2. Tris(bipyridine)ruthenium(II) chloride.....	29
1.6.3. Photoactive Ruthenium Complexes.....	30
1.7. Bibliography	32
Chapter 2: Experimental.....	37
2.1. The Laser System Overview.....	38

2.2.	Generation of Ancillary Light.....	39
2.2.1.	Nonlinear Optical Transformations	39
2.3.	The TA Setup	43
2.3.2.	Table Layout.....	43
2.3.3.	Broadband White-Light Probe.....	45
2.3.4.	Pump Sources.....	49
2.3.5.	Optics.....	51
2.3.6.	Optomechanics	52
2.3.7.	Sample Delivery.....	54
2.3.8.	System Control, Data Acquisition and Analysis.....	58
2.3.9.	Optimisation and Accreditation	61
2.4.	Bibliography	66
Chapter 3: Photochemistry of Guaiacol		67
3.1.	Introduction.....	68
3.2.	Methods.....	70
3.3.	Results and Discussion	70
3.3.1.	Transient Absorption Spectroscopy.....	70
3.3.2.	Kinetic Fitting Procedure.....	74
3.4.	Time-Resolved Photoelectron Imaging.....	79
3.5.	Conformer Specific Photodissociation Dynamics	81
3.6.	Conclusions.....	87
3.7.	Bibliography	88
Chapter 4: Photoactivation of <i>cis</i>-[Ru(bipyridine)₂(nicotinamide)₂]²⁺		91
4.1.	Introduction.....	92
4.2.	Methods.....	93
4.3.	Results and Discussion	93
4.3.1.	Static UV/Vis Absorption Spectra.....	93
4.3.2.	TAS.....	96
4.3.3.	Target Analysis of TAS.....	101
4.3.4.	Kinetic Model for Dissociation of <i>cis</i> -[Ru(bpy) ₂ (NA) ₂] ²⁺	103
4.3.5.	Kinetic Analysis	109
4.3.6.	Quantum Yields	111

4.3.7. Formation and Relaxation Dynamics of the Intermediate $[\text{Ru}(\text{bpy})_2(\text{NA})]^{2+}$	113
4.4. Conclusions.....	119
4.5. Bibliography	120
Chapter 5: Conclusion and Outlook	123
5.1. Summary	124
5.2. Outlook.....	126
5.2.1. Photostability in Biomolecules	126
5.2.2. Photoactivation of Transition Metal Complexes	126
5.3. Bibliography	127
Appendix A: List of Abbreviations	a
Appendix B: Chapter 3 Methodology	c
Gas Phase Methods.....	c
Theoretical Calculations	d
Bibliography.....	e
Appendix C: Chapter 4 Theory	f
Computational Methodology.....	f
TD-B3LYP Calculation Results.....	h
Bibliography.....	j

List of Figures

Figure 1.1 Jablonski diagram depicting molecular states and photophysical processes connecting them. The vertical positions of thick lines correspond to the electronic energy minima of electronic ground and excited states. Thin black lines correspond to vibrational levels. As is the convention, straight arrows refer to radiative transitions (cyan: absorption, green: fluorescence, red: phosphorescence), while curvy arrows depict non-radiative processes (orange: internal conversion, blue: intersystem crossing and violet: intramolecular vibrational relaxation). The width and position of lines on the abscissa have no physical connotation and are placed for aesthetics.....	4
Figure 1.2 PES along a single nuclear coordinate of initial and final electronic states. The Franck-Condon factor for the photoexcitation from $\Psi''v = 0$ is greatest for $\Psi'v = 4$. Photoemission from $\Psi'v = 0$ has the most favourable overlap with $\Psi''v = 1$	13
Figure 1.3 Energy of two convergent PES in the X_1 , X_2 branching space (grey shading) form a conical intersection.....	16
Figure 1.4 Quantum tunnelling of a wavefunction through a potential barrier along some nuclear separation u . In the bound region, u_0 - u_1 , a normal harmonic wavefunction is observed. The classically forbidden region, <i>i.e.</i> the barrier u_1 - u_2 carries an exponential decay of the wavefunction that emerges on the second state, $>u_2$	17
Figure 1.5 Schematic showing how the two laser pulses are sent through the sample at pump-probe delay time t and the probe pulse is detected by the photodiode array.....	18
Figure 1.6 A typical TAS with the various contributions: 1. Ground-state bleach (ochre dashed line). 2. Stimulated emission (purple dashed line). 3. Excited-state absorption (blue dotted line). The sum of these contributions is shown in the solid red line.....	19
Figure 1.7 Calculated potential energy cuts along the O-H coordinate of phenol for the first two electronic excited states, S_1 and S_2 , and the ground state, S_0 . Excitation ($h\nu_{\text{pump}}$) to the S_1 is shown for four different excitation wavelengths (green, blue, red and orange arrows). The grey shaded area, labelled $V(u) - E$, represents the potential barrier to H-atom tunnelling used in WKB tunnelling calculations. Following H-atom tunneling under the S_1/S_2 CI and O-H fission along S_2 , H-atoms are probed using fs pulses ($h\nu_{\text{probe}}$). Figure taken from ref. 58.....	24
Figure 1.8 (a-c) TA spectra of 10 mM solution of phenol in cyclohexane following 267 nm irradiation at various pump-probe delays with (a) including solvent only TA spectra for 1, 200 and 800 ps. (d) Transients at select wavelengths and S_1 fluorescence lifetime obtained from time-correlated single photon counting experiment. Figure taken from ref. 66.	27
Figure 2.1 Schematic of the optical table containing the laser system and TOPAS.	38
Figure 2.2 Second order nonlinear optical process for generating pulses of new frequencies. (a) SFG, (b) DFG, (c) OPG.....	41
Figure 2.3 Illustration of the typical shape of a white-light continuum spectrum generated from the broadening of an IR seed pulse (dashed peak).	42
Figure 2.4 Schematic of the TA setup drawn to scale. Legend of labelled optics may be found in Section 2.3.5. PP – peristaltic pump.....	44

Figure 2.5 A summarized white-light continuum probe generation beam path. BS – beamsplitter, RR – retroreflector, $\lambda/2$ WP – half-waveplate, ND – neutral density filter, L – lens, SM – spherical mirror, F – filter,	45
Figure 2.6 A 25 mm translation stage mounted vertically translates the CaF_2 window continuously. From the position shown, the platform may move 25 mm (though only 12 mm is used) up before reversing direction.....	46
Figure 2.7 Pictures of WLC imaged on white card during optimisation, where a) and b) have too low a power density, c) is optimal and d) is over-pumped. <i>Nota bene</i> the red/purple halo around c) is not clear from this image and appears as a much fainter, perfectly symmetrical version of the halo seen in d).	48
Figure 2.8 Spectra of the filtered WLC and its RMS noise.....	49
Figure 2.9 Left: upper reservoir, right: wire-guided thin film liquid jet setup.....	55
Figure 2.10 IRFs of a film of methanol excited at 267 nm for four probe wavelengths.	62
Figure 2.11 Sample of GVD curve fitted from two photon artefact of pumping methanol at 266 nm.....	63
Figure 2.12 DCM - <i>trans</i> -4-dicyanomethylene-2-methyl-6- <i>p</i> -dimethyleaminostyryl-4H-pyran.	63
Figure 2.13 Time and energy resolved transient absorption in DCM in ethanol following excitation with 400 nm. Time zero not corrected.....	64
Figure 2.14 Fitted transients for DCM in ethanol at 620, 550, 500 and 450 nm. <i>Nota bene</i> the ΔOD axis has its polarity inverted i.e. $-\Delta\text{OD}$ (not the typical $+\Delta\text{OD}$).	65
Figure 2.15 TAS of phenol in cyclohexane at 2 ns after excitation with 267 nm.....	65
Figure 3.1 The structures of the two lowest energy conformers, A and B , of guaiacol.....	69
Figure 3.2 TAS of 25 mM guaiacol/cyclohexane solution at times: (a) <25 ps and (b) 25 ps to 8 ns. Solvent-alone scans at 25 ps (dark grey) and 2 ns (light grey).....	71
Figure 3.3 TAS of 25 mM guaiacol/methanol solution at times: (a) <25 ps and (b) 25 ps to 10 ns. Solvent-alone scans at 25 ps (dark grey) and 2 ns (light grey).....	73
Figure 3.4 TAS of 35 mM solution of guaiacol in chloroform recorded using a 100 μm path length Harrick flow-cell at 2 ns after 267 nm irradiation. Quenching of excited state through an electron transfer to solution process yields the absorption spectrum of the guaiacoxyl radical, in good accord with previous studies. ¹³	74
Figure 3.5 Kinetic traces for guaiacol/cyclohexane and guaiacol/methanol solutions from 0 to 2 ns, each fitted with a multi-exponential decay.....	75
Figure 3.6 Kinetic traces of the solvent response of methanol (blue) and cyclohexane (red), following excitation at 267 nm from 0 to 2 ns, each fit with biexponential decay functions.....	76
Figure 3.7 Kinetic traces of the methanol/guaiacol (blue) and cyclohexane/guaiacol (red), following excitation at 267 nm from 0 to 25 ps, each fit with tetraexponential decay functions (solid line). Dotted lines show the solvent component (the same as the fits in Figure 3.6). Dashed-dotted lines show the solute (guaiacol) component.....	77

Figure 3.8 Kinetic traces of the methanol/guaiacol (blue) and cyclohexane/guaiacol (red), following excitation at 267 nm from 25 to 2 ns, each fit with tetraexponential decay functions (solid line). Dotted lines show the solvent component (the same as the fits in Figure 3.6). Dashed-dotted lines show the solute (guaiacol) component.....	78
Figure 3.9 (a) Time-dependent photoelectron spectrum (b) its fit and (c) the associated residuals. Time axes are linear between ± 500 fs and then logarithmic to +100 ps.....	79
Figure 3.10 (a) DAS of the TRPEI data (vertical dashed line denotes the ionisation potential), (b) anisotropy parameter β_2 as a function of pump-probe delay, where error bars represent one standard deviation, and (b) (inset) right half: background-subtracted photoelectron image at a pump-probe time delay of 100 ps and left half: same image after Abel inversion performed using methods outlined in ref. 4. Time axis is linear to 500 fs and then logarithmic to +100 ps.	80
Figure 3.11 (a) Calculated PECs for the S_0 , S_1 and S_2 states of both conformer A (red) and B (blue) of guaiacol with respect to the O–H coordinate ($R_{\text{O-H}}$). PECs are calculated at the CASPT2(12,11)/aug-cc-pVTZ level of theory. (b) Rescaled PECs for the S_1 and S_2 states in A and B , such that the S_1 origin is set to 0 eV in both conformers. Following excitation ($h\nu$) to the S_1 state below the S_1/S_2 CI, excited state flux may proceed <i>via</i> either red arrows (no tunnelling) for conformer A or blue arrows (tunnelling) for conformer B . See main text for further details...	84
Figure 4.1 Static UV/Vis absorption spectra of $[\text{Ru}(\text{bpy})_2(\text{NA})]^{2+}$ (1 , orange), $[\text{Ru}(\text{bpy})_2(\text{NA})(\text{H}_2\text{O})]^{2+}$ (2 , cyan) and $[\text{Ru}(\text{bpy})_2(\text{H}_2\text{O})_2]^{2+}$ (3 , black). Irradiation of 1 with 465 nm for 50 s yields 2 . Further irradiation of 2 for 1 h 50 min yields 3 . Molecular structure of 1 is shown inset.....	92
Figure 4.2 Calculated static UV/Vis absorption spectra for (a) 1 , (b) 2 and (c) PCI, both in the gas phase (dotted lines) and with a H_2O PCM (solid lines). Calculated ground state structures shown inset. Spectra were calculated at the TD-B3LYP level of theory using a 28 electron SDD ECP for Ru and a cc-pVTZ basis set for C, O, N and H atoms. Calculated spectra were generated by convolution of the calculated squared transition dipole moments (TDM ²) for singlet excitations with Gaussian functions (50 nm FWHM). Experimentally measured spectra for 1 and 2 from Figure 4.1 are shown in panels (a) and (b), respectively, for comparison (dashed-dotted lines)....	95
Figure 4.3 UV/Vis TAS of 890 μM aqueous solution of 1 over pump-probe delay ranges (a) $t = -1$ to 25 ps and (b) $t = -1$ ps to 1.2 ns, following photoexcitation at 340 nm. Growth/decay features i – iv highlighted, indicate the spectral location assigned to the ³ MLCT ESA, GSB of 1 , absorption of the PCI and, finally, photoproduct 2 , respectively.....	97
Figure 4.4 UV/Vis TAS of 890 μM solution of 1 in acetone over pump-probe delay ranges $t = -1$ ps to 1.2 ns, following photoexcitation at 340 nm. The ground state bleach of 1 is spectrally red-shifted in acetone relative to H_2O	100
Figure 4.5 Representative fits (grey) to transient absorption spectra (black dashed) at (a) $t = 1$ ps and (b) $t = 1$ ns, showing the individual basis functions used in the ‘target analysis’ of the TAS in Figure 4.3. Basis functions have been assigned to the ³ MLCT ESA (blue), PCI complex (green), GSB recovery of 1 (orange) and formation of the photoproduct 2 (cyan). Static UV/Vis absorption spectra in Figure 4.1 are used as basis functions for 1 and 2	102
Figure 4.6 Kinetic scheme illustrating the major pathways and associated time constants (τ), used to model the photodissociation dynamics of 1 in H_2O . The individual steps involved in this kinetic scheme are discussed further in the main text (Section 4.3.4).....	103

- Figure 4.7** | (a – d) Kinetic traces for the time-dependent evolution of the $^3\text{MLCT}$ state population (blue), PCI (green), photoproduct **2** (cyan) and GSB recovery of **1** (orange), obtained by integration of the basis functions (see Figure 4.5) used in the ‘target analysis’ of the TAS in Figure 4.3. Kinetic fits to these traces, in accordance with the scheme in Figure 4.6, are shown by the solid lines – see main text for details. (e) Kinetic trace reflecting the vibrational cooling of the $^3\text{MLCT}$ state at $t < 40$ ps (grey squares), obtained by integration of the ‘red edge’ of the $^3\text{MLCT}$ feature i in Figure 4.3a over a range $\lambda = 375 - 380$ nm. The solid grey line represents a fit to the trace with a bi-exponential decay function..... 106
- Figure 4.8** | Pictorial schematic of the post-dissociation processes involving the PCI and formation of the photoproduct **2**..... 108
- Figure 4.9** | Schematic potential energy profiles of the $^1\text{MLCT}$, $^3\text{MLCT}$, ^3MC , ^1MC and singlet ground state (GS) along the Ru–NA bond dissociation coordinate in **1**, including the major relaxation channels after excitation (hv) to the ‘bright’ $^1\text{MLCT}$ state. 114
- Figure 4.10** | (a) MECP of the CASSCF calculated $^3\text{MC}/^1\text{MC}$ ISC seam. Equatorial and axial angles of this geometry as well as the gradient difference motion (**g**) are presented. (b) MECP of the CASSCF calculated $^1\text{MC}/\text{GS}$ CI, of quasi-JT type, and branching space. Equatorial and axial angles of this geometry as well as the gradient difference (**g**) and derivative coupling motions (**h**) are presented. 116
- Figure 4.11** | Schematic potential energy surfaces for the significant electronic states in the PCI complex. From the top left, downwards: excited state population from the ^3MC of **1** (black) may land on the ^3MC PCI (purple) following NA ligand elimination; displacement through the $^3\text{MC}/^1\text{MC}$ ISC seam minimum (Figure 4.9a) to the ^1MC PCI (red); and then through the $^1\text{MC}/\text{GS}$ CI minimum (Figure 4.9b) leading to the GS of the PCI (green). On the GS, two possible isomers of PCI exist, labelled pro-cis and pro-trans, into which a solvent molecule may be accommodated to complete the formation of **2**..... 118
- Figure C.1** | Calculated (major) orbital transitions associated with (a, b) the $^1\text{MLCT}/^3\text{MLCT}$ states and (c) $^1\text{MC}/^3\text{MC}$ states for complex **1** using the TD-B3LYP method – see Table C.1h
- Figure C.2** | Calculated molecular orbital involved in the (major) orbital transitions associated with the $^1\text{MLCT}/^3\text{MLCT}$ states of the cis-[Ru(bpy)₂(NA)(H₂O)]²⁺ (**2**) photoproduct - see Table C.1 for details. Calculations were performed at the TD-B3LYP/cc-pVTZ-SDD level of theory.....h

List of Tables

Table 2.1 Details of the harmonic stage used to generate pump wavelengths of 800, 400 and 267 nm.	50
Table 2.2 Lenses used in the setup.....	51
Table 2.3 Reflective optics used in the setup	51
Table 2.4 Miscellaneous optics used in the setup	52
Table 3.1 Collated parameters from fitting of solvent-alone and guaiacol solution data.....	77
Table 4.1 Time constants (τ) and quantum yields (ϕ) extracted for the dissociation of 1 . Values for τ are extracted from kinetic fits to the traces in Figure 4.7, in accordance with the kinetic model presented in Figure 4.6. See main text for further details.	112
Table C.1 Calculated vertical excitation energies (ΔE), transition wavelengths and associated oscillator strengths (f) for significant triplet and singlet electronic excitation transitions in complexes 1 and 2 , using TD-B3LYP with an SDD 28 electron ECP (Ru) and cc-pVTZ (H, C, O and N) basis set. Major molecular orbital transitions and their relative contributions (%) to a given state are also provided (L = LUMO and H = HOMO) together with vertical energy differences (δE) between significant states in 1 (see Figure C.1 for orbital transitions in 1). Central wavelengths for the experimentally observed absorption bands of 1 and 2 , assigned predominantly to the ‘bright’ $^1\text{MLCT}$ state(s), are also given (<i>cf.</i> Figure 4.1).	i

Acknowledgements

It is difficult for me to overstate my gratitude to my Ph.D. supervisor, Dr Vasilios Stavros. Without his guidance, enthusiasm and belief I would have been lost. Thank you for making working with you so enjoyable and putting so much into my project.

I am fortunate to have spent my time at Warwick amongst such wonderful people: ‘Team Stavros’. I’d particularly like to thank Dr Gareth Roberts, for investing far more in myself and my work than he needed to. Thanks to the vacuous members (gas-phase spectroscopists, not dullards! Then again...): Mr Craig Williams, Dr Adam Chatterley, Dr David Hadden, Mr Jamie Young and Dr Michael Staniforth. It’s been a pleasure. Then in the solution corner, I thank Mr Michael ‘Mitch’ Horbury, who joined me in my final year and helped immensely to get these results; and the Masters students Mr William Powell, Ms Lucia Giffard and Mr Connor Gallagher with whom it was a pleasure to work.

I would also like to thank Costantini group members Dr Tom White, Dr Ada Della Pia, Mr Jonathan Blohm and Mr Ben Moreton for filling the office with so much enjoyable conversation. Thank you, Ada, for showing me the true comic potential of the Italian demeanour and debating so fervently the contents of spaghetti alla carbonara – I will still cook it how I like it!

This work would not have been possible without the help and support of many collaborators, particularly Ms Nichola Smith and Prof. Peter Sadler from Warwick, and Prof. Martin Paterson and Dr Dave Townsend from Heriot-Watt University. I’m also grateful to the mechanical and electronics wizards, particularly Mr Rod Wesson and Dr Alex Colburn, for fixing and building so many components of the setup.

To my friends and family, who I have abused so much in the wake of these studies, particularly my parents, Lila, and her parents, who have been so loving and supportive, I am so very grateful.

Finally I’d like to thank: Single Malt Scotch Whiskey; Jaffa Cakes; housemates Jamie, Dave, and Bells; that rock in Wales that nearly killed me; my bicycles; Khet; Four Tet; Archer; Barcelona, Valencia, Chamonix and Tenerife; and Vas (By The Power Of Greyskull), thanks for all the fish (tikka).

Declaration

This thesis is submitted to the University of Warwick in support of my application for the degree of Doctor of Philosophy. It has been composed by myself and has not been submitted in any previous application for any degree. The work presented (including data generated and data analysis) was carried out by the author except in the cases outlined below:

- α. Time-resolved photoelectron imaging measurements discussed in Section 3.4 were performed by J. O. F. Thompson and D. Townsend at Heriot-Watt University
- β. Theory calculations discussed in Section 3.5 were performed by T. N. V. Karsili and B. Marchetti at the University of Bristol
- γ. Synthesis and characterisation of complex **1** in Sections 4.2 and 4.3.1 were performed by N. A. Smith and P. J. Sadler at the University of Warwick
- δ. Data analysis discussed in Sections 4.3.3 was performed in collaboration with G. M. Roberts at the University of Warwick
- ε. Theory calculations discussed in Sections 4.3.1, 4.3.4 and 4.3.7 were performed by G. M. Roberts at the University of Warwick and R. G. McKinlay, J. M. Žurek, and J. M. Paterson at Heriot-Watt University

Parts of this thesis have been published by the author:

Chapter 3:

Greenough, S. E.; Horbury, M. D.; Thompson, J. O. F.; Roberts, G. M.; Karsili, T. N. V.; Marchetti, B.; Townsend, D.; Stavros, V. G.; “Solvent Induced Conformer Specific Photochemistry of Guaiacol”; *Phys. Chem. Chem. Phys.*, **16**, **2014**, 16187.

Chapter 4:

Greenough, S. E.; Roberts, G. M.; Smith, N. A.; Horbury, M. D.; McKinlay, R. G.; Žurek, J. M.; Paterson, M. J.; Sadler, P. J.; Stavros, V. G.; “Ultrafast Photo-Induced Ligand Solvolysis of *cis*-[Ru(bipyridine)₂(nicotinamide)₂]²⁺: Experimental and Theoretical Insight into its Photoactivation Mechanism”; *Phys. Chem. Chem. Phys.*, **16**, **2014**, 19141

Abstract

Two areas of study are presented in this thesis: photostability of biomolecules and photoactivation of transition metal complexes. The implementation of a newly constructed transient absorption spectrometer, to investigate relevant photodissociation reactions in solution, is documented and includes a description of a gravity driven thin-film liquid jet, which may prove useful to spectroscopists seeking to remove sample/glass interaction or maximise their temporal resolution.

Toward the subject of photostability of biomolecules, solvent induced conformer-specific photodissociation dynamics of guaiacol are elucidated. A particular photodissociation channel is observed to effectively be switched on or off depending on the solvent (cyclohexane or methanol) used. This is attributed to the interchangeable solvent specific conformers of guaiacol; an intramolecular H-bond between OH and OMe moieties is formed in cyclohexane whereas an intermolecular H-bond between OH and solvent is formed in methanol. The latter is thought to lower a barrier to O–H dissociation and facilitates H-atom loss via tunnelling.

The photoactivation mechanism of *cis*-[Ru(bipyridine)₂(nicotinamide)₂]²⁺, a photoactive species designed to display high cytotoxicity following irradiation, for potential use in photodynamic therapy (photochemotherapy), is investigated. The photoactivation process is shown to occur with a high quantum yield and on an ultrafast timescale. Importantly, the conclusions here provide a detailed understanding of the initial stages involved in this photoactivation and the foundation required for designing more efficacious photochemotherapy drugs of this type.

*“I thought of that while
riding my bicycle”*
– Albert Einstein



1.1. Overview

Optical spectroscopy has long been renowned for its power in providing electronic and vibrational properties of a vast number of systems from simple diatomics, to very complex polyatomic molecules. Recording absorption or emission spectra, generated when electromagnetic radiation interacts with matter, provides information on molecular structure and the molecules' interaction with their environment.

Of the many types of spectroscopy, most are simply measurements of a change in intensity of a particular wavelength of light as a result of its interaction with the sample. The spectral resolution of such wavelength measurements or *linewidth* was drastically improved by the use of the laser, invented in the late 1960s, which had the ability to produce photons over a very narrow range of wavelengths (or narrow spectral bandwidth). Indeed the use of early dye lasers to create highly frequency selective, coherent and high-powered beams of light brought about a torrent of new techniques and technology.

The development of *ultrafast* pulsed lasers allowed the monitoring of molecular dynamics on a femtosecond (fs ($1\text{ fs} = 1 \times 10^{-15}\text{ s}$)) timescale. This level of time resolution is important as changes in nuclear geometry as a result of excitation, *i.e.* photochemistry, occur on this timescale. Early work that began to utilise ultrafast lasers in the late 1980s, chiefly by Ahmed Zewail,¹ studied the transition states of chemical reactions. A representative example involved monitoring the photodissociation of the I-CN bond in real-time using the pump-probe technique – one *pump* pulse to prepare the molecule in the excited state and a second *probe* pulse, delayed in time, to determine the excited state dynamics, *i.e.* the progress of the reaction. This femtosecond time-resolved spectroscopy brought about an area of study now known as 'femtochemistry' for which Zewail was awarded the 1999 Nobel Prize in Chemistry.

The work in this thesis is aimed toward a better understanding of how excited state relaxation pathways operate in *photostable* and *photoactive* molecules. This chapter introduces these

relaxation pathways (discussed in Sections 1.2 and 1.3), the femtochemistry techniques to study them (Section 1.4) and related work upon which we build (Sections 1.5 and 1.6). The second chapter documents the construction and optimisation of a transient absorption spectrometer for the study of solution-phase dynamics.

An important theme of the thesis is the utilization of knowledge garnered through gas-phase experiments to understand solution-phase dynamics; combining complementary methods to yield a more complete picture. In Chapter 3 we use this approach to aid in the understanding of *photostability* (avoiding chemical reaction) pathways in biological molecules, here studying guaiacol (2-methoxyphenol).

Knowledge of photostability mechanisms is equally applicable toward *photoactivation* (inducing chemical reaction) as they share much the same photophysics and may only become differentiable at a single point. In Chapter 4 we examine the photoactivation of a novel ruthenium polypyridyl complex designed to exhibit cytotoxicity following excitation.

1.2. The Fates of Excited States

The various photophysical processes that accompany the electronic excitation of a molecule may be explained using state diagrams of the type shown in Figure 1.1. All these processes may be described as either *radiative* or *non-radiative* transitions between energy levels, where the absorption or emission of a photon is elicited in the former but not the latter. In either case the molecular geometry strictly remains the same, but typically the movement of electrons between different molecular orbitals consequently causes structural changes, such as bond angle and bond length deviation. These effects, which cause *photochemistry*, are discussed in Section 1.2.4. This section outlines the basic concepts seen in Figure 1.1.

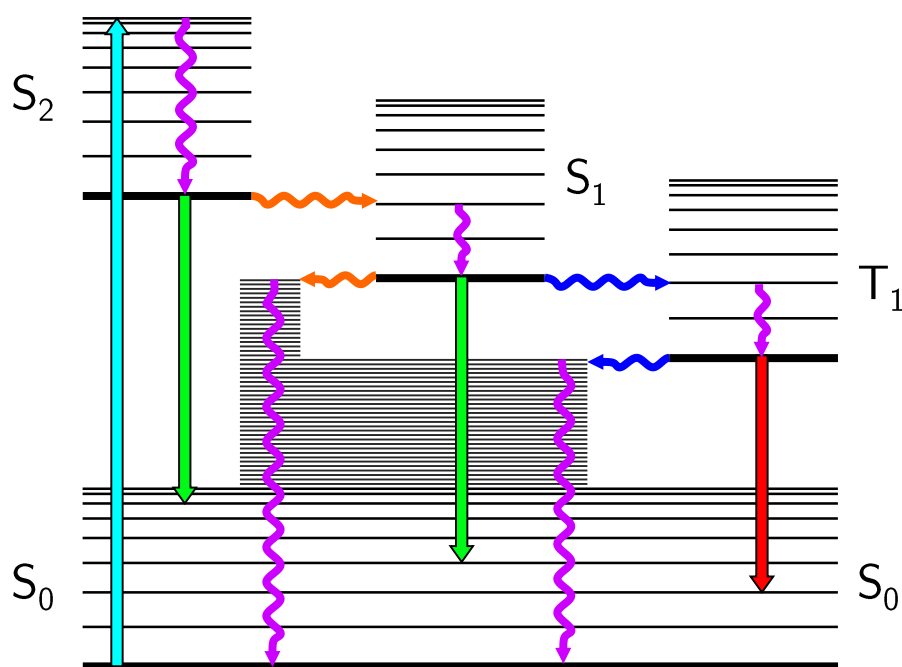


Figure 1.1 | Jablonski diagram depicting molecular states and photophysical processes connecting them. The vertical positions of thick lines correspond to the electronic energy minima of electronic ground and excited states. Thin black lines correspond to vibrational levels. As is the convention, straight arrows refer to radiative transitions (cyan: absorption, green: fluorescence, red: phosphorescence), while curvy arrows depict non-radiative processes (orange: internal conversion, blue: intersystem crossing and violet: intramolecular vibrational relaxation). The width and position of lines on the abscissa have no physical connotation and are placed for aesthetics.

1.2.1. Radiative Processes

1.2.1.1. Absorption

A molecule may assimilate a photon of energy to be promoted from a low-lying state to a higher one (cyan arrow Figure 1.1). The absorption of electromagnetic radiation in the UV/Vis region of the spectrum typically corresponds to the displacement of electrons between molecular orbitals and are thus termed electronic transitions. The degree of light absorbed by matter may be determined through the difference of the intensity from the light source before and after having passed through the substance. The Beer-Lambert law summarises this relation:

$$A(\nu) = -\log_{10} \left(\frac{I'}{I} \right) = \epsilon(\nu)lc \quad (1.1)$$

where $A(\nu)$ is absorbance (or optical density, OD) of a specific energy, I is the intensity of incident radiation, I' is the intensity of light transmitted (such that transmittance, $T = I'/I$), $\epsilon(\nu)$ is the molar absorption coefficient, l is the path length and c is the concentration of molecular absorbers. The molar absorption coefficient is usually taken in units of $\text{M}^{-1} \text{cm}^{-1}$. Absorption becomes fundamental to this thesis, as it is both the initiation for the photochemistry and the main probe (see Section 1.4) for all processes met in this research.

1.2.1.2. Transition Dipole Moment and Oscillator Strength

Electronic excitation is driven by the interaction of the electric field component of light with electric dipoles, formed from a difference in point charges, within molecules. A dipole moment μ is a vector pointing from a negative charge q^- to positive charge q^+ displaced by distance r . The magnitude of μ is thus given as $\mu = qr$ and is typically stated in Debye, $1 \text{ D} = 3.336 \times 10^{-30} \text{ C}\cdot\text{m}$. In the electric field of light, the two charges experience a force in opposite direction that is proportional to both the magnitude of the charges and their separation and may vary with the angle between the dipole moment and the electric field vectors.

For a molecule (a multi dipole system), the *molecular* dipole moment operator, $\hat{\mu} = \sum_i q_i \mathbf{r}_i$, may be used in the quantum mechanical expression of the transition between states i and f :

$$\mathbf{M}_{if} = \int \Psi' \hat{\mu} \Psi'' d\tau \quad (1.2)$$

where Ψ'' and Ψ' are the wavefunctions of the states i and f , respectively. \mathbf{M}_{if} is known as the transition dipole moment (TDM) and may be described as the measure of the dipole moment associated with the movement of electrons that occurs during electronic excitation. The probability that such a transition may take place is then found as the square of \mathbf{M}_{if} and often given as an oscillator strength f :²

$$f_{if} = \frac{8\pi^2 m_e \nu}{3\hbar e^2} \times |\mathbf{M}_{if}|^2 \quad (1.3)$$

where m_e is electron rest mass, e is elementary charge, h is Planck's constant, and ν frequency of incident light.³

Following excitation, the nuclei of a molecule are subjected to new forces and often elicit vibrational motion. Vibrational and rotational energy levels within electronic states and linewidth broadening (see Section 1.3.3.1) lead to broader energy transitions that yield absorption *bands*. Experimentally the oscillator strength may be determined by integration of an absorption band, and thus relates back to the molar absorption coefficient $\varepsilon(\nu)$ as:

$$f_{if} = 4.3 \times 10^{-5} \int \frac{\varepsilon(\tilde{\nu})}{\text{M}^{-1}\text{cm}^{-1}} \frac{d\tilde{\nu}}{\text{cm}^{-1}} \quad (1.4)$$

For a very strong absorption, $\varepsilon(\tilde{\nu}) \approx 10^5 \text{ M}^{-1}\text{cm}^{-1}$ with a typical bandwidth of 3000 cm^{-1} , the oscillator strength is of the order of 1.³

1.2.1.3. Emission

In addition to excitation, there are a number of radiative processes where the emission of a photon occurs. These may be considered as *spontaneous* or *stimulated* emission. The spontaneous emission of excited molecules or *luminescence*, is termed *fluorescence* (green arrow Figure 1.1) when the emissive state is a singlet and *phosphorescence* (red Figure 1.1) when emission is from a triplet state (see Section 1.2.3). Spontaneous emission is a crucial relaxation pathway in various species; detecting fluorescence and phosphorescence is an extremely powerful experimental approach.⁴ Stimulated emission, which may be seen as an equivalent to (stimulated) absorption, occurs when an electromagnetic field interacting with molecule causes the release a photon that is of equal energy to the incident one. It is through stimulated emission that laser action is induced and luminescent states are detected in the experiments here (see Section 1.4.1).

1.2.2. Non-Radiative Vibrational Energy Transfer

Excess vibrational energy imparted through excitation above the zero point energy (ZPE, the lowest vibrational level within an electronic state) may be transferred to other vibrational levels

of equal or less energy through various non-radiative vibrational energy transfer (VET) processes. Energy can dissipate through thermal motion to the surroundings and is thus termed *intermolecular energy transfer* (IET). For all but diatomics, molecules may also distribute vibrational energy throughout other vibrational modes, termed *intramolecular vibrational-energy redistribution* (IVR).^{5,6}

1.2.2.1. Intramolecular Vibrational-Energy Redistribution

The role of IVR is particularly apparent in gas-phase experiments where IET is checked by the absence of interaction with surrounding molecules, as is the case in solution. IVR is elicited through anharmonic coupling between various vibrational modes (density of states).⁷ For very small molecules, where there are few enough modes that IVR is a reversible process, periodicity may be observed due to partial recurrences of the initially populated states.⁶ Larger systems (>10 atoms), which are of concern in this thesis, have a much higher density of acceptor states (so may be treated as a continuum of states) that cause net flow out of the initially populated states irreversibly. The probability, and thus rate, k_{ij} , of the transition between the initial state i and a continuum of states j , is proportional to the strength of the coupling between states, V_{ij} , and the density of acceptor states, ρ_j . This relationship is known as *Fermi's golden rule*:⁸

$$k_{ij} = \frac{2\pi}{\hbar} |V_{ij}|^2 \rho_j \quad (1.5)$$

Because this transition rate is proportional to the density of states, rates of IVR vary greatly depending on the molecule's size. Large molecules typically elicit picosecond IVR lifetimes ($\tau = 1/k$). IVR rates can also depend on the level of excitation because of the change in energy spacings as the molecule cascades through vibrational energy levels. In some cases, *e.g.* benzene,⁹ ethane,¹⁰ bromomethane,¹¹ fast relaxation at high vibrational energy is followed by stagnation (or a bottleneck) due to the reduced density of states and larger energy spacing at smaller vibrational frequencies.⁵

IVR may be enhanced through solute-solvent interactions. Particularly, the coupling of energy from one solute mode to another, through a resonant solvent mode or changing the potential energy surfaces (see Section 1.3.1) of the solute, can lead to an increased coupling strength.⁵

1.2.2.2. Intermolecular Energy Transfer

Whilst IVR refers specifically to a redistribution of energy, such that the overall potential energy of the excited molecule remains the same[†], IET is responsible for the removal of potential energy from, or the *relaxation* of, a solute molecule as heat to the solvent. Rates of IET (when separable from IVR) are typically slower, *e.g.* benzene $\tau_{\text{IVR}} \approx 2$ ps, $\tau_{\text{IET}} \approx 70$ ps.¹² In some cases, IET can prevent stagnation of IVR by supplying or accepting energy differences between solute modes that are acting as bottlenecks.⁵

The probability of IET can be described using a Landau-Teller approach[‡] where the rate of IET is proportional to the frequency-dependant friction $\xi(\omega)$ at oscillator frequency ω , which describes the solvent forces acting on the ‘donating’ vibrational coordinate of the solute. The rate of IET as described by Hochstrasser and co-workers,⁵ is given by:

$$k_{\text{VET}} = \frac{2 \tanh(\hbar\omega/2 k_B T)}{\mu \hbar \omega / k_B T} \xi(\omega) \quad (1.6)$$

Typically $\xi(\omega)$ is larger at low frequencies and decays exponentially with increasing ω causing IET to be dominated by the lowest frequency solute modes. It can also be seen from Equation 1.6 that IET is temperature dependant and has less dependence, compared to IVR, on the solute density of states.

The timescales for VET are typically of the order of one to tens of picoseconds for large systems in solution.¹² Because this is considerably faster than observed spontaneous emission

[†] The IVR arrows in Figure 1.1 are representative for a single coordinate, having moved energy to other acceptor modes to compensate.

[‡] A semi-classical molecular collision theory treating the interaction of two particles, A and B. For its application here, A is a solvent molecule in collinear collision with a harmonic oscillator BC (vibrational mode of solute molecule) under a repulsion between A and B.¹³

timescales, fluorescence and phosphorescence are usually only observed from lower vibrational energy levels of a given electronic state, regardless of the excitation energy.⁴ The resulting difference between excitation and emission frequencies is known as the Stokes shift.⁴

1.2.3. Internal Conversion and Intersystem Crossing

Non-radiative conversion between electronic states may occur such that electronic energy is distributed over many vibrational modes. During such a transition, if the spin is preserved then this known as internal conversion (IC) (orange Figure 1.1). IC is driven by the coupling of vibronic states; vibrational modes in the initially excited electronic state couple with degenerate (higher vibrational) modes in the lower lying electronic state.¹⁴

Quantification of the rate of IC (k_{IC}) can be treated similarly to IVR; k_{IC} is proportional to the density of vibrational states in the initial and final electronic states.¹⁴ The strength of the coupling between two vibronic states is dependant of the energy gap, ΔE , between the electronic states such that k_{IC} also has the following proportionality:¹⁵

$$k_{IC} \propto \exp\left(-\Delta E/h\nu\right) \quad (1.7)$$

where ν is the vibrational frequency. Internal conversion is therefore most likely to occur where electronic states lie closest in energy (such conditions are discussed in Section 1.3.4). As with VET, IC typically occurs on a faster timescale than fluorescence (observing a Fermi's golden rule model) and kinetically out competes it. Because the gap between the ground state (S_0) and first excited state (S_1) of most molecules is relatively large compared to the gap between higher energy levels ($S_n \leftarrow S_{n+1}$ (where $n > 1$)), $S_0 \leftarrow S_1$ fluorescence may become the favoured relaxation pathway for the S_1 state in the absence of an efficient IC channel. This is the cause the observed norm: *Kasha's rule*, where luminescence is usually only detected from the lowest excited electronic state.

Non-radiative conversion between electronic states of different spin multiplicity is a “forbidden process” termed intersystem crossing (ISC, blue arrow Figure 1.1). Where there is sufficient

spin-orbit coupling, such as in molecules containing heavy atoms, ISC can become a highly favoured process.⁸ This allows the conversion between singlet (S) and triplet (T) states. A common outcome following ISC is the trapping of population in the triplet multiplicity as VET and IC traffic population to the lowest vibrationally and electronically excited triplet state (T_1). Due to the forbidden nature of the process, radiative decay from T_1 to the singlet ground (S_0) state, or phosphorescence (red arrow Figure 1.1), may then occur on a very long timescale (milliseconds to hours).⁸

1.2.4. Photodissociation

Finally a further molecular relaxation process not indicated in Figure 1.1 is that of dissociation. If electronic transitions lead to the system accessing a state that has repulsive character with respect to a nuclear coordinate (see Section 1.3 for characterisation of excited state ‘shape’) then fragmentation along said coordinate may occur, *i.e.* a bond AB can break into fragments A and B. Excess electronic energy is transferred to internal energy in either fragment or translational energy, *i.e.* fragments are repelled ballistically. Following photodissociation, fragments, or products produced from their reaction, are convenient handles for probing the photochemistry at play. The results discussed in this thesis are based around photoexcitation leading to dissociation.

1.3. Femtochemistry

1.3.1. Born-Oppenheimer Approximation

Thus far we have treated electronic states as energy levels with no apparent change in molecular structure. Such a simplification is made when describing a system quantum mechanically. The Born-Oppenheimer approximation states that since electrons are orders of magnitude lighter than nuclei ($m_{proton}/m_{electron} \approx 1,836$), on the time scale of electron motion, nuclei may be regarded as stationary. This allows for an estimate for the molecular wavefunction of a system

to be made by separating the nuclear and electronic terms in the Schrödinger equation.^{8,16,17} The Schrödinger equation for a molecular wavefunction $\Psi(r, R)$ is given by:

$$\mathcal{H}\Psi(r, R) = E\Psi(r, R) \quad (1.8)$$

where E is the total energy and R and r are nuclear and electron displacement, respectively. \mathcal{H} is the molecular Hamiltonian and is the sum of the kinetic and potential energy operators:

$$\mathcal{H} = [T_n(R) + T_e(r) + V_{ne}(R, r) + V_{nn}(R) + V_{ee}(r)] \quad (1.9)$$

where T_n and T_e are nuclear and electronic kinetic operators, respectively, and V_{ne} , V_{nn} and V_{ee} are the potential energy operators of Columbic interactions between particles. Separating the molecular wavefunction of Equation 1.8, in line with the Born-Oppenheimer approximation, yields the nuclear $\Psi_n(R)$ and electronic $\Psi_e(R, r)$ wavefunctions:

$$\Psi(r, R) = \Psi_e(R, r)\Psi_n(R) \quad (1.10)$$

If the nuclear configuration R is fixed, an electronic Schrödinger equation:

$$[T_e(r) + V_{ne}(R, r) + V_{ee}(r)]\Psi_e(r, R) = E_e(R)\Psi_e(r, R) \quad (1.11)$$

and a nuclear Schrödinger equation:

$$[T_n(R) + V_{nn}(R) + E_e(R)]\Psi_n(R) = E(R)\Psi_n(R) \quad (1.12)$$

may be determined. Each has corresponding terms from Equation 1.9 that operate only on either the electronic or nuclear wavefunction. The energy of the electronic wavefunction $E_e(R)$ and the internuclear potential energy operator $V_{nn}(R)$ combine to give a molecular potential energy $P(R)$ that is solely dependent on nuclear geometry. The potential energy of an electronic state of an N atom non-linear molecule can therefore be described by an $3N - 6$ [§] dimensional surface. These potential energy surfaces (PES) are important to understand and visualise molecular dynamics. For any large system, calculating such a PES would not only be

[§] Normal modes of vibration. The 6 translational and rotational modes do not affect the potential energy.

challenging due to computational expense but often futile considering only some or one of the coordinates will be responsible for the observed dynamics. More often then, when considering the potential energy of a system, only the reactive coordinates are considered. This yields PES or cuts, of the type seen below and elsewhere in this thesis (Section 1.5.2 and Chapters 3 and 4).

1.3.2. Franck-Condon Principle

Figure 1.2 is a graphical depiction of a PES viewed along one particular degree of freedom, where nuclear separation R is marked on the abscissa and potential energy E on the ordinate, in which the arrows that depict radiative transitions here are purposely drawn vertically. This is a further application of the Born-Oppenheimer approximation; photoexcitation to, or photoemission from, an electronic state occurs between the same nuclear coordinates of a PES and are described as *vertical* transitions.¹⁸ It has already been stated in Equation 1.2 that the transition probability is dependent on the overlap between initial Ψ'' and final Ψ' wavefunctions. If the total wavefunction is separated into nuclear and electronic wavefunctions, as demonstrated in Equation 1.10, Equation 1.2 may be given as:

$$\mathbf{M}_{if} = \int \Psi'_e(R, r) \hat{\boldsymbol{\mu}} \Psi''_e(R, r) d\tau \int \Psi'_v(R) \Psi''_v(R) d\tau \quad (1.13)$$

The first term contains the spatial overlap integral of the electronic wavefunctions and their interaction with the electric molecular dipole moment operator $\hat{\boldsymbol{\mu}}$. The right-hand term contains the overlap integral of the vibrational wavefunctions (vibrations are the relevant nuclear modes of freedom) and is known as the Franck-Condon factor. The Franck-Condon principle, dictates that the probability of an electronic transition is greatest between vibrational levels with the largest overlap of vibrational wavefunctions. This is depicted in Figure 1.2, where the arrows depict transitions that have the greatest overlap of vibrational wavefunctions.

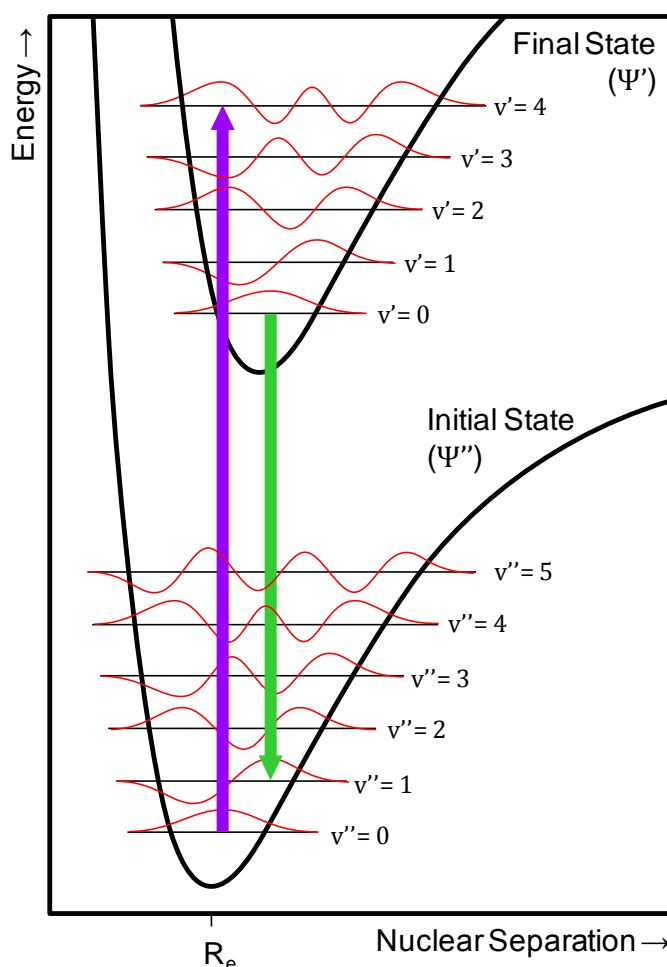


Figure 1.2 | PES along a single nuclear coordinate of initial and final electronic states. The Franck-Condon factor for the photoexcitation from $\Psi''_{v=0}$ is greatest for $\Psi'_{v=4}$. Photoemission from $\Psi'_{v=0}$ has the most favourable overlap with $\Psi''_{v=1}$.

Excited state PES generally differ to those of the ground (initial) state due to a change in geometry associated with displacement of electrons from bonding molecular orbitals. For the coordinate shown here, the equilibrium bond length R_e of the initial state is different to the optimal bond length of the excited state and hence the potential energy surfaces are offset in nuclear separation. It can be seen that an electronic transition starting in $\Psi''_{v=0}$ will encounter the most favourable overlap (of the vibrational wavefunctions shown here) with $\Psi'_{v=4}$ and hence the transition probability of $\Psi'_{v=4} \leftarrow \Psi''_{v=0}$ will be higher than other possible transitions from $\Psi''_{v=0}$. It can be seen that following VET processes, photoemission occurring from $\Psi'_{v=0}$ has a different preferred transition *i.e.* the Franck-Condon *window* has changed.

1.3.3. Wavepackets

The depiction of the Franck-Condon principle in Figure 1.2 only shows excitation for a single frequency. We will shortly see that femtosecond pulses are necessarily broadband and photoexcitation produces an excited state consisting of multiple vibrational states. This forms a coherent superposition of vibrational states known as a wavepacket, that evolves with time.⁸

1.3.3.1. Energy-Time Uncertainty and Bandwidth Limitation

The uncertainty principle means that two complementary observables cannot simultaneously be known precisely. It is possible to give up the precision of one variable in order to gain a greater specification of a complementary property. The most common example of this uncertainty is that of Heisenberg and the relation of the location and linear momentum of a particle.⁸ A similar complementarity exists between energy and time:

$$\Delta E \Delta t \geq \hbar/2 \quad (1.14)$$

where ΔE and Δt are the uncertainties of energy and time, respectively. It is due to this energy-time uncertainty that the ultrafast pulses required for femtosecond time resolution have broad energies. The laser pulses used in most pump-probe experiments have Gaussian profiles, which are measured at the full width at half maximum (FWHM) in temporal or frequency domains. The energy-time relationship in this case is given by:

$$\Delta \nu \approx \frac{0.441}{\tau_p} \quad (1.15)$$

where $\Delta \nu$ is the frequency FWHM and τ_p is the temporal FWHM or pulse duration. As an example, with regards to photoexcitation and wavepacket generation, a 50 fs bandwidth

limited** pulse has a bandwidth of $\sim 300 \text{ cm}^{-1}$. This is large enough to excite several vibrational levels in large molecules and cause the creation of a wavepacket on the excited state PES.

1.3.3.2. The Generation and Evolution of Wavepackets

The superposition of n vibrational wavefunctions gives a time-dependant wavefunction of a wavepacket $\Psi(t)$:

$$\Psi(t) = \sum_n A_n \psi_n e^{-iE_n t/\hbar} \quad (1.16)$$

where ψ_n is the n^{th} vibrational wavefunction, E_n is its energy and A_n is an expansion coefficient accounting for the excitation pulse's shape (Gaussian) and electric field, Franck-Condon factors and dipole moment operators of each vibronic transition. Upon initial excitation, the wavepacket is localized on a PES where the component wavefunctions constructively interfere; elsewhere they destructively interfere. Because the time-dependent factor affects the phases of the waves, the locus of constructive interference will change with time. This effectively causes the wavepacket to move across the PES as a coherent entity. The movement of a wavepacket in a harmonic well can therefore be described like a classical particle; it may be visualised as a marble swirling around in a bowl.

1.3.4. Electronic State Degeneracy

The energy-gap law, Equation 1.7, shows that non-radiative transitions have a higher probability if the energy difference of between states, ΔE , is small. The rearrangement of nuclear coordinates can affect the potential energy of states differently, depending on the character of the state *e.g.* excited states may have repulsive character for particular coordinates (see Section 1.2.4). At certain nuclear coordinates, the ΔE of two PES may tend toward zero *i.e.* they are degenerate. In such cases the two PES may form either an *avoided crossing* or a *conical intersection*. Avoided crossings occur between states of the same spin multiplicity and

** Gaussian pulses that have a time-bandwidth product of 0.441 are known as bandwidth limited *i.e.* they aren't temporally dispersed or *chirped*.

symmetry in one dimension of nuclear coordinate space. In addition to avoided crossings in polyatomic molecules, the extra dimensionality (degrees of freedom) can cause a change to the molecular symmetry and allow states to cross.

1.3.4.1. Conical Intersections

For a polyatomic molecule of N atoms, two PES are allowed to cross along a $3N - 8$ dimensional subspace of the $3N - 6$ nuclear coordinate space. Each point in nuclear coordinate space where the two electronic states are degenerate is known as a point of conical intersection. Figure 1.3 shows the energy of two convergent PES as functions of the remaining two nuclear coordinates X_1 and X_2 . These dimensions form the two-dimensional *branching space*. Movement in the branching space lifts the degeneracy in the subspace.

The local topography of the convergent PES resembles two cones connected at the apices, hence the term conical intersection. It is through these areas of electronic state degeneracy that IC and ISC occurs. Their character is therefore important to consider in molecular dynamics.

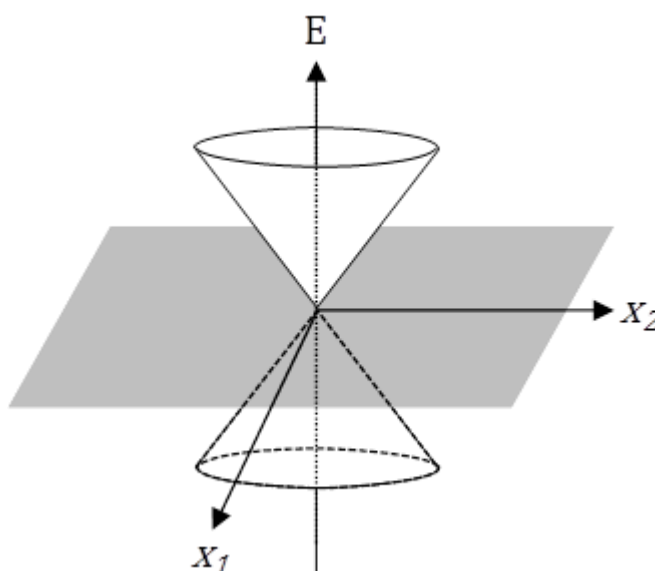


Figure 1.3 | Energy of two convergent PES in the X_1 , X_2 branching space (grey shading) form a conical intersection.

1.3.4.2. Tunnelling

Wavepacket motion across PES was earlier likened to that of a marble on a surface. Whilst usually useful when describing dissociative states for example, a classical description neglects the quantum tunnelling phenomenon. Figure 1.4 shows an example of a wavefunction's interaction with a barrier formed between two states (S'' and S'). In the classical sense, the barrier is insurmountable as there is not the required energy to do so. Quantum tunnelling allows a wavefunction, and therefore wavepacket, to travel through the barrier. Whilst its amplitude decays exponentially, it will not necessarily become zero. There is therefore a probability that a wavefunction or wavepacket may emerge from the barrier with non-zero amplitude.

For a single dimension, where u is a vibrational mode like that seen in Figure 1.4, the lifetime of tunnelling τ can be approximated using a semiclassical Wentzel-Kramers-Brillouin (WKB) approach¹⁹:

$$\tau = \left[v_u \exp \left(-2 \int_{u_1}^{u_2} \sqrt{\frac{2m}{\hbar^2} (V(u) - E)} du \right) \right]^{-1} \quad (1.17)$$

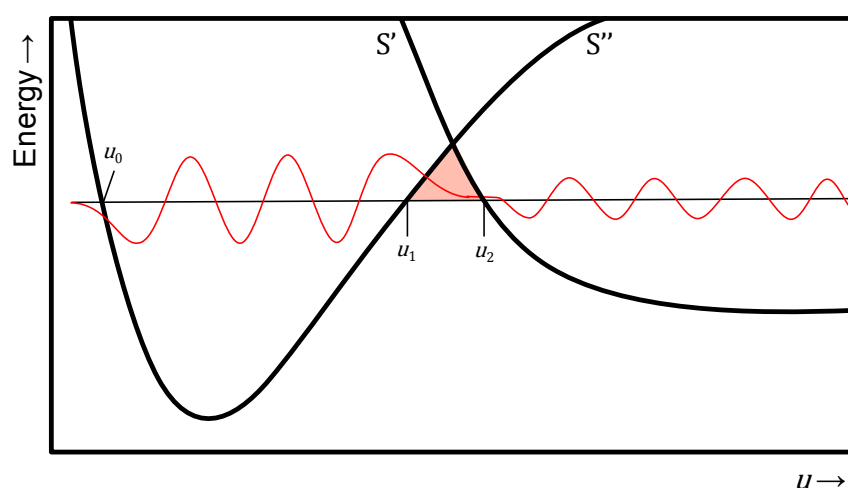


Figure 1.4 | Quantum tunnelling of a wavefunction through a potential barrier along some nuclear separation u . In the bound region, u_0 - u_1 , a normal harmonic wavefunction is observed. The classically forbidden region, *i.e.* the barrier u_1 - u_2 carries an exponential decay of the wavefunction that emerges on the second state, $>u_2$.

where ν_u is the frequency of the vibrational mode, m is the mass of the tunnelling particle, $V(u)$ is the potential barrier, and E is the energy of the wavefunction. The rate of tunnelling has an exponential proportionality with the mass of the tunnelling particle and the barrier size. Short tunnelling lifetimes are therefore only observed for light particles, *e.g.* hydrogen, tunnelling through small barriers. Whilst the WKB approximation has been shown to have good accuracy in predicting tunnelling rates in model systems, *e.g.* phenol: see section 1.5.2, it only accounts for a single reaction coordinate and contributions from other degrees of freedom are neglected.

1.4. Pump-Probe Spectroscopy

As already mentioned, pump-probe spectroscopy relies on the use of a preparatory *pump* pulse to prepare the sample in the excited state, and a *probe* pulse, delayed in time (the pump-probe delay, t) to measure the system spectroscopically. Probing at varying pump-probe delays allows the dynamics in question to be followed. The type of probe used is what sets techniques apart. This thesis primarily only discusses results of ultrafast transient absorption (TA) spectroscopy but the complementary gas-phase technique of time-resolved photoelectron imaging spectroscopy (TRPEI) is also used.

1.4.1. Ultrafast Transient Absorption Spectroscopy

Ultrafast TA spectroscopy (Figure 1.5) has been used to study excited state dynamics in a plethora of materials such as transition metal complexes,²⁰⁻²³ photosynthetic carotenoids,^{24,25} and DNA base analogues^{26,27} and structures,^{28,29} photovoltaic materials³⁰⁻³² and myriad organic molecules.³³⁻³⁶ Since the method does not rely on fluorescence, it can be used to examine

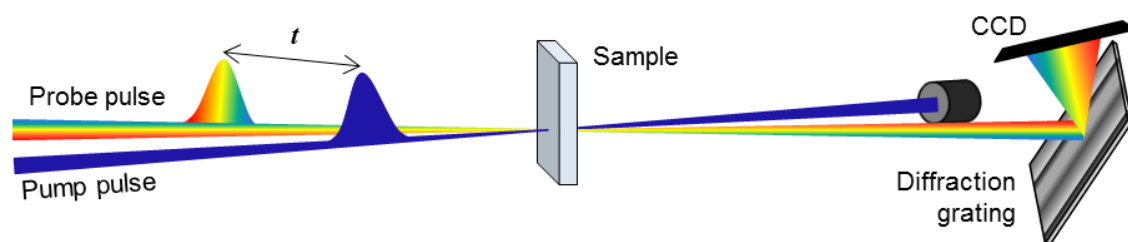


Figure 1.5 | Schematic showing how the two laser pulses are sent through the sample at pump-probe delay time t and the probe pulse is detected by the photodiode array.

optically dark states (populated by relaxation from an excited state) and non-emissive states. For example, a recent publication in *Nature*,³⁷ which employed ultrafast TA for its experimental data, revealed the complete dynamics of the initiation of vision. Before this was published, the conversion of the 11-*cis* retinal chromophore to its all-*trans* form in rhodopsin had been identified as the primary photochemical event in vision, and the details of this process had drawn much experimental and theoretical interest. This latest study used an extremely high experimental time resolution (<20 fs) to monitor wave-packet dynamics as a function of the isomerization coordinate, *i.e.* the *cis-trans* twist. They observed stimulated emission from the excited singlet state as it rearranged its configuration and photoinduced absorption from the hot ground electronic state of the *trans*-photoproduct within 200 fs.

In TA spectroscopy, the pump pulse promotes a fraction of the molecules in the sample to an electronically excited state. At a delay t after this, a weak probe pulse (*i.e.* a pulse that is of such a low intensity so as not to appreciably alter the sample further) is sent through the sample and

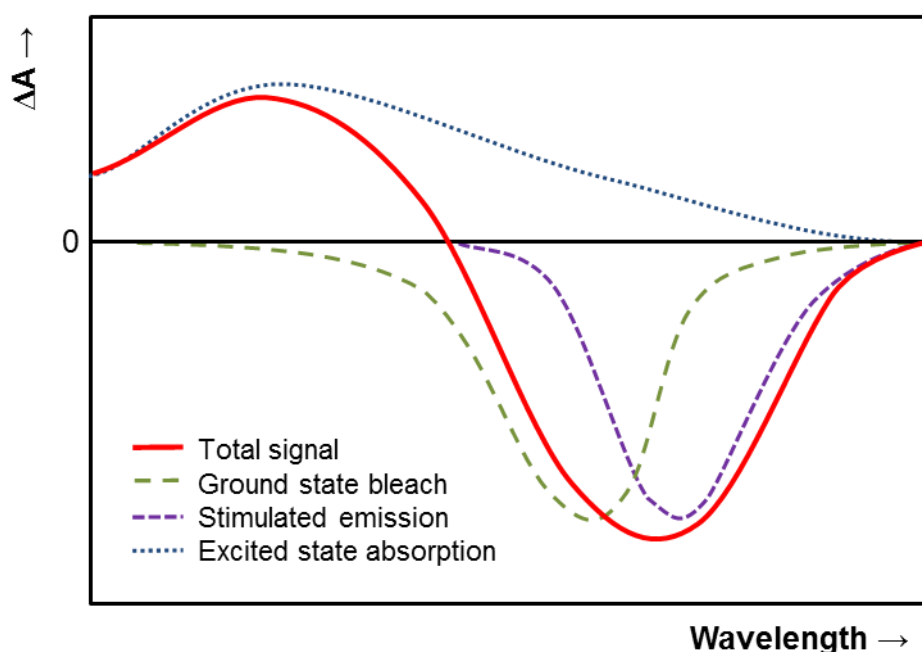


Figure 1.6 | A typical TAS with the various contributions: 1. Ground-state bleach (ochre dashed line). 2. Stimulated emission (purple dashed line). 3. Excited-state absorption (blue dotted line). The sum of these contributions is shown in the solid red line.

the absorption spectrum recorded (Figure 1.6). The use of a mechanical chopper in the pump beam running at half the repetition rate of the laser allows only every other pulse to be incident on the sample so that the probe beam sees the sample in a pumped, non-pumped alternating fashion. From this, a difference absorbance (ΔA or differential optical density, ΔOD) spectrum or *transient absorption spectrum* (TAS), *i.e.*, the absorbance of the excited sample minus the absorbance of the sample in the ground state (GS), can be obtained for each pump-probe time delay. By recording the TAS for a range of time delays, a ΔA profile as a function of pump-probe time delay t and wavelength λ , which provides information about the system dynamics, can thus be created.

The TAS is made up of contributions from various processes:²⁴

1. Ground state bleach (Figure 1.6 ochre dashed line) – Since a fraction of the molecules are excited to a higher state, the population of the GS has been reduced. The GS absorption in the excited sample is less than that of the non-excited sample, so a negative signal in the TAS is observed for the region of wavelengths absorbed by the GS.
2. Stimulated emission (Figure 1.6 purple dashed line) – Upon population of the excited state, the probe pulse can cause stimulated emission as it passes through the sample. A photon of the probe pulse induces the stimulated emission of an excited molecule, emitting a photon in the identical direction, hence more light is detected and a negative ΔA signal arises. This can only occur for optically allowed transitions and is Stokes shifted with respect to the ground state bleach. It is important to use weak probe pulses to avoid this affecting the result appreciably.
3. Excited state absorption (ESA, Figure 1.6 blue dotted line) – The excited molecules themselves may absorb light and be promoted to even higher states (if there are optical transitions that allow it) by the pump pulse. Consequently a positive ΔA signal is

observed in the wavelength region of the ESA. Again, the effect of this is reduced when using a low intensity probe pulse.

4. Product absorption – Excitation with the pump pulse may cause reactions to occur where transient molecular states such as a triplet state, charge-separated states and isomerized states may form – the absorption of which gives a positive ΔA signal. This is not shown in Figure 1.6, but could look like the exemplar ESA shown.

A few other important considerations need to be taken into account:

- Firstly the *beam geometry* – the angle at which the pump and probe beams are incident in the sample and size (diameter) of the probe beam in relation to that of the pump. The time resolution of the spectrometer is determined by the temporal width of the pump-probe cross-correlation function. There is an angular dependence of this, which is greatly affected by the relative size of the two beams. For angles greater than 5° there is significant broadening of the temporal response; an effect magnified by also increasing the probe beam diameter (if $d_{\text{probe}} < d_{\text{pump}}$).³⁸
- Secondly the importance of the polarization of the pump and probe beams. When a sample is exposed to polarized light, molecules with absorption transition moments oriented along the electric vector of the incident light are preferentially excited. Hence a partially oriented excited-state population is created. Probing of this excited sample is therefore dependant on the polarization of the probe beam and the rearrangement of the excited volume within the pump-probe time delay. This directional dependence is known as *anisotropy*. The signal measured is therefore different when pump and probe beam polarizations are parallel (\parallel) or perpendicular (\perp) and the total signal intensity, I_T , is given by $I_{\parallel} + 2I_{\perp}$ (since $I_T = I_y + I_x + I_z$). Setting the angle between the pump and probe beam polarizations to 54.7° , the *magic angle*, removes the need to record I_{\parallel} and I_{\perp} separately.³⁹

- Finally, the propagation of a light wave through a medium is perturbed by permittivity (the resistance encountered when forming an electric field in the material). The velocity of light in a vacuum is a physical constant, c , but due to permittivity, light traveling through any given material travels slower. The refractive index, n , is a measure of how light is retarded in any given medium, and is given by speed of light in a vacuum divided by the speed of light in the medium. Since the refractive index is also a function of the frequency of light, different wavelengths of light have slightly different refractive indices and so propagate through media at different speeds. In general shorter wavelengths travel slower than longer wavelengths: $n(\lambda_{\text{blue}}) > n(\lambda_{\text{red}}) > 1$. The effect of this in a pulsed wave made up of different frequency components (*i.e.* pulsed laser light) is to spread the frequencies apart in time. This, *dispersion*, must therefore be avoided or minimized (by careful choice of components) in order to preserve a spectrometer's temporal resolution.⁴⁰

1.4.2. Time-Resolved Photoelectron Imaging Spectroscopy

The photoelectric effect^{41,42} describes the ejection of an electron from a system following the absorption of a photon of sufficient energy. As a probing technique, the probe pulse ionizes the excited state causing the release of an electron with a characteristic kinetic energy (eKE) related to the photon energy by:⁴³

$$h\nu = eBE + eKE \quad (1.18)$$

where $h\nu$ is the energy of the photon and eBE is the electron binding energy (*i.e.* the difference between the emitting electronic state and the first cationic state) of the probed state. As excited state population evolves with t , eBE and thus the detected eKE vary. Photoelectron spectroscopy is a very powerful technique, particularly as it may be used in the detection of optically dark and non-fluorescent states.⁴⁴

1.5. Photostability in Biologically Relevant Molecules

1.5.1. Introduction

Organic molecules are generally unstable when irradiated with ultraviolet (UV) light. The electronic excitation imparted by the absorption of UV photons often leads to the breaking of covalent bonds through population of dissociative states (as discussed in 1.2.4). It is perhaps remarkable then, given the high exposure of Earth to UV irradiation during biogenesis, that early life was able to flourish.⁴⁵ Indeed ~4 billion years on, with a fully formed UV filtering stratospheric ozone, UV radiation is still significant; the average daytime exposure to a human is on the order of 10^{18} photons per second. There is, and always has been, a significant pressure for *photostability* to be present in life's key building blocks (amino acids, DNA bases *etc.*). Indeed there may have been a type of natural selection for the molecular motifs we see today in nature. Photostability mechanisms involve the highly efficient deactivation of excited state population through the non-radiative processes described previously (1.2.2 and 1.2.3). Studying these mechanisms is therefore important not only in our understanding of the origins of life but also intellectually beneficial; knowledge in this field may be extended to other applications of photochemistry such as therapeutics and solar energy.

When seeking to understand the excited state dynamics of biologically important motifs, most early sub-picosecond time resolution experiments were performed under ultra-high vacuum in order to remove “unwanted” interactions with surrounding molecules.^{46,47} This simplistic approach has allowed for a vast collection of information on many small (~10 atoms) biologically important species and forms the first steps in the “bottom up” approach used in this field.⁴⁸ Of course the biological focus is pertinent because it calls for experiments that mimic real biological conditions. Hence, applying this knowledge garnered from experiments *in vacuo* toward real world problems requires one to also study the molecule's interaction with its surroundings. Besides this, the majority of photochemistry is concerned with the condensed phase anyway; solution and solid-state. In using solution-phase techniques such as TA

spectroscopy, the influence of solvent on molecular dynamics has started to be fully appreciated.^{46,47}

1.5.2. Phenol

As the chromophore of the amino acid tyrosine and an ideal model for several small aromatic species, phenol (structure shown in Figure 1.7 inset) has received considerable attention from both experimental⁴⁹⁻⁵⁸ and theoretical⁵⁹⁻⁶³ standpoints. It is particularly relevant to this thesis given its closely related structure to that of guaiacol (2-methoxyphenol), the subject of Chapter 3, and that it has been comparatively studied in both gas and solution phases. The photochemistry of phenol following excitation to the first excited state, S_1 , is now discussed.

1.5.2.1. Phenol in vacuo

Figure 1.7 shows the calculated one-dimensional PES of the ground state, S_0 ($^1\pi\pi$), and the first two singlet electronic excited states, S_1 ($^1\pi\pi^*$) and S_2 ($^1\pi\sigma^*$) of phenol along the O–H coordinate

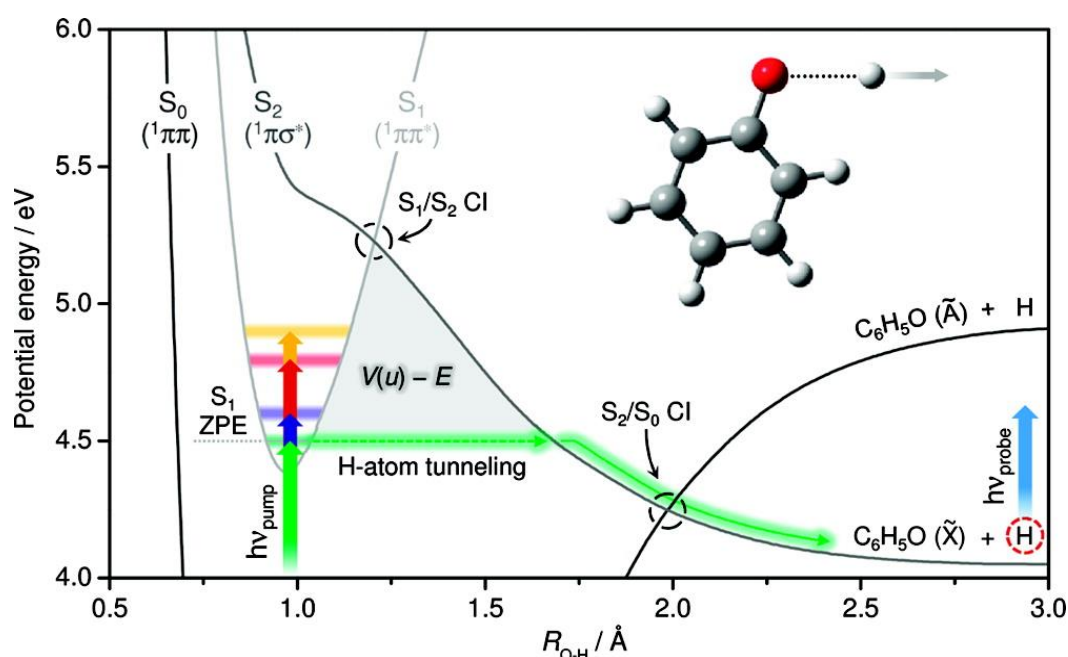


Figure 1.7 | Calculated potential energy cuts along the O–H coordinate of phenol for the first two electronic excited states, S_1 and S_2 , and the ground state, S_0 . Excitation ($h\nu_{\text{pump}}$) to the S_1 is shown for four different excitation wavelengths (green, blue, red and orange arrows). The grey shaded area, labelled $V(u) - E$, represents the potential barrier to H-atom tunnelling used in WKB tunnelling calculations. Following H-atom tunneling under the S_1/S_2 CI and O–H fission along S_2 , H-atoms are probed using fs pulses ($h\nu_{\text{probe}}$). Figure taken from ref. 58.

(R_{O-H}). Excitation of phenol with energies in the region of $275 > \lambda > 248$ nm (4.5 to 5 eV), as indicated by vertical arrows in Figure 1.7, leads to population of the optically bright S₁ state. Both the S₀ and S₁ are bound states of only π -character, *i.e.* only electrons of the π -system are involved. The S₂ state however, has σ character as it is formed from a $\sigma^* \leftarrow \pi$ transition and is repulsive with respect to the O–H coordinate due to the population of the σ^* anti-bonding molecular orbital. The importance of $\pi\sigma^*$ states in a plethora of other biomolecules was first highlighted by Sobolewski *et al.*⁶⁰ They postulated that the S₂ (¹ $\pi\sigma^*$) of phenol was critical in linking population from the optically bright S₁ back to the ground state. Indeed it can be seen from Figure 1.7 that the S₂ has CIs with both S₀ and S₁ states along the O–H coordinate.

As one may expect, excitation directly to the S₂ ($\lambda < 248$ nm) results in O–H fission on a femtosecond timescale.⁵⁶ However, the position of the S₁/S₂ CI, some 4000 cm⁻¹ above the ZPE of the S₁, creates a barrier for population transfer to the S₂ following excitation to the ZPE of the S₁ ($h\nu_{\text{pump}}$, green arrow Figure 1.7). Surprisingly perhaps, frequency domain measurements have shown that O–H fission from S₁ still persists.⁵⁰ Originally, two theses were formed to account for this: i) IC through high vibrational (O–H stretch) acceptor modes of the S₀ (termed S₀^{*}) allowing population transfer via an S₁ \rightarrow S₀^{*} \rightarrow S₂ pathway.^{50,64} ii) H-atom tunnelling under the S₁/S₂ CI to promote predissociation on the S₂.^{57,60,63} It has been shown that selective deuteration of the O–H bond of phenol (C₆H₅OD) increases the fluorescence lifetime of the S₁ ZPE level from ~2.4 ns to ~13.3 ns⁶⁵ and complete deuteration (C₆D₅OD) yields no D-atom signal from O–D scission of the S₂ state.⁵⁰ These paradigms alone did not exclusively reveal the favourability of either (i) or (ii). From Equation 1.17 it can be seen that the mass of the tunnelling particle has an inverse exponential proportionality to the tunnelling rate. D-atom tunnelling is ~10³ less probable than H-atom tunnelling.⁵⁷ However, the isotope effect ($k_{\text{H}}/k_{\text{D}}$) shown lies some way out of the typical range for tunnelling mechanisms (~10 to ~100)¹⁹: advocates of (i) hypothesized that the O–D stretch acceptor modes were less efficient for the S₁ \rightarrow S₀^{*} IC.

The first experimental measurement of the appearance dynamics for H-atoms formed *via* tunnelling under the S_1/S_2 CI came through the use of time-resolved photofragment spectroscopy – a technique that provides both temporal and energetic details of the O–H dissociation mechanism.⁵⁸ Roberts *et al.* were able to show that following excitation above the ZPE, whilst still below the S_1/S_2 CI, (such as $h\nu_{\text{pump}}$: blue, red and yellow arrows Figure 1.7) the same H-atom loss from the S_2 state is observed with little variance in the H-atom appearance lifetime.⁵⁸ If one considers a Fermi's golden rule model, in which the increased density of states at higher $h\nu_{\text{pump}}$ should promote faster IC, the insensitivity of the H-atom appearance lifetime to the excess energy imparted in the S_1 appears inconsistent with a pathway of $S_1 \rightarrow S_0^*$ IC (although it does not rule this out, *vide infra*).¹⁴ Indeed the *overall* lifetime of the S_1 excited Franck-Condon window (relaxing through any means *i.e.* $S_1 \rightarrow S_0$ IC and fluorescence, $S_1 \rightarrow S_2$ H-atom tunnelling and $S_1 \rightarrow T_n$ ISC) was shown to decrease with increasing $h\nu_{\text{pump}}$. The concepts of competing kinetics dictate that the H-atom appearance lifetime should echo that of the S_1 . However, experimental constraints, *viz.* the length of achievable pump-probe time delay and poor signal-to-noise, prevented Roberts *et al.* from observing such an effect. It may then be concluded that the time constants of all of the S_1 decay processes that contribute to the overall S_1 lifetime are similar *i.e.* $k_{\text{Tunnelling}} \approx (k_{\text{IC}} + k_{\text{Fluorescence}} + k_{\text{ISC}})$.

Elegantly, in an attempt to reconcile this coincidence of time constants, Roberts *et al.* used a one-dimensional WKB approximation (recall section 1.3.4.2) to estimate the S_1/S_2 H-atom tunnelling lifetime, $\tau_{\text{tunnelling}}$, at the ZPE. The energy of the barrier was obtained from the calculated potential energy shown in Figure 1.7 and led to the extraction of a $\tau_{\text{tunnelling}}$ value of 2.5 ns. This timescale very-accurately modelled the H-atom experimental data and matched previously reported S_1 excited state lifetimes.⁶⁵

1.5.2.2. Phenol in solution

The S_1 state photodynamics of phenol in solution were examined by Zhang *et al.*⁶⁶ with TA spectroscopy employing a wire-guided thin film liquid jet for sample delivery. The TA spectra

of a 10 mM solution of phenol in cyclohexane following excitation with 267 nm light are shown in Figure 1.8. This excitation energy (4.6 eV) will lead to population of the S_1 state above the ZPE but below the S_1/S_2 CI in the gas phase and it is assumed to be the same here in a weakly perturbing solution such as cyclohexane.

At early time delays (<1 ns, Figure 1.8a) the TA spectra are dominated by the ESA feature of the S_1 , which has characteristic broad peaks at 380, 475 and 600 nm. The assignment of S_1 ESA is backed up by the calculated $S_n \leftarrow S_1$ oscillator strengths (squared TDMs shown in Figure 1.8b) and the absorption profile previously reported by Hermann *et al.*⁶⁷ in cyclohexane at 100 ps. The authors were careful to include the contribution to the signal by the solvent, including solvent-only TA spectra in Figure 1.8a to illustrate that, in this case, it has minimal effects after 800 ps.

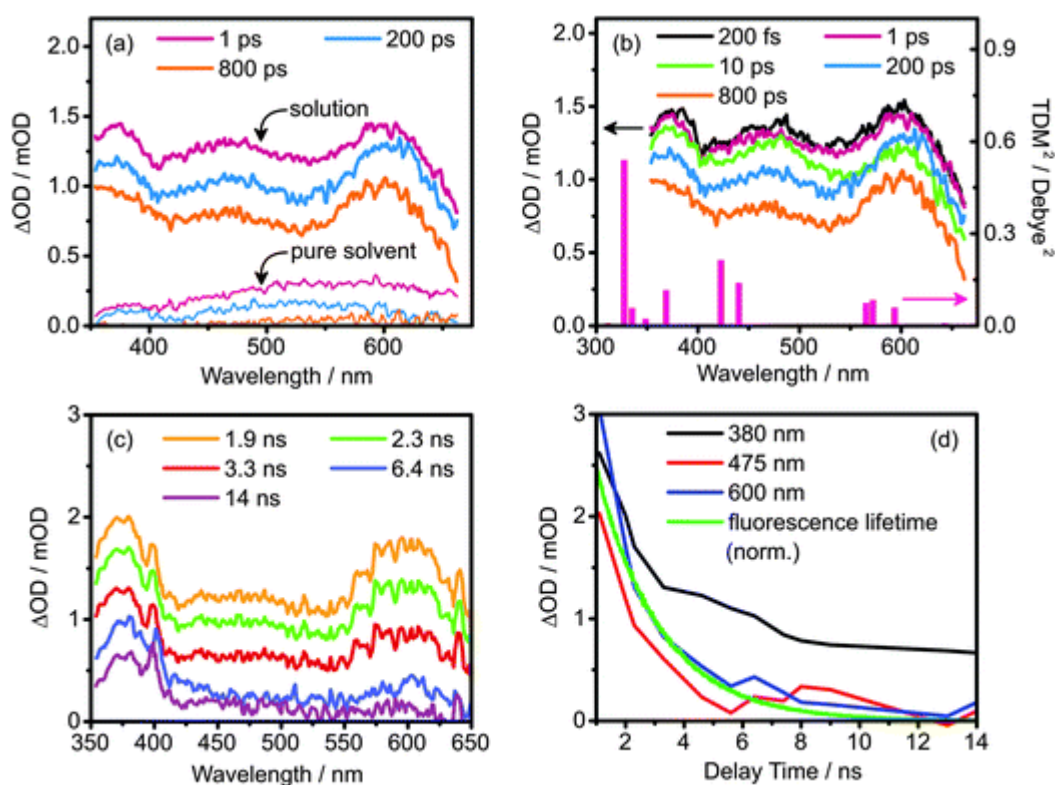


Figure 1.8 | (a-c) TA spectra of 10 mM solution of phenol in cyclohexane following 267 nm irradiation at various pump-probe delays with (a) including solvent only TA spectra for 1, 200 and 800 ps. (d) Transients at select wavelengths and S_1 fluorescence lifetime obtained from time-correlated single photon counting experiment. Figure

taken from ref. 66.

Continuing to later time delays, (Figure 1.8b and c) up to 14 ns, it is clear that the S_1 ESA decays and reveals the progressive appearance of a spectral signature assigned to the phenoxyl radical *i.e.* C_6H_5O from O–H dissociation. The transients taken at 475 and 600 nm (Figure 1.8d) show that the S_1 decays with a lifetime similar to the previously reported fluorescence lifetime^{68,69} and from that obtained here, using time-correlated single photon counting, of 2.1 ns. The kinetics of the 380 nm TA deviate from this observed S_1 lifetime due to the spectral overlap with the radical signature (~ 400 nm).

The solution-phase data presented is highly concordant with the data of previous gas-phase studies. Following the excitation of phenol to the S_1 , with 267 nm (4.6 eV) irradiation, rapid (solvent assisted) VET to the ZPE precedes S_1 deactivation by the same pathways as found *in vacuo*: $S_1 \rightarrow S_0$ IC and fluorescence, $S_1 \rightarrow S_2$ H-atom tunnelling and $S_1 \rightarrow T_n$ ISC. The observation of phenoxyl radicals on a ~ 2 ns timescale is congruent with an H-atom tunnelling mechanism under the S_1/S_2 CI. Furthermore the presence of solvent molecules (though relatively weakly interacting) would lead to much faster deactivation of vibrationally excited states such that the $S_1 \rightarrow S_0^* \rightarrow S_2$ notion for H-atom loss (rather than the $S_1 \rightarrow S_2$ H-atom tunnelling postulate) becomes more unlikely since the S_0^* would be effectively quenched, negating $S_0^* \rightarrow S_2$ IC.

It is most interesting to note that the solvent effect on PES energies at short R_{O-H} is minimal. Specifically it may be expected that the Rydberg character of the S_2 PES would be particularly prone to Pauli repulsion with solvent electron density, leading to an increase of the S_2 energy. Given the sensitivity of the tunnelling rate to barrier size (recall section 1.3.4.2), an increase in the energy of the S_1/S_2 CI due to solution would likely result in a vanishingly small phenoxyl radical yield and a significant change in the S_1 lifetime. The apparent agreement between gas- and solution-phase experiments in timescales of S_1 relaxation and the presence of H-atom or complementary phenoxyl radical signatures indicate that the tunnelling rate, and therefore tunnelling barrier, is not substantially changed.

This highlights how the chosen solvent, cyclohexane, is an excellent likeness to the environment of the gas phase due to its non-hydrogen-bonding character and low polarity.⁷⁰ This study of phenol is built upon in Chapter 3, where a gas- and solution-phase comparative study of guaiacol (2-methoxyphenol), is presented, in which we now observe a significant solvent effect.

1.6. Photoactivation for Therapy

1.6.1. Introduction

The unique photochemical properties of ruthenium-pyridyl complexes have been exploited for a plethora of technological and medicinal applications, such as: light-harvesting,^{71,72} light-emitting devices,⁷³⁻⁷⁵ fluorescence imaging^{76,77} and cytotoxic action.^{77,78} One of the more novel uses of these complexes is as photoactivatable prodrugs, where light induces formation of an active species from a stable, inert precursor molecule; a technique known by the term photodynamic therapy (PDT),⁷⁹ or more generally as photochemotherapy. PDT has the obvious benefit of spatial control, limiting the possible side effects to the immediate area of tissue,^{80,81} and also has the potential to generate unique reactive species that might otherwise be biologically incompatible *i.e.* caged delivery.⁸²⁻⁸⁴

1.6.2. Tris(bipyridine)ruthenium(II) chloride

Perhaps the most heavily studied inorganic chromophores are polypyridyl complexes of ruthenium(II), of which, the archetypal tris-(2,2'-bipyridine)ruthenium(II), or $[\text{Ru}(\text{bpy})_3]^{2+}$, is a member.⁸⁵ Numerous experimental and computational studies of $[\text{Ru}(\text{bpy})_3]^{2+}$ have revealed that its photophysics hinges around a manifold of near-degenerate metal-to-ligand charge-transfer triplet states (³MLCT) formed by ultrafast intersystem crossing (ISC) from the initially photo-populated (singlet) ¹MLCT state.⁸⁶⁻⁸⁸ The 'averaged' ³MLCT state therefore involves electron transfer from a metal d-orbital to the π^* orbital of one of the bipyridine (bpy) ligands and is formally termed $[\text{Ru}^{\text{III}}(\text{bpy})_2(\text{bpy}^-)]^{2+}$. At a similar energy to this ³MLCT state, lies the lowest energy

triplet metal-centred (^3MC , d-d ligand field) state, the accessibility of which is dependent on solvent and temperature.⁸⁹ The ^3MC state is known to exhibit significant distortions of the geometry relative to the ground state or that of the MLCT states,⁹⁰ and therefore an increased ligand labilization. For fully bidentate-chelated complexes such as $[\text{Ru}(\text{bpy})_3]^{2+}$, this dissociation channel is not usually a high yielding relaxation pathway^{91,92} and such complexes primarily decay radiatively back to the ground state from the $^3\text{MLCT}$ and/or ^3MC states.⁸⁸ When one of the bpy ligands is replaced, for example, by two monodentate pyridines (or related aromatic heterocycles, L) to form a complex of the class $[\text{Ru}(\text{bpy})_2(\text{L}')(\text{L}'')]^{2+}$, a solvent substitution reaction may ensue, depending on the nature of the solvent.⁹³ As such, the replacement of an L ligand with a solvent molecule (solvolysis), following photodetachment, may provide a further excited state deactivation mode. The relative ordering of the energies of the $^3\text{MLCT}$ and ^3MC states becomes variable depending on the polar and steric effects of the substituent ligand, L.⁸⁹ It has been postulated that in order to create complexes with high photoproduct quantum yields (*i.e.* those which undergo ligand dissociation), the ^3MC state must be made the lowest energy excited state or thermally accessible from the $^3\text{MLCT}$ state.⁸⁹

1.6.3. Photoactive Ruthenium Complexes

Several novel transition metal complexes with charge-transfer transitions have been shown to be photoactive including complexes of iron,⁹⁴ osmium,⁹⁵ rhodium,⁹⁶ platinum⁹⁷ and ruthenium.⁹⁸⁻¹⁰⁰ For all these complexes, there is only a limited understanding of the photochemistry and photophysics that underpins their transformation from the inert to the active species. To date, limited time-resolved spectroscopic and computational studies have been conducted on photoactivatable complexes of this type.^{98,101-104} Such investigations may provide fundamental understanding of the mode(s) of activation;

highlighting inefficiencies in the photoreaction of these complexes and so aid the design of more efficacious complexes, ultimately delivering improved healthcare technologies.

Turro and co-workers have studied the ultrafast dynamics of the bipyridyl ruthenium acetonitrile complex $cis-[Ru(bpy)_2(CH_3CN)_2]^{2+}$ following photoexcitation at 310 nm, in both water and acetonitrile solutions.¹⁰² For aqueous transient UV/Vis absorption experiments at early times (<10 ps), typical absorption features of the 3MLCT excited state and an absorption, assigned to a pentacoordinated Ru(II) intermediate (PCI), *i.e.* $[Ru(bpy)_2(CH_3CN)]^{2+}$, were observed. Due to the near simultaneous appearance of these features, and the relatively slow decay (~50 ps) of the 3MLCT signature, the authors proposed a kinetic picture of direct formation of the PCI from the initially populated singlet states (MLCT and/or $\pi\pi^*$ ligand centred). The PCI may then recombine with its original partner ligand or, especially in the case of aqueous solutions, undergo solvolysis (ligand exchange with a solvent molecule). Importantly, Turro and co-workers observed an absorption peak at 458 nm, appearing after 10 ps, which they assigned to the monoaqua complex, *i.e.*, $[Ru(bpy)_2(CH_3CN)(H_2O)]^{2+}$.¹⁰²

More recently, Lamberti and co-workers have carried out a combined experimental and theoretical study, using transient X-ray and visible absorption spectroscopies, and time-dependent density functional theory calculations to unravel the 3MLCT excited state structure of $cis-[Ru(bpy)_2(py)_2]^{2+}$ (py = pyridine).¹⁰⁴ Their results showed that there is little reorganization of the geometry from the ground state to the 3MLCT state; only a small shortening of the Ru–N(bpy) bonds. Calculations of the 3MC state, however, showed a significant lengthening of one of the Ru–N(py) bonds and minimal re-optimizations of the bpy ligands. The transient X-ray absorption data provided experimental verification of the 3MLCT structure, but experimental determination of the 3MC geometries remains a challenge. The small intensity and energy differences in the transient visible absorptions between the ground state and mono-aquated photoproduct,

cis-[Ru(bpy)₂(py)(H₂O)]²⁺, made accurate determination of the dissociation time of the pyridine ligand difficult, with an estimated dissociation time of <3 ns after excitation.

Depending on the size of the labile ligands and the nature of the extended solvent structure, it can be expected that there will be an ensemble of PCI species with their geminate partners having various degrees of separation.¹⁰⁵ These nascent photodetached ligands and partnering PCI complexes, surrounded by a solvation shell, can be classed as *caged* species and may either geminately reform the original complex or undergo (some degree) of diffusional separation, with the relative propensities for these processes depending on the exact nature of the system. In systems that undergo separation (or where the ligand is initially ejected through the solvation shell, *e.g.* smaller ligands), photodetached ligands may in principle still re-encounter the PCI complex, but after a longer diffusional period, to afford diffusive recombination.

To date, no work has placed an emphasis on understanding the structural changes surrounding the PCI of a [Ru(bpy)₂(L')(L'')]²⁺ type complex during ligand solvolysis and the impact of caging on the degree of solvolysis (*i.e.* the quantum yield for formation of the mono-aquated species), which will undoubtedly contribute to its efficacy as a pro-drug. To this end, in Chapter 4, we have investigated the structural and photochemical properties of the novel ruthenium complex, *cis*-[Ru(bpy)₂(NA)₂]²⁺ (NA = nicotinamide, pyridine-3-carboxamide).

1.7. Bibliography

- (1) Zewail, A. H. *Angew. Chem., Int. Ed.* **2000**, 39, 2586.
- (2) Hilborn, R. C. *American Journal of Physics* **1982**, 50, 982.
- (3) Klán, P.; Wirz, J. In *Photochemistry of Organic Compounds*; John Wiley & Sons, Ltd: 2009, p 25.
- (4) Lakowicz, J. R. *Principles of Fluorescence Spectroscopy*; 3rd ed.; Springer: New York, 2006.
- (5) Owirutsky, J. C.; Raftery, D.; Hochstrasser, R. M. *Annu. Rev. Phys. Chem.* **1994**, 45, 519.
- (6) Reid, K. L. *Int. Rev. Phys. Chem.* **2008**, 27, 607.
- (7) Boyall, D.; Reid, K. L. *Chem. Soc. Rev.* **1997**, 26, 223.

-
- (8) Atkins, P. W.; Friedman, R. *Molecular Quantum Mechanics*; OUP Oxford, 2011.
- (9) Trout, T. J.; Velsko, S.; Bozio, R.; Decola, P. L.; Hochstrasser, R. M. *J. Chem. Phys.* **1984**, *81*, 4746.
- (10) Zinth, W.; Kolmeder, C.; Benna, B.; Irgens-Defregger, A.; Fischer, S. F.; Kaiser, W. *J. Chem. Phys.* **1983**, *78*, 3916.
- (11) Graener, H. *Chem. Phys. Lett.* **1990**, *165*, 110.
- (12) Aßmann, J.; Kling, M.; Abel, B. *Angew. Chem., Int. Ed.* **2003**, *42*, 2226.
- (13) Child, S. *Molecular Collision Theory*; Dover Publications, 2012.
- (14) Beddard, G.; Fleming, G.; Gijzeman, O.; Porter, G. *Chem. Phys. Lett.* **1973**, *18*, 481.
- (15) Englman, R.; Jortner, J. *Mol. Phys.* **1970**, *18*, 145.
- (16) Born, M.; Oppenheimer, R. *Annalen der Physik* **1927**, *389*, 457.
- (17) Eckart, C. *Physical Review* **1934**, *46*, 383.
- (18) Hollas, J. M. *Modern Spectroscopy*; John Wiley & Sons, 2004.
- (19) Limbach, H.-H.; Lopez, J. M.; Kohen, A. *Philos. Trans. R. Soc., B* **2006**, *361*, 1399.
- (20) Hedley, G. J.; Ruseckas, A.; Samuel, I. D. W. *J. Phys. Chem. A* **2008**, *113*, 2.
- (21) Duan, H.-S.; Chou, P.-T.; Hsu, C.-C.; Hung, J.-Y.; Chi, Y. *Inorg. Chem.* **2009**, *48*, 6501.
- (22) McCusker, J. K. *Acc. Chem. Res.* **2003**, *36*, 876.
- (23) Steinhurst, D. A.; Baronavski, A. P.; Owrutsky, J. C. *Chem. Phys. Lett.* **2002**, *361*, 513.
- (24) Berera, R.; Grondelle, R.; Kennis, J. M. *Photosynth. Res.* **2009**, *101*, 105.
- (25) Holt, N. E.; Zigmantas, D.; Valkunas, L.; Li, X.-P.; Niyogi, K. K.; Fleming, G. R. *Science* **2005**, *307*, 433.
- (26) Wan, C.; Fiebig, T.; Schiemann, O.; Barton, J. K.; Zewail, A. H. *Proc. Natl. Acad. Sci. U. S. A.* **2000**, *97*, 14052.
- (27) Wan, C.; Xia, T.; Becker, H.-C.; Zewail, A. H. *Chem. Phys. Lett.* **2005**, *412*, 158.
- (28) Crespo-Hernández, C. E.; Cohen, B.; Kohler, B. *Nature* **2005**, *436*, 1141.
- (29) Schwalb, N. K.; Temps, F. *Science* **2008**, *322*, 243.
- (30) Bach, U.; Lupo, D.; Comte, P.; Moser, J.; Weissörtel, F.; Salbeck, J.; Spreitzer, H.; Grätzel, M. *Nature* **1998**, *395*, 583.
- (31) De, S.; Pascher, T.; Maiti, M.; Jespersen, K. G.; Kesti, T.; Zhang, F.; Inganäs, O.; Yartsev, A.; Sundström, V. *J. Am. Chem. Soc.* **2007**, *129*, 8466.
- (32) Pensack, R. D.; Banyas, K. M.; Barbour, L. W.; Hegadorn, M.; Asbury, J. B. *Phys. Chem. Chem. Phys.* **2009**, *11*, 2575.
- (33) Kovalenko, S.; Ruthmann, J.; Ernsting, N. *Chem. Phys. Lett.* **1997**, *271*, 40.
- (34) Ernsting, N.; Schmidt, R.; Brauer, H. *J. Phys. Chem.* **1990**, *94*, 5252.
- (35) Attar, A. R.; Blumling, D. E.; Knappenberger Jr, K. L. *J. Chem. Phys.* **2011**, *134*, 024514.
-

-
- (36) Yamaguchi, Y.; Maruyama, S. *Chem. Phys. Lett.* **1998**, 286, 336.
- (37) Polli, D.; Altoè, P.; Weingart, O.; Spillane, K. M.; Manzoni, C.; Brida, D.; Tomasello, G.; Orlandi, G.; Kukura, P.; Mathies, R. A. *Nature* **2010**, 467, 440.
- (38) Ziolk, M.; Naskrecki, R.; Karolczak, J. *Opt. Commun.* **2004**, 241, 221.
- (39) Lakowicz, J. R. In *Principles of Fluorescence Spectroscopy*; Lakowicz, J. R., Ed.; Springer US: 2006, p 353.
- (40) Maciejewski, A.; Naskrecki, R.; Lorenc, M.; Ziolk, M.; Karolczak, J.; Kubicki, J.; Matysiak, M.; Szymanski, M. *J. Mol. Struct.* **2000**, 555, 1.
- (41) Hertz, H. *Wiedemann's Annalen* **1887**, 31, 983.
- (42) Einstein, A. *Ann. Phys* **1905**, 17, 132.
- (43) Carlson, T. A. *Annu. Rev. Phys. Chem.* **1975**, 26, 211.
- (44) Neumark, D. M. *Annu. Rev. Phys. Chem.* **2001**, 52, 255.
- (45) Sobolewski, A.; Domcke, W. *Phys. Chem. Chem. Phys.* **2010**, 12, 4897.
- (46) Crim, F. F. *Nature Chem.* **2011**, 3, 344.
- (47) Crim, F. F. *Faraday Discuss.* **2012**, 157, 9.
- (48) Staniforth, M.; Stavros, V. G. *Proc. R. Soc. A* **2013**, 469, 20130458.
- (49) Tseng, C.-M.; Lee, Y. T.; Ni, C.-K. *J. Chem. Phys.* **2004**, 121, 2459.
- (50) Nix, M. G. D.; Devine, A. L.; Cronin, B.; Dixon, R. N.; Ashfold, M. N. R. *J. Chem. Phys.* **2006**, 125, 133318.
- (51) Ashfold, M. N. R.; Cronin, B.; Devine, A. L.; Dixon, R. N.; Nix, M. G. D. *Science* **2006**, 312, 1637.
- (52) Tseng, C.-M.; Lee, Y. T.; Lin, M.-F.; Ni, C.-K.; Liu, S.-Y.; Lee, Y.-P.; Xu, Z. F.; Lin, M. C. *J. Phys. Chem. A* **2007**, 111, 9463.
- (53) Ashfold, M. N.; Devine, A. L.; Dixon, R. N.; King, G. A.; Nix, M. G.; Oliver, T. A. *Proc. Natl. Acad. Sci. U. S. A.* **2008**, 105, 12701.
- (54) Nix, M.; Devine, A.; Dixon, R.; Ashfold, M. *Chem. Phys. Lett.* **2008**, 463, 305.
- (55) Hause, M. L.; Heidi Yoon, Y.; Case, A. S.; Crim, F. F. *J. Chem. Phys.* **2008**, 128, 104307.
- (56) Iqbal, A.; Cheung, M. S. Y.; Nix, M. G. D.; Stavros, V. G. *J. Phys. Chem. A* **2009**, 113, 8157.
- (57) Dixon, R. N.; Oliver, T. A. A.; Ashfold, M. N. R. *J. Chem. Phys.* **2011**, 134, 194303.
- (58) Roberts, G. M.; Chatterley, A. S.; Young, J. D.; Stavros, V. G. *J. Phys. Chem. Lett.* **2012**, 3, 348.
- (59) Sobolewski, A. L.; Domcke, W. *J. Phys. Chem. A* **2001**, 105, 9275.
- (60) Sobolewski, A.; Domcke, W.; Dedonder-Lardeux, C.; Jouvet, C. *Phys. Chem. Chem. Phys.* **2002**, 4, 1093.
- (61) Lan, Z.; Domcke, W.; Vallet, V.; Sobolewski, A. L.; Mahapatra, S. *J. Chem. Phys.* **2005**, 122, 224315.
- (62) Abe, M.; Ohtsuki, Y.; Fujimura, Y.; Lan, Z.; Domcke, W. *J. Chem. Phys.* **2006**, 124, 224316.
-

-
- (63) An, H.; Baeck, K. K. *J. Phys. Chem. A* **2011**, *115*, 13309.
- (64) Sur, A.; Johnson, P. M. *J. Chem. Phys.* **1986**, *84*, 1206.
- (65) Ratzer, C.; Küpper, J.; Spangenberg, D.; Schmitt, M. *Chem. Phys.* **2002**, *283*, 153.
- (66) Zhang, Y.; Oliver, T. A. A.; Ashfold, M. N. R.; Bradforth, S. E. *Faraday Discuss.* **2012**, *157*, 141.
- (67) Hermann, R.; Mahalaxmi, G. R.; Jochum, T.; Naumov, S.; Brede, O. *J. Phys. Chem. A* **2002**, *106*, 2379.
- (68) Berlman, I. *Handbook of Florescence Spectra of Aromatic Molecules*; Elsevier, 2012.
- (69) Bent, D.; Hayon, E. *J. Am. Chem. Soc.* **1975**, *97*, 2599.
- (70) Moelwyn-Hughes, E. A.; Thorpe, P. L. *Proc. R. Soc. London, A* **1964**, *277*, 423.
- (71) Grätzel, M. *Inorg. Chem.* **2005**, *44*, 6841.
- (72) Frischmann, P. D.; Mahata, K.; Wurthner, F. *Chem. Soc. Rev.* **2013**, *42*, 1847.
- (73) Rudmann, H.; Rubner, M. F. *J. Appl. Phys.* **2001**, *90*, 4338.
- (74) Holder, E.; Langeveld, B. M. W.; Schubert, U. S. *Adv. Mater.* **2005**, *17*, 1109.
- (75) Rudmann, H.; Shimada, S.; Rubner, M. F. *J. Am. Chem. Soc.* **2002**, *124*, 4918.
- (76) Fernandez-Moreira, V.; Thorp-Greenwood, F. L.; Coogan, M. P. *Chem. Commun.* **2010**, *46*, 186.
- (77) Gill, M. R.; Thomas, J. A. *Chem. Soc. Rev.* **2012**, *41*, 3179.
- (78) Yadav, A.; Janaratne, T.; Krishnan, A.; Singhal, S. S.; Yadav, S.; Dayoub, A. S.; Hawkins, D. L.; Awasthi, S.; MacDonnell, F. M. *Mol. Cancer Ther.* **2013**, *12*, 643.
- (79) Dougherty, T. J. In *Photodynamic Therapy: Methods and Protocols*; Gomer, C. J., Ed.; Humana Press Inc: Totowa, 2010; Vol. 635, p 1.
- (80) Mroz, P.; Yaroslavsky, A.; Kharkwal, G. B.; Hamblin, M. R. *Cancers* **2011**, *3*, 2516.
- (81) Agostinis, P.; Berg, K.; Cengel, K. A.; Foster, T. H.; Girotti, A. W.; Gollnick, S. O.; Hahn, S. M.; Hamblin, M. R.; Juzeniene, A.; Kessel, D.; Korbelik, M.; Moan, J.; Mroz, P.; Nowis, D.; Piette, J.; Wilson, B. C.; Golab, J. *Ca-Cancer J. Clin.* **2011**, *61*, 250.
- (82) Ciesienski, K. L.; Hyman, L. M.; Yang, D. T.; Haas, K. L.; Dickens, M. G.; Holbrook, R. J.; Franz, K. J. *Eur. J. Inorg. Chem.* **2010**, *2010*, 2224.
- (83) Sgambellone, M. A.; David, A.; Garner, R. N.; Dunbar, K. R.; Turro, C. J. *Am. Chem. Soc.* **2013**, *135*, 11274.
- (84) Zayat, L.; Calero, C.; Alborés, P.; Baraldo, L.; Etchenique, R. *J. Am. Chem. Soc.* **2003**, *125*, 882.
- (85) Watts, R. J. *J. Chem. Educ.* **1983**, *60*, 834.
- (86) Van Houten, J.; Watts, R. J. *J. Am. Chem. Soc.* **1976**, *98*, 4853.
- (87) Damrauer, N. H.; Cerullo, G.; Yeh, A.; Boussie, T. R.; Shank, C. V.; McCusker, J. K. *Science* **1997**, *275*, 54.
-

-
- (88) Durham, B.; Caspar, J. V.; Nagle, J. K.; Meyer, T. J. *J. Am. Chem. Soc.* **1982**, *104*, 4803.
- (89) Wagenknecht, P. S.; Ford, P. C. *Coord. Chem. Rev.* **2011**, *255*, 591.
- (90) Juris, A.; Balzani, V.; Barigelletti, F.; Campagna, S.; Belser, P.; von Zelewsky, A. *Coord. Chem. Rev.* **1988**, *84*, 85.
- (91) Durham, B.; Walsh, J. L.; Carter, C. L.; Meyer, T. J. *Inorg. Chem.* **1980**, *19*, 860.
- (92) Van Houten, J.; Watts, R. J. *Inorg. Chem.* **1978**, *17*, 3381.
- (93) Pinnick, D. V.; Durham, B. *Inorg. Chem.* **1984**, *23*, 1440.
- (94) Roy, M.; Chakravarthi, B. V. S. K.; Jayabaskaran, C.; Karande, A. A.; Chakravarty, A. R. *Dalton Trans.* **2011**, *40*, 4855.
- (95) Sun, Y.; Joyce, L. E.; Dickson, N. M.; Turro, C. *Chem. Commun.* **2010**, *46*, 6759.
- (96) Lutterman, D. A.; Fu, P. K. L.; Turro, C. *J. Am. Chem. Soc.* **2005**, *128*, 738.
- (97) Mackay, F. S.; Woods, J. A.; Heringova, P.; Kasparkova, J.; Pizarro, A. M.; Moggach, S. A.; Parsons, S.; Brabec, V.; Sadler, P. J. *Proc. Natl. Acad. Sci. U. S. A.* **2007**, *104*, 20743.
- (98) Betanzos-Lara, S.; Salassa, L.; Habtemariam, A.; Novakova, O.; Pizarro, A. M.; Clarkson, G. J.; Liskova, B.; Brabec, V.; Sadler, P. J. *Organometallics* **2012**, *31*, 3466.
- (99) Gabrielsson, A.; Zális, S.; Matousek, P.; Towrie, M.; Vlček, A. *Inorg. Chem.* **2004**, *43*, 7380.
- (100) Singh, T. N.; Turro, C. *Inorg. Chem.* **2004**, *43*, 7260.
- (101) Salassa, L.; Garino, C.; Salassa, G.; Gobetto, R.; Nervi, C. *J. Am. Chem. Soc.* **2008**, *130*, 9590.
- (102) Liu, Y.; Turner, D. B.; Singh, T. N.; Angeles-Boza, A. M.; Chouai, A.; Dunbar, K. R.; Turro, C. *J. Am. Chem. Soc.* **2009**, *131*, 26.
- (103) Salassa, L.; Borfecchia, E.; Rui, T.; Garino, C.; Gianolio, D.; Gobetto, R.; Sadler, P. J.; Cammarata, M.; Wulff, M.; Lamberti, C. *Inorg. Chem.* **2010**, *49*, 11240.
- (104) Borfecchia, E.; Garino, C.; Salassa, L.; Rui, T.; Gianolio, D.; Zhang, X.; Attenkofer, K.; Chen, L. X.; Gobetto, R.; Sadler, P. J.; Lamberti, C. *Dalton Trans.* **2013**, *42*, 6564.
- (105) Harris, A. L.; Brown, J. K.; Harris, C. B. *Annu. Rev. Phys. Chem.* **1988**, *39*, 341.



2.1. The Laser System Overview

A schematic of the laser table, which accommodates the laser system, an optical parametric amplifier (Light Conversion, *TOPAS-C*) and a separate experiment's beam paths, is shown in Figure 2.1. The commercially available laser system is used to generate the fundamental beam and entails the following. A Ti:sapphire (Ti:Al₂O₃) oscillator¹ (Spectra-Physics, *Tsunami*) produces pulses (4.7 nJ/pulse, 0.37 W) centred at 800 nm, with an ~80 fs pulse duration and a 76 MHz repetition rate. The oscillator is pumped by the 4 W, 532 nm output from a frequency-doubled, continuous wave (CW) Nd:YVO₄ diode laser (Spectra-Physics, *Millenia*). Amplification of the oscillator pulses is performed through the use of a chirped regenerative amplifier (Spectra-Physics, *Spitfire XP*). The oscillator output or “seed” pulses are first stretched temporally (chirped) to yield a pulse duration of the order of picoseconds. 1 in 76,000 pulses of the seed pulse train are amplified in a second Ti:sapphire crystal, which is pumped by the ~20W, 527 nm output from a frequency doubled, pulsed Nd:YLF laser (Spectra-Physics, *Empower*). Following this, amplified pulses are recompressed to provide a short-pulse duration. The final output consists of a femtosecond pulse train centred at 800 nm with the power of 3 mJ/pulse and a repetition rate of 1 kHz. The pulses have a Gaussian spectral shape where the FWHM is ~500 cm⁻¹ and a Gaussian temporal shape with a pulse duration (FWHM) of ~40 fs. The beam has a Gaussian beam profile with an intensity FWHM of ~12 mm, but this is reduced

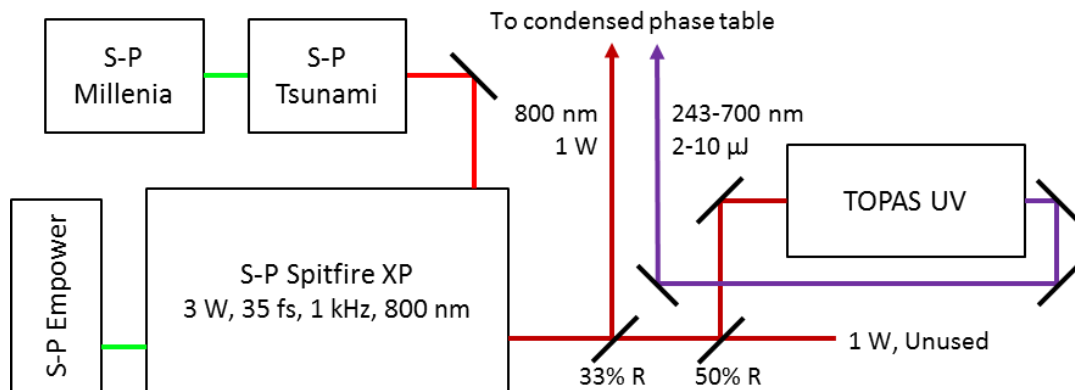


Figure 2.1 | Schematic of the optical table containing the laser system and TOPAS.

to ~8 mm via a reflective telescope, an intensity FWHM required by the optical parametric amplifier.

The 3 W fundamental is then divided into three 1 W beams by incidence with first 33% and then 50% partially reflective 800 nm dichroic mirrors (LAYERTEC Optische). The first portion (i) becomes the fundamental for the transient absorption (TA) setup, the second portion (ii) pumps a TOPAS-C (see Section 2.3.4.2) and the third (iii) is used in a separate setup. Parts (i) and (ii) are then guided off this table and onto the TA setup table.

2.2. Generation of Ancillary Light

The energy required to excite our target molecules to their lowest optically bright states ($\pi^* \leftarrow \pi$ and $\pi^* \leftarrow d$ transitions in biomolecules and ruthenium complexes, respectively) far exceeds the photon energy of the 800 nm fundamental. Consequently frequency up-conversion is required to generate UV photons for the excitation of our target molecules. Additionally the excited state population of such species is probed using the absorption of UV/visible (UV/Vis) photons. Therefore, several processes are required to convert our malapropos fundamental into useful frequencies; particularly the generation of UV/Vis pump frequencies (240 to 400 nm) and a continuum of UV/Vis probe frequencies (340 to 740 nm). The following sections briefly describe the processes used to generate said light.

2.2.1. Nonlinear Optical Transformations

When light travels through a transparent material, the electric field component will have some effect on the induced dipole moment or dielectric polarization of that medium. The amplitude by which the medium's polarisation \mathbf{P} is perturbed by the incident electric field \mathbf{E} is given by the electric susceptibility χ such that:

$$\mathbf{P} = \epsilon_0 \chi \mathbf{E} \quad (2.1)$$

where ε_0 is the vacuum permittivity. Whilst this expression is usually sufficient when concerning low field strengths, it is a simplification and not appropriate for high field strengths that are characteristic of pulsed lasers. In this event, when the electric field intensity of the propagating light becomes comparable to the dielectric polarization, a power series of Equation 2.1 may be used to model the *nonlinear susceptibility*^{2,3}:

$$\begin{aligned} \mathbf{P} &= \varepsilon_0 \left(\chi^{(1)} \mathbf{E} + \chi^{(2)} \mathbf{E} \mathbf{E} + \chi^{(3)} \mathbf{E} \mathbf{E} \mathbf{E} \dots \chi^{(n)} \mathbf{E}^n + \dots \right) \\ &= \left(\mathbf{P}^{(1)} + \mathbf{P}^{(2)} + \mathbf{P}^{(3)} + \dots \mathbf{P}^{(n)} + \dots \right) \end{aligned} \quad (2.2)$$

where $\chi^{(n)}$ is the n^{th} order nonlinear susceptibility and $\mathbf{P}^{(n)}$ is the n^{th} order nonlinear polarization. Each of the electric fields in Equation 2.2 may correspond to different frequency components *i.e.* sum or difference frequency generation.

2.2.1.1. Second-Order Nonlinear Processes

As an example of a nonlinear optical process, we consider a simplified representation of second-harmonic generation (SHG). An optical electric field with a frequency ω and amplitude \mathbf{E}_ω :

$$\mathbf{E}_\omega(t) = \mathbf{E}_0 \sin(\omega t) \quad (2.3)$$

interacting with an asymmetric medium with a non-zero second-order susceptibility $\chi^{(2)}$, has a second-order polarization represented as:

$$\mathbf{P}^2(t) = \varepsilon_0 \chi^{(2)} \mathbf{E}_0^2 \sin^2 \omega t = \frac{1}{2} \chi^{(2)} \mathbf{E}_0^2 (1 - \cos 2\omega t) \quad (2.4)$$

Hence, for an electric field \mathbf{E}_ω oscillating with frequency ω , the polarization oscillates at the second harmonic 2ω . The medium is able to radiate photons of twice the incident light's frequency and may be thought of as the summation of two photons of the same frequency to yield one photon ω_2 of twice that of the initial two *i.e.* $\omega_1 + \omega_1 = \omega_2$. SHG is a specific

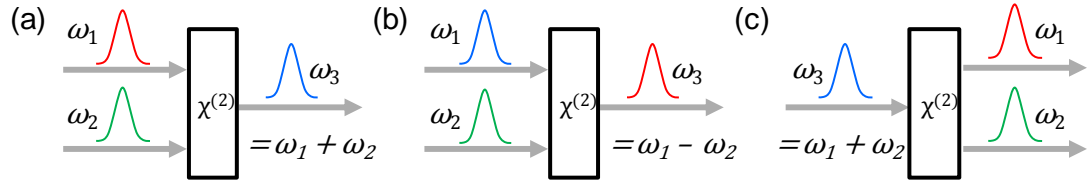


Figure 2.2 | Second order nonlinear optical process for generating pulses of new frequencies. (a) SFG, (b) DFG, (c) OPG.

degenerate case of sum-frequency generation (SFG). As stated above the driving electric fields may have different frequencies, thus a more general case may be described as $\omega_1 + \omega_2 = \omega_3$. Difference-frequency generation (DFG) may be used to mix pump waves of similar frequencies to yield longer wavelengths *i.e.* $\omega_1 - \omega_2 = \omega_3$. The last second order nonlinear process we consider is optical parametric generation (OPG). OPG can be considered as the opposite of SFG and is capable of producing two photons whose sum energy is equal to the initial photons *i.e.* $\omega_3 = \omega_1 + \omega_2$. The nonlinear behaviour described here is summarized in Figure 2.2.

The $\chi^{(2)}$ medium used must meet particular constraints in order to favour particular combinations of frequencies such as phase-matching of the incident and produced photon waves so that they do not destructively interfere. The phase-matching of two incident beams may be with perpendicularly polarized (Type-I) or orthogonally polarized (Type-II) light.⁴ Second-order nonlinearity is only observed in asymmetric (no centre of inversion) materials; if \mathbf{P} changes symmetrically with \mathbf{E} , then the even terms in Equation 2.2 become zero.³

2.2.1.2. Supercontinuum Generation

When a pulsed laser is loosely focused into a transparent medium the typical photon densities easily become great enough to elicit higher order nonlinear effects. One of the most spectacular phenomena in nonlinear optics is the spectral broadening of femtosecond pulses to produce continua *i.e.* supercontinuum generation (SCG). The broadening on the blue (anti-Stokes) side of the seed pulse is significantly larger than that of the red (Stokes) side; SCG is typically used to transform near-IR light into a broadband white light continuum as illustrated in Figure 2.3. Various media can be used to produce white-light with little variance in the overall

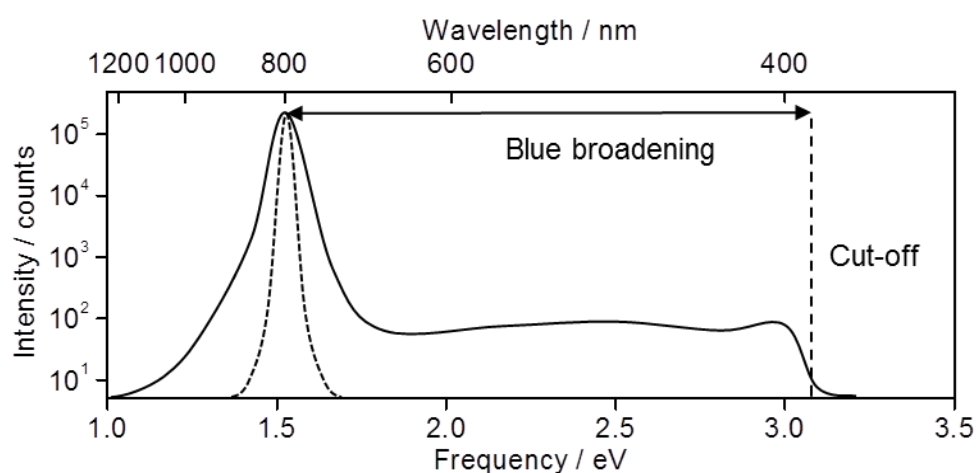


Figure 2.3 | Illustration of the typical shape of a white-light continuum spectrum generated from the broadening of an IR seed pulse (dashed peak).

broadened spectrum seen, except for the position of the cut-off frequency. The conception of a complete model for SCG remains a field of research^{5,6} but a number of nonlinear, mostly third-order, effects are known to contribute.⁷ The use of SCG for the broadband white-light probe and optimization is outlined in Section 2.3.3.

2.3. The TA Setup

The design and construction of the TA spectroscopy setup forms a major part of this thesis and is described in detail within this chapter. Whilst TA setups are relatively common amongst research groups worldwide, and indeed such apparatus has become commercially available, this section of the thesis should prove insightful for other “builders” and researchers wishing to emulate or build upon the studies in the ensuing chapters. A particular advantage of this setup is the use of a wire-guided thin-film liquid jet (2.3.7.). Unless otherwise specified, all optomechanics used in this setup use standard catalogue items from ThorLabs Inc. (*e.g.* a typical mirror mount is constructed from parts: *KM100*, *TR75/M*, *PH75/M*, *BA1S/M*). Generally, the setup uses 25.4 mm diameter, circular optics unless otherwise stated. Specific optics are designated with bolded labels (*e.g.* lens **L1**) and are catalogued in Section 2.3.5.

2.3.1.1. Periscope and Beam Drawbridge

The optical table that houses the laser system and the optical table housing the TA setup have different table top heights, so periscopes are used to alter the beam heights between them. The periscopes are placed on the table housing the laser system, immediately before sending the beam off of the table toward the TA setup. A hinged span of square tubing is used to join between the enclosures of each optical table so that the beam is fully enclosed. This ‘beam drawbridge’ can be raised to allow laboratory operators access between the tables when the beams are inactive. On entering the TA setup the beam height is 182 mm, and this remains unvaried throughout.

2.3.2. Table Layout

Apart from the laser system and the periscope described *supra*, all beam lines are guided atop the optical table housing the TA setup (Figure 2.4). The table (Newport Corp., *MST Series Table Top & R-2000 Series LabLegs*) measures 90 × 180 cm and has an enclosure constructed of aluminium T-slotted profiles with black acrylic side panels and lids that has the internal dimensions of (W) 174 × (D) 80 × (H) 37 cm. The table layout is shown in detail in Figure 2.4.

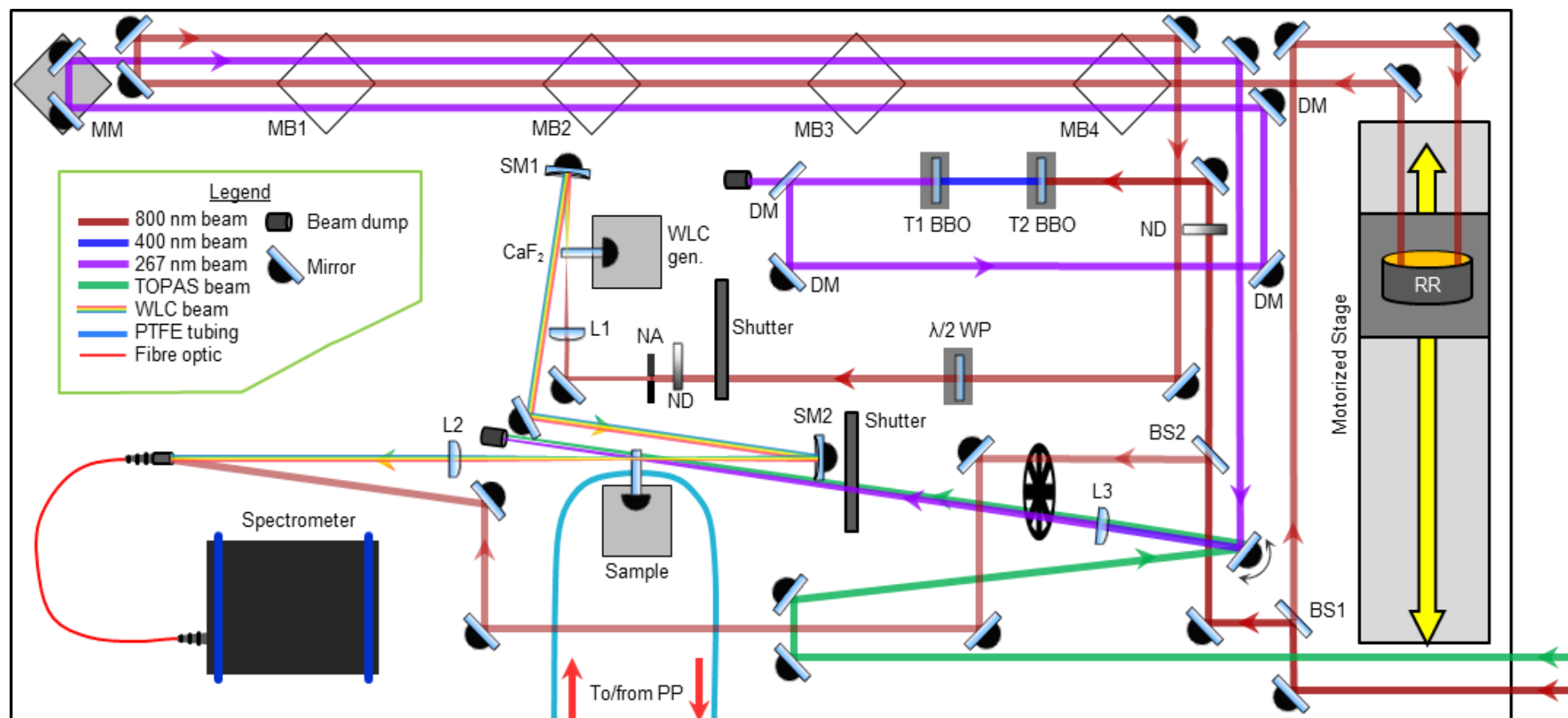


Figure 2.4 | Schematic of the TA setup drawn to scale. Legend of labelled optics may be found in Section 2.3.5. PP – peristaltic pump.

2.3.3. Broadband White-Light Probe

2.3.3.1. Beam Path

The white-light continuum (WLC) probe path, from its generation to detection, is summarily shown in Figure 2.5 and described in detail as follows.

Transmission of 5% of the fundamental beam through a 95:5 beamsplitter (**BS1**), yields the ‘WLC seed’. The WLC seed is passed through a variable delay stage (see Section 2.3.6.1) then a half-waveplate ($\lambda/2$ **WP**) set to 27° or 333° ,^{††} corresponding to p- or s-polarized pump light, respectively. In this way the waveplate changes the polarization of the seed-WLC, and thus WLC,⁸ to be 54.7° (‘magic angle’)⁹ with respect to that of pump, ensuring that anisotropy (rotational) effects are not measured. This angle may of course be varied to accommodate transient anisotropy measurements but such effects are not addressed within this thesis.

The WLC seed is then passed through a graduated neutral density filter (**ND**), an iris (numerical aperture) and focused into the CaF_2 window using a lens (**L1**). The neutral density filter and iris are used to attenuate the power density at focus to control the SCG process and give a stable WLC. Following SCG in the CaF_2 window the expanding WLC is collimated with a spherical (concave) mirror (**SM1**), passed through a colour-compensating filter (**F**), and focussed into the sample using a second spherical mirror (**SM2**). The use of spherical mirrors and/or thin optics, between the point of SCG and sample, is important to minimize the chirp of the WLC to

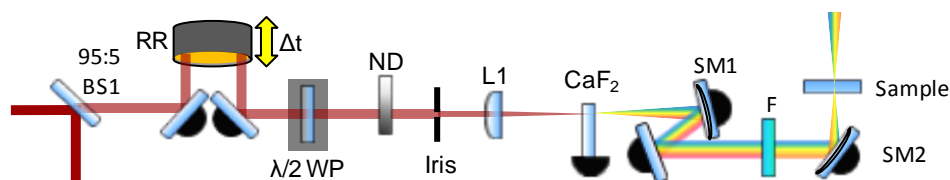


Figure 2.5 | A summarized white-light continuum probe generation beam path. BS – beamsplitter, RR – retroreflector, $\lambda/2$ WP – half-waveplate, ND – neutral density filter, L – lens, SM – spherical mirror, F – filter,

^{††}For linearly polarized light a half-wave plate rotates the polarization vector through an angle 2θ , where θ is the optical axis tilt angle.

maintain temporal resolution and ease chirp correction measurements (a larger chirp requires more data points around $t = 0$, thus increases scan durations).

2.3.3.2. CaF_2 Translation

As discussed previously, several different materials may be used to generate white-light probe pulses. Each material has its own merits in terms of the continua that may be produced using them and the ease of use. We have used both sapphire and CaF_2 windows successfully but elected to use 1 mm thick CaF_2 in gathering the results contained within this thesis. The significant advantage of CaF_2 over the other commonly used glass media is the deep blue cut-off to blue broadening, allowing us to generate probe energies up to 3.6 eV (340 nm). CaF_2 has a relatively low damage threshold and we find that after ~30 seconds of pumping, the WLC becomes highly unstable and any duration after a minute, SCG ceases completely. Due to this, the glass is continuously vertically translated to ensure that a single spot is not over-pumped. This arrangement, shown in Figure 2.6, consists of a vertically mounted linear translation stage, to which the SCG optomechanics are attached. The translation stage is moved by a piezo linear

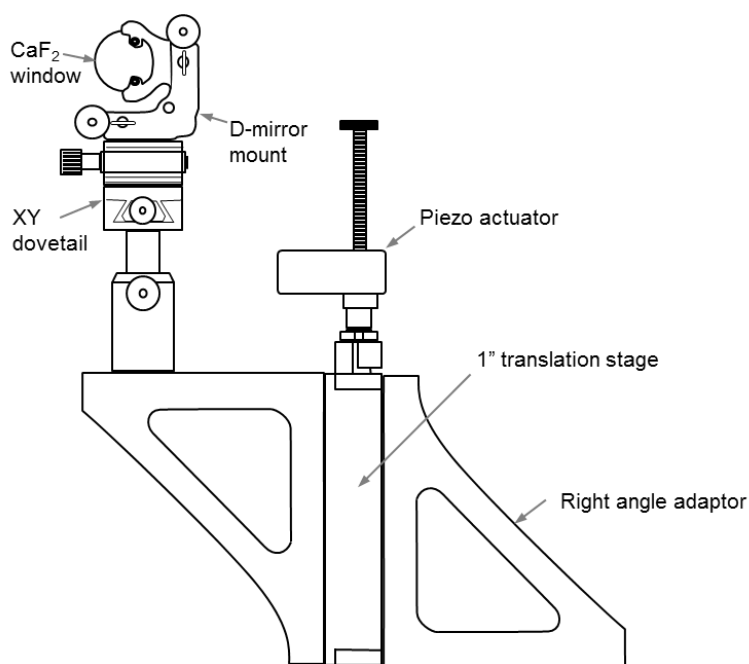


Figure 2.6 | A 25 mm translation stage mounted vertically translates the CaF_2 window continuously. From the position shown, the platform may move 25 mm (though only 12 mm is used) up before reversing direction.

actuator (Newport Corp., *Picomotor Actuator*, 8303) driven by a homebuilt controller (commercially available equivalent: Newport Corp., *PCB-Mountable Single-Axis Picomotor Driver*, 8712). This is programmed to provide 12 mm of automated translation of the stage in a continuous raster-fashion *i.e.* from the starting position, the stage moves 12 mm in the positive, then 12 mm in the negative and repeats indefinitely. Only 12 mm of travel is used as we elect to translate through an arc of the CaF_2 window rather than the full diameter. This is because the WLC produced is then reflected back at a very acute angle off of **SM1** (see Figure 2.4), to avoid optical aberrations introduced when reflecting off of such mirrors at appreciable angles. Using the edge of the window prevents the WLC clipping it on the return pass. The translation speed required to prevent WLC instability is a remarkably low ~ 3 mm/hr.

2.3.3.3. Optimisation Routine

Optimisation of the WLC may be achieved through variation of the intensity of the WLC seed, its beam width at focus and position (depth) of the focus into the CaF_2 window. These are controlled through a combination of the ND filter, iris and XY dovetail stage. A simple routine to produce a stable WLC for this system is as follows:

1. Ensure the WLC seed is perpendicular with the CaF_2 window by checking the back reflection is collinear with the seed.
2. Starting with the focus behind the CaF_2 window, the ND fully shut (OD=3, power ~ 50 pJ) and the iris diameter set to 3 mm, move the CaF_2 window toward the focus until faint broadening (orange/red blurring, Figure 2.7a) of the beam of the WLC-seed occurs. If no change is observed, incrementally repeat with higher intensity (adjust the ND filter).
3. Increase the intensity by opening the ND filter until a SCG is observed – this will appear as a yellow/orange/pink filament (Figure 2.7b).
4. Open iris until a red/purple halo appears around a white filament (Figure 2.7c).

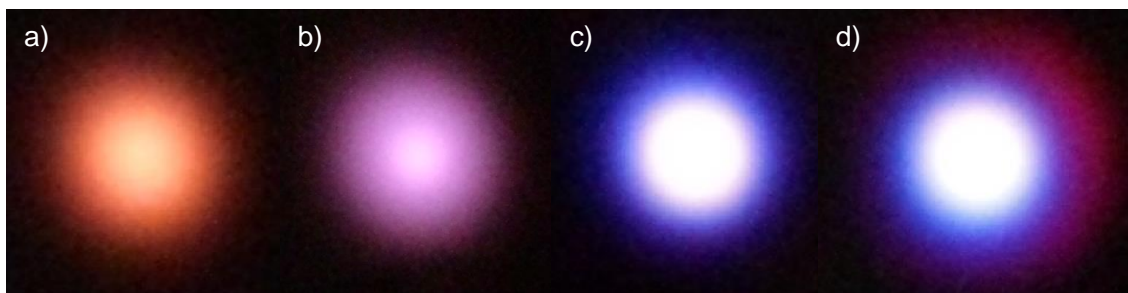


Figure 2.7 | Pictures of WLC imaged on white card during optimisation, where a) and b) have too low a power density, c) is optimal and d) is over-pumped. *Nota bene* the red/purple halo around c) is not clear from this image and appears as a much fainter, perfectly symmetrical version of the halo seen in d).

5. Adjust the ND filter and iris as required to yield the least shot noise as measured by the shot-to-shot root mean square noise (described below)

Figure 2.7 shows the result of the SCG. A clean off-white central filament (Figure 2.7c) is usually indicative of high quality white light. Intermittent speckling of the red halo that appears around this (Figure 2.7d) is indicative of too high a power density.

2.3.3.4. WLC Spectrum

Due to the intensity of the residual WLC seed (800 nm) this must be removed to ensure that it does not interact with the sample. To do this a colour compensating filter (HOYA, *CM-500*) is placed in the WLC beam. This also removes a significant amount of the red-region of the WLC spectrum, but has the advantage over commonly available shortpass filters in that it does not absorb in the blue/ultraviolet region and the deep-blue WLC is thus preserved. The filtered WLC spectrum is shown in Figure 2.8.

The root mean square error, calculated from the difference in intensities between sequential shots, *i.e.*:

$$RMSE = \sqrt{\frac{1}{n} \sum (I_1 - I_2)^2} \quad (2.5)$$

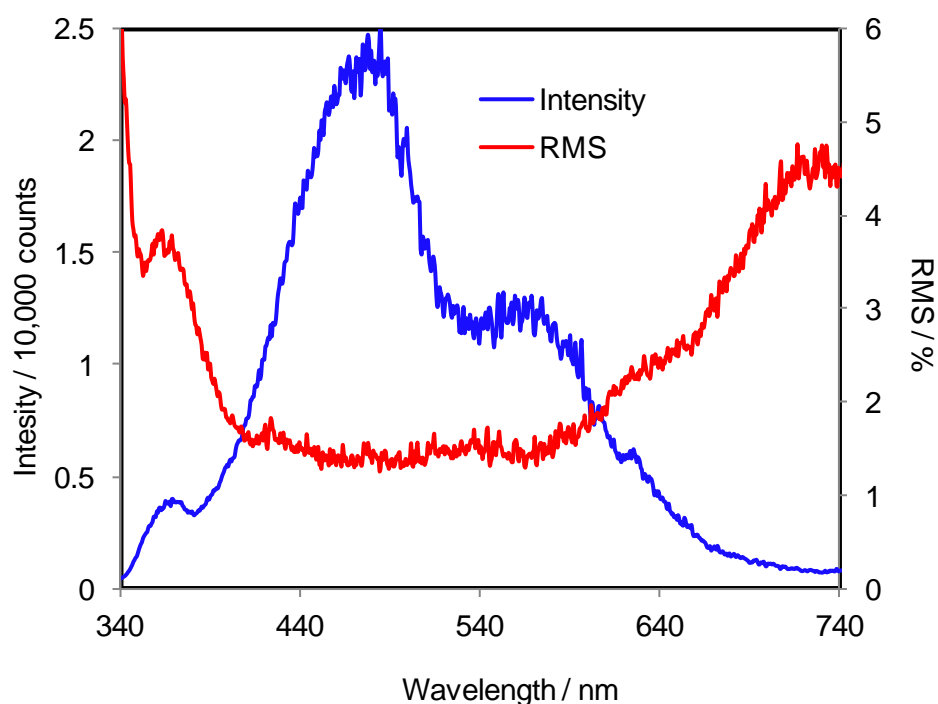


Figure 2.8 | Spectra of the filtered WLC and its RMS noise.

where, n is number shots and I_1 and I_2 are intensities, for a pair of sequential pulses – is used as a measure of the WLC stability when optimizing the system. This error is displayed as a percentage of the shot intensity, shown in Figure 2.8. It is usually the aim of the optimisation routine to keep this noise below 2% for all wavelengths except the far extremes of the WLC.

2.3.4. Pump Sources

We employ two sources of light to excite our molecules. The harmonics of our fundamental provide the highest power density (and beam quality) and are therefore useful when exciting sample that is weakly absorbing. The use of an optical parametric amplifier allows the user selection of practically any excitation wavelength required.

2.3.4.1. Harmonic Stage

SFG is used to convert our fundamental 800 nm into 400 and 267 nm light, using the nonlinear medium beta-barium borate (β -BaB₂O₄, BBO). The phase-matching of the produced radiation with the driving fields is achieved with angle-tuning of the BBO crystal. The details of the harmonic stage, which constitutes two BBO crystals (CASTECH Crystals, Inc, 1" mounted, 8

mm diameter), are given in Table 2.1 and include the properties of the BBO crystals and the light produced.

Table 2.1 | Details of the harmonic stage used to generate pump wavelengths of 800, 400 and 267 nm.

	BBO Properties			Light properties			
Harmonic of Fundamental	Phase Matching Type	Crystal cut angle	Crystal thickness	Wavelength (Energy)	Mixed Frequencies	Polarization	Typical Power
1 st	N/A	N/A	N/A	800 nm (12500 cm ⁻¹)	N/A	P	900 mW
2 nd	Type I	$\theta = 29.2^\circ$, $\phi = 0$	300 μm	400 nm (25000 cm ⁻¹)	$2 \times \omega_{800 \text{ nm}}$	S	300 mW
3 rd	Type II	$\theta = 55.5^\circ$, $\phi = 30^\circ$	200 μm	267 nm (50000 cm ⁻¹)	$\omega_{800 \text{ nm}} + \omega_{400 \text{ nm}}$	P	1.2 mW

The use of dichroic mirrors (see 2.3.5) is required to remove the mixed frequencies from the produced beam. This is done using four reflections off of dichroic mirrors that are highly reflective for either 400 nm or 267 nm, depending on which is used.

2.3.4.2. TOPAS

Further pump wavelengths may be provided with the use of an optical parametric amplifier (Light Conversion, TOPAS-C). The TOPAS uses a combination of the second order nonlinear processes, described above, to generate pump wavelengths in the range 243 – 2000 nm (5.1 – 0.6 eV).

2.3.5. Optics

2.3.5.1. Lenses

Table 2.2 | Lenses used in the setup

Label	Form	Focal Length	Diameter	Material	Manufacturer	Part No.
L1	Plano-Convex	50 mm	12.7 mm	CaF ₂	Thorlabs Inc.	LA5183
L2	Plano-Convex	200 mm	25.4 mm	CaF ₂	Thorlabs Inc.	LA5714
L3	Plano-Convex	500 mm	25.4 mm	CaF ₂	Thorlabs Inc.	LA5464

2.3.5.2. Mirrors

Table 2.3 | Reflective optics used in the setup

Label	Details	Manufacturer	Part No.
AIM	Protected Aluminium Enhanced UV	CVI Laser Optics	PAUV-PM-1037-C
AgM	Silflex MKII, High Reflectivity Silver	Optics Balzers	BD10308105
DM1	Dichroic – Front Side: >99.9% R 800 nm; Rear Side: uncoated	Layertec optische	#100715
DM2	Dichroic – Front Side: >99% R 267 nm, <10% R 400 + 800 nm; Rear Side: <0.5% AR 400 + 800 nm	Layertec optische	#102854
DM3	Dichroic – Front Side: >99.9% R 400 nm, <2% R 800 nm; Rear Side: <1% AR 800 nm	Layertec optische	#101271
SM1	Spherical concave, $f = 50.8$ mm, enhanced aluminium	Edmund Optics	#43-538
SM2	Spherical concave, $f = 203.2$ mm, enhanced aluminium	Edmund Optics	#49-611

R – Reflective, AR – Antireflective, f – Focal Length

2.3.5.3. Other

Table 2.4 | Miscellaneous optics used in the setup

Label	Description	Manufacturer	Part No.
ND	Circular ND Filter 60 mm Dia 0.04-3.0 Optical Density	Edmund Optics	54-081
BS1	Dichroic Beamsplitter – 95% R 800 nm	Layertec optische	#108742
BS2	CaF ₂ circular window, 1 mm thick, 25.4 mm diameter	UQG optics	-
RR	Hollow Gold Retroreflector, 50.8 mm Clear Aperture, 1 Arcsec	Edmund Optics	#49-674

2.3.6. Optomechanics

2.3.6.1. Motorized Delay Stage

The WLC seed is passed through a variable optical delay stage to vary its path length with respect to that of the pump beam. In this way the pump-probe time delay is created. The stage consists of a motorized translation stage (Physik Instrumente, *M-531.DD High Precision Linear Translation Stage*) driven by a motor controller (Physik Instrumente, *C-863 Mercury Servo Controller*) with a hollow gold retroreflector (**RR**) mounted atop the stage. The specifications of the translation stage allow a minimum incremental step size, *i.e.* the smallest change in pump-probe delay, t , of 0.7 fs and a maximum pump-probe delay of 2 ns. It is also important to note that the low pitch and yaw qualities of this translation stage coupled with the low pointing deviation of the retroreflector (1 arcsec) mean that when the delay stage is correctly aligned, with the incident and (retro-) reflected beam perfectly parallel with the axis of movement (in both vertical and horizontal planes), no deviation in beam pointing is detectable. This is verifiable in three ways: (i) placement of a 50 μm diameter iris at the focus of the WLC probe (in place of the sample); deviation will give a diffraction pattern of the exiting beam, (ii) optimization of pump-probe signal at early t , then re-optimization should not be possible at the

limit of t , and (iii) the WLC spectral intensity should not vary from end-to-end of the delay stage.

2.3.6.2. Delay Lines

Larger delays, $>2\text{ns}$, may be created through use of a secondary delay line, in the pump beam, constituting paired mirrors mounted on magnetic bases. The default position of these mirrors, as shown in Figure 2.4, corresponds to $t \approx 0$, with the equivalent delay line in the WLC seed required to match beam path lengths. Shortening of the pump beam path, by moving the paired mirrors to magnetic bases that are positioned to give increments of 2 ns, allows pump-probe delays of up to 10 ns (translation stage, 2 ns + magnetic base delay loop, 8 ns). Each time this is done, pump-probe overlap must be reattained.

2.3.6.3. Chopper

For the detector to record ‘pump-on’ and ‘pump-off’ probe intensities, an optical chopper is used to block sequential pump pulses. The chopper (Thorlabs, *MC1000A*) consists of a motor driven 10-slot chopping blade that rotates at 50 Hz, so that at 1 kHz laser repetition rate, every-other pump pulse is blocked. Consequently a sequence of probe pulses, as detected with the spectrometer (see Section 2.3.8), will comprise half ‘pump-on’ probe pulses and half ‘pump-off’ probe pulses.

2.3.6.4. Shutters

Mechanical shutters placed in the WLC-seed and pump beam paths are required for pump-only or probe-only measurements and may also be used between data acquisitions to reduce sample degradation. These homebuilt shutters are repurposed from moving-arm hard disk drives (3.5-inch form factor) with a design based loosely upon that of Maguire and co-workers.¹⁰ Their function requires application of a $\pm 5\text{ V}$ potential to the hard drive’s magnetic voice coil to move the reader arm to either the positive or negative limit. Attached to this moving arm is a sheet of heat resistant plastic that acts as a suitable beam block. Control of the $\pm 5\text{ V}$ potential, and thus

position of the beam block (either open or closed), is carried out using a multifunction data-acquisition (DAQ) card (National Instruments, *USB-6009 DAQ*), a homebuilt amplifier/logic gate unit, and LabVIEW software running on the system PC.

To elaborate, the DAQ card is connected via USB to the PC system, which runs the LabVIEW program (see Section 2.3.8) and may vary the voltage of the DAQ card's analogue output channels, in the range of 0 to 5 V. A homebuilt amplifier/logic gate unit is then required, firstly, to amplify signal current from 5 mA to the 1 A required to drive the voice coil, and secondly, to interpret the input signal as either high or low and output either +5 or -5 V. The logic circuit interprets $0 < V < 2.5$ as low and $2.5 < V < 5$ as high and produces -5 V or +5 V potentials, respectively. In this way it is simple to programmatically control the shutters using the LabVIEW program (Section 2.3.8.3).

2.3.7. Sample Delivery

In the very simplest of sample delivery methods a quartz cuvette, of the type commonly used in static UV/Vis absorption spectrometers, may be employed. However, the 1 kHz laser repetition rate ensures that irradiated sample will not be entirely replaced by new sample molecules through diffusion alone. This is problematic if the excited state lifetimes approach milliseconds, photoproduct is generated or photodegradation occurs. For this reason, sample is recirculated continuously.

2.3.7.1. Peristaltic Pump

Sample recirculation is carried out using a peristaltic pump (Masterflex, *L/S Economy Variable-Speed Drive WZ-07554-90* with *L/S rigid PTFE-Tubing Pump Head WZ-77390-00*) that accepts PTFE tubing (Masterflex, *PTFE tubing set 4 mm ID 6 mm OD WZ-77390-60*). This is greatly advantageous over normal soft-polymer walled tubing as PTFE is chemically resistant to almost all solvents and chemical compatibility is therefore not an issue. The flow rate of the peristaltic

pump is high enough to provide fresh sample for each shot in either of the following delivery methods.

2.3.7.2. Wire-guided Thin Film Liquid Jet

A wire-guided thin film liquid jet of the type described by Tauber and co-workers¹¹ is employed in the experiment in Chapter 3. Significant differences between the two designs exist, however, and the liquid jet, shown in Figure 2.9, is described in detail as follows. The setup utilises an upper and lower reservoir; the lower reservoir serves as a sample vat and the upper reservoir provides hydrostatic pressure to drive the liquid through the jet. The upper reservoir is mounted on a tall post that may be adjusted in height to provide variable hydrostatic pressure and thus control of the flow rate through the jet. The upper reservoir is constructed of a (8.5 mm ID, 10 mm OD, 80 mm long) glass cylinder with four (1 mm long, 2.5 mm ID, 4 mm OD) ports, to which PTFE tubing (3.2 mm ID) may be attached (with some coercion) to form a tight seal. The four ports are required for: an inlet from the pump, a penstock to feed the jet, an overflow to

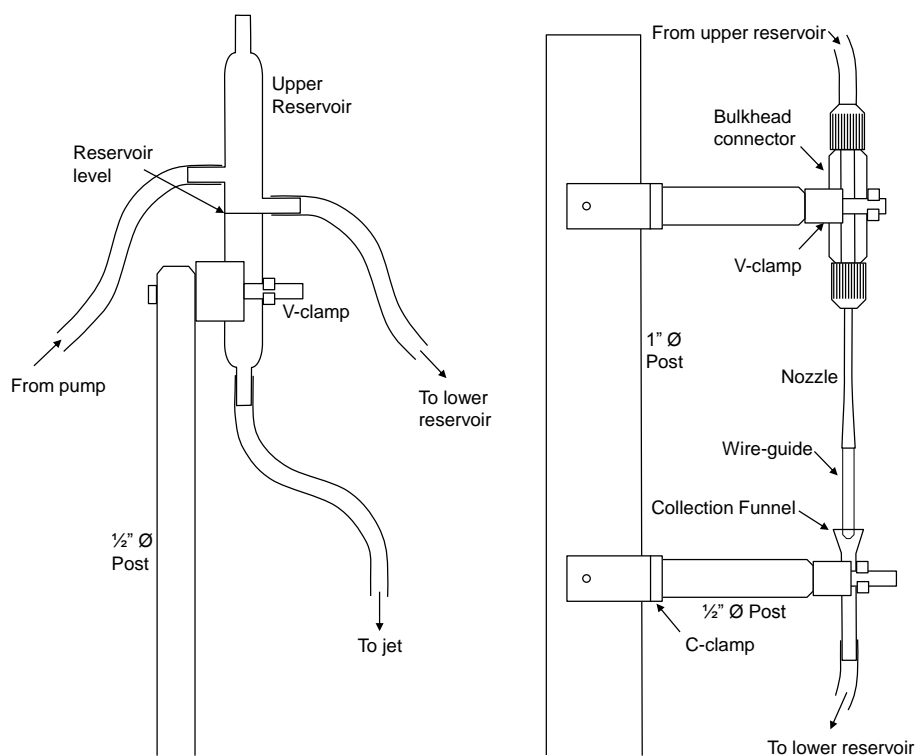


Figure 2.9 | Left: upper reservoir, right: wire-guided thin film liquid jet setup.

maintain a constant reservoir level, and a vent to prevent pressurisation. The placement of the ports make an invertible design that provides two different reservoir volumes and thus further variability of the hydrostatic pressure.

The liquid jet ‘nozzle’ comprises a 4 cm long stainless steel tube (Small Parts @Amazon.com, *stainless steel 304 hypodermic round tubing, gauge 14, 2.1 mm OD, 1.83 mm ID*), taper-crimped into a slit at one end from which a loop of wire (Goodfellow Cambridge Ltd, *molybdenum wire, 200 μm thick*) protrudes. Various sizes of tubes and wire thickness have been used but those stated here have given the best results. A procedure to reliably make quality nozzles is as follows:

1. A ~5 cm length of molybdenum wire, which is used due to its inert and malleable character, is bent into a loop by hand.
2. The ends of the loop are held ~3.5 mm apart and clamped with a pair of smooth jaw-faced flat nose pliers.
3. Using a 3 mm hex key inside the loop and the pliers held firmly shut, the wire is tensioned to force the wires straight and parallel.
4. The wire should now hold a U-shape. The ends are pulled slightly apart, so as to maintain the straightness of the wire, but to add a slight splaying (*i.e.* slight V-shape)
5. Stainless steel tubes are cut to length (4 cm) and edges are deburred using increasingly finer grades of glass paper. The inside and ends are then polished using glass fibres.
6. The tubes are then placed in a vice with angled jaw faces. These are purpose-made smooth faces with a 2.5° angle, such that the occluding angle is 5° .
7. The tube is crimped slightly so that it becomes oval shaped at one end.
8. A 2 mm wide, 300 μm thick metal shim (made by crushing a 150 μm thick walled steel tube) is held in the very end of the tube while it is crimped further to form a slit. The shim prevents the tube closing in on itself in the middle and forming an hourglass shape.

9. The ends of the wire are inserted in the gaps between the shim and the end of the slit.
The slight splaying of the wires holds them in place.
10. The tube may be crimped further, first with and then without the shim in place, until the wires are pinched in place.

The nozzle is connected to the upper reservoir using PTFE tubing and a bulkhead connector (Cole-Parmer, *Union connector; bulkhead; tube OD, 1 to 4 mm, EW-31320-85*). A film may be formed by engaging the peristaltic pump and filling the upper reservoir to the reservoir level. Sometimes, a slight pressure may be added, by blocking the vent, to encourage flow through the penstock and bulkhead connector. Once flow out of the nozzle is established, a pair of tweezers, closed loosely around the nozzle, is dragged from the top to the bottom of the wire to form a film between the two wires. A purpose-built glass collection funnel is mounted below to collect sample and feed this back to the lower reservoir. To prevent dripping, which causes ripples on the film, the tip of the wire loop is positioned in near-contact to the inside of the funnel; a static globule of sample forms and facilitates smooth run-off from the film.

An extra stable post, to which the whole liquid jet is mounted, is itself mounted on a 25 mm travel XYZ stage. This allows the precise positioning of the film in relation to the pump-probe overlap, and selection of the area on the film that is to be probed. This is important as the film is rarely uniformly flat and an optimum location, which does not lens or disperse the beam, must be selected.

Tauber and co-workers¹¹ found the thickness of the film to be dependent on the height of the upper reservoir above the nozzle; the thickness decreases as from the top to the bottom of the wire guide. Apart from the upper ~2 mm, the film reported here varies little across its length, and is measured through absorbance to be ~125 μm . The height of the upper reservoir noticeably changes the speed of the film and is used to balance this flow rate and the film's stability.

Finally a bipartite Perspex box with dimensions $60 \times 20 \times 20$ mm is used to enclose the film. The box has cut-outs that let it fit around the nozzle and collection funnel, and slits in the front and back panels to allow the laser beams to pass through unobstructed. Enclosing the film in this manner is important not only to minimize drafts and maintain film stability, but also to create a positive vapour pressure around the film to decrease evaporation of volatile solvents. Significant evaporation of the solvent can present a safety problem, so the entire laser table enclosure is vented with an external extraction line.

2.3.7.3. Flow-Through Cell

A 1 mm path length quartz flow through cell (Starna UK, *45/Q/1*) is employed for experiments in Chapter 4. For future experiments this has been replaced with a disassemblable cell (Harrick Scientific, *demountable liquid cell, DLC-S25*) using 1 mm thick front and 2 mm thick back CaF_2 windows. This has the advantages of variable path lengths and is easily cleaned. Either Viton or Kalrez O-rings are used for chemical compatibility with all solvents used.

2.3.8. System Control, Data Acquisition and Analysis

2.3.8.1. Fibre-Coupled Spectrometer

After the white light has probed the sample and is collimated (**L2**), it is collected into a fibre-optic cable fibre and passed to the spectrometer. The collection lens (Avantes Ltd, collimating lens for UV/VIS/NIR, *COL-UV/VIS-FCPC*) attaches directly to the fibre-optic cable (Avantes Ltd, *fibre cable, 200 μm , 2 m length, FC-UV200-2-FCPC*), which in turn attaches to the spectrometer (Avantes Ltd, *dual channel Avaspec-Fast, ULS1650F-2-USB2*). The spectrometer has two channels to enable white-light normalization and greater flexibility, however, only one channel is used for the experiments in this thesis and from hereon it is treated as a single channel spectrometer. The spectrometer uses a symmetrical Czerny-Turner layout comprising of a 50 μm entrance slit, a ruled diffraction grating blazed at 300 nm and a 2048 pixel linear CCD (Sony, *ILX554*). This gives the detector a bandwidth of ~ 0.5 nm and 340 to 800 nm spectral range.

The spectrometer is operated in store-to-RAM mode which, for a single ‘scan’, collects a burst of shots (pulses) before uploading the data to the PC *via* USB2. The integration time is set to a 1 ms and it is in this simple way the burst mode is timed; a TTL trigger is received by the spectrometer and then it integrates 1 ms shots continuously until the RAM is full. The number of pixels used is reduced to 813, corresponding to a probe window of 340 to 800 nm. This allows the number of shots per scan to be increased to 2500. The data packet sent to the PC, for one average at one pump-probe delay, is thus an array of 2500 lines of 813 pixels.

2.3.8.2. Chopper Reference Beam

The method of triggering the spectrometer does not differentiate ‘pump-on’ *versus* ‘pump-off’ shots and thus when the difference spectrum is calculated, its polarity may be flipped depending on whether the ‘pump-on’ shots are odd or even lines in the data array. A ‘chopper reference beam’ (ChopRef) produced from a weak reflection (<5 %) of a CaF₂ window (**BS2**) in the 800 nm pump beam, is sent through the chopper and onto the fibre-optic collection lens. The spectrometer thus receives a 500 Hz optical signal that is used to indicate the state (pump-on or pump-off) of the chopper for a given shot.

2.3.8.3. LabVIEW Programming

A purpose-created program, known as a virtual instrument (VI), is responsible for controlling the setup and is coded using the National Instruments LabVIEW 8.6 language. Given the size and complexity of the code, it would be a fruitless task to try to fully document the entire VI’s *modus operandi*. The following, therefore, will simply list the tasks it performs during the steps of optimization and data acquisition. The VI is separated into ‘Setup’ and ‘Scan’ modes, which have the following functionality.

Setup mode:

- Display of WLC spectrum and RMS values (to facilitate optimization)
- Display of ΔOD (display of current signal to facilitate overlap optimization)

- Manual control of delay stage, including setting position corresponding to $t = 0$
- Chopper reference beam intensity level (set value to allow code to assess if 500 Hz chopper reference is ‘pump-on’ or ‘pump-off’ for odd shots)
- Manual control of shutters

Scan Mode:

- Start/stop/pause/save scan options
- Save directory and file name
- No. of scans
- Select delays file or generate them from specified parameters (see below)
- Display of transients for selected wavelengths
- Display of spectra, with ‘all’ or ‘select’ delays option
- ‘Current scan’ data or ‘averaged scans’ data option for transients and spectra
- WLC spectrum
- Current system status and scan progress

2.3.8.4. Data Acquisition

The first operation of a single ‘scan’ is to acquire a background intensity that may be used to correct for stray light, dark noise and pump-probe independent signal. This is done by blocking the probe beam using the shutter and recording the pump only scatter and background signals. These intensities may be subtracted from all subsequent shots during the scan.

The delay stage will then move between a series of specified pump-probe delays, from -1 ps to t_{max} (the maximum delay required), and a difference spectrum is recorded at each. The pump-probe delays, $t(i)$, are either loaded from a predefined .txt file or generated according to:

$$t(i) = \begin{cases} -1 + \frac{2i}{N} & \text{for } i = 0 \dots N - 1, \\ 10^{-1+\frac{i}{N}} & \text{for } i = N \dots [N(1 + \log t_{max})]. \end{cases} \quad (2.6)$$

where N denotes the number of pump-probe delays between -1 and 1 ps and t_{max} is the maximum pump-probe delay. This generates the same number of delay points in each order of magnitude of delay. This means that a fitting procedure will have equal weighting for dynamics of every timescale.¹²

Calculation of the difference spectra are performed in LabVIEW as the data is acquired from the spectrometer. For a single time delay, in a single scan, the data array received consists of an array of 2500 shots \times 813 pixel intensities. The 2500 shots are divided into two arrays of ‘pump-on’ and ‘pump-off’ shots, according to the chopper reference intensity. The pump-probe difference signal for each pixel at a given pump-probe delay is recorded as:

$$\Delta OD(t) = \log \frac{I_{Puff}(t) - I'_{bkg}}{I_{Pon}(t) - I''_{bkg}} \quad (2.7)$$

where I_{Puff} and I_{Pon} , are the intensities of WLC probe with pump-off and pump on, respectively; and I'_{bkg} and I''_{bkg} the pump-off and pump-on background intensities, respectively. A shortcoming of this method is due to the recording of the background at the beginning of each scan and not for every delay. To do so, however, would increase the acquisition time two-fold and, generally, insignificant variation in this background is seen anyway.

2.3.9. Optimisation and Accreditation

2.3.9.1. Instrument Response Function

The interaction of the pump and probe pulses in non-absorbing media, *i.e.* glass or solvent, when the pulses are matched temporally allows for the instantaneous absorption of a photon

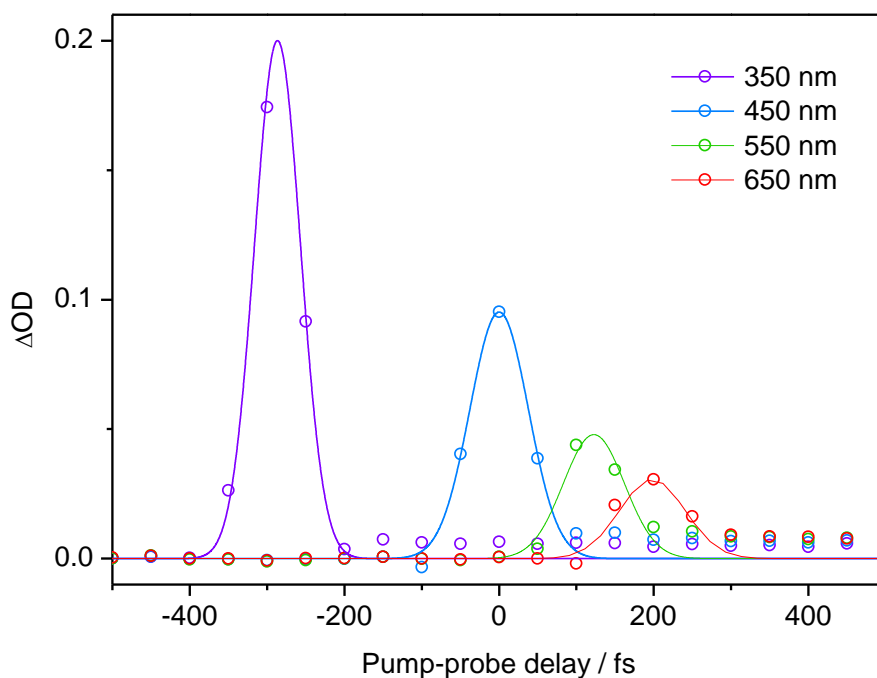


Figure 2.10 | IRFs of a film of methanol excited at 267 nm for four probe wavelengths.

from both pump and probe pulses (non-degenerate two-photon absorption). Variation of pump-probe delay around this point allows one to record the instrument response function (IRF) to find the temporal resolution. The pump and probe pulses are both temporally Gaussian, hence their interaction typically yields a Gaussian-like artefact. Figure 2.10 shows the IRF recorded in a liquid film of methanol, pumped with 267 nm and probed at four wavelengths across our probe region. These are each fit with Gaussian functions to give FWHM of between 70 and 100 fs.

2.3.9.2. Chirp Correction

Since the broadband white light is chirped (due to group velocity dispersion, GVD), time zero is wavelength dependant. For the scan shown in Figure 2.10 pump-probe delay is set to zero for 450 nm; other wavelengths would require correction of the timescale for ultrafast measurements. Hence, for each wavelength we are required to fit a Gaussian to the time zero artefact (as above) to accurately pinpoint time-zero for that wavelength. A new program can be

used to resolve this automatically to arrive at a GVD curve, which represents the difference in wavelength-dependent time zeros across the WLC (Figure 2.11) and is fitted using an exponential function. This curve can then be used to correct time zero for the acquired transient data.

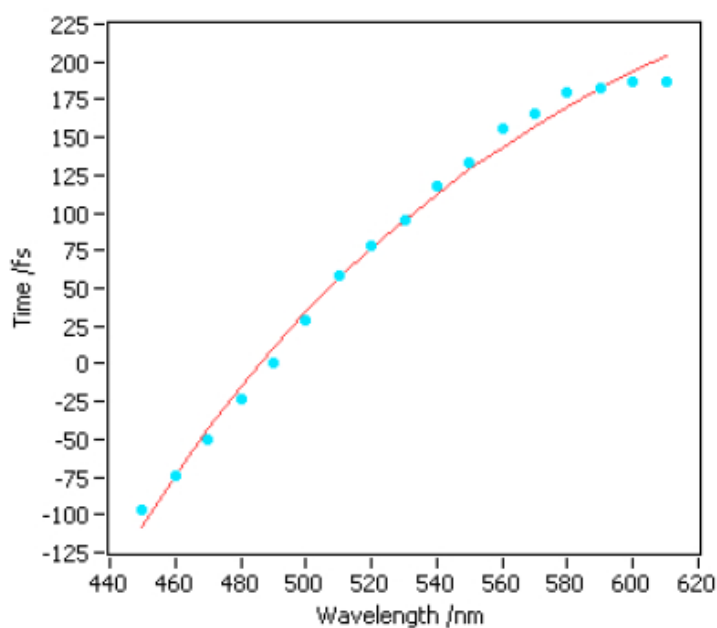


Figure 2.11 | Sample of GVD curve fitted from two photon artefact of pumping methanol at 266 nm.

2.3.9.3. DCM Reproduction

The laser dye *trans*-4-dicyanomethylene-2-methyl-6-*p*-dimethylaminostyryl-4H-pyran (DCM – Figure 2.12) has been extensively studied¹³⁻¹⁶ and used as a test for other systems due to its

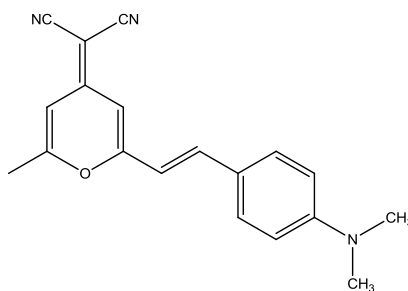


Figure 2.12 | DCM - *trans*-4-dicyanomethylene-2-methyl-6-*p*-dimethylaminostyryl-4H-pyran.

strong absorption and fluorescence properties, and high photostability. In polar solvents the excitation of DCM leads firstly to a short-lived locally excited singlet state (S_1 -LE) followed by intramolecular charge transfer to the charge transfer (CT) state, characterized by significantly lower electron density on the electron donating group than the acceptor group. The CT state is then known to radiatively decay to the ground state.

The relatively large transient gain signal that results is easily characterized for exemplar wavelengths. The most complete study to date (Maciejewski *et al.*)¹⁶ used a white light supercontinuum to probe excited state dynamics following excitation with 400 nm. Two distinct processes that dominate the observed transients are: stimulated fluorescence, S_1 -CT \rightarrow S_0 , (max. intensity *circa* 620 nm) and excited state absorption, $S_n \leftarrow S_1$ (max. intensity *circa* 450 nm). In the spectral range between 520 and 560 nm both process compete and the resulting transients are convoluted.

DCM has been used to calibrate the current setup during its inception. As an example, DCM in ethanol, delivered using a 1 mm path length flow cell, was excited with 400 nm light before

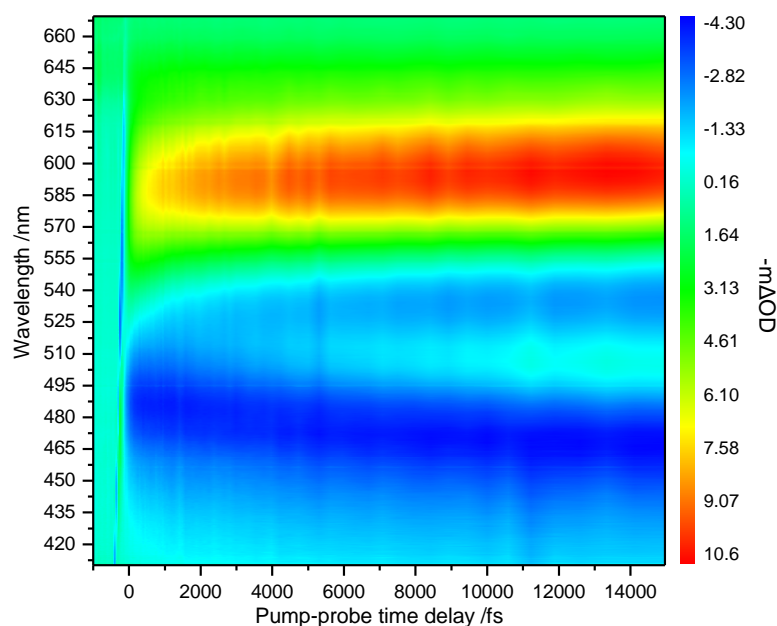


Figure 2.13 | Time and energy resolved transient absorption in DCM in ethanol following excitation with 400 nm.

Time zero not corrected.

probing the dynamics. A 2D intensity plot, Figure 2.13, shows the ΔOD as a function of pump-probe delay and wavelength. Transients for exemplar wavelengths (Figure 2.14) show very similar dynamics as those seen in by Maciejewski *et al.* in methanol at 400 nm excitation.

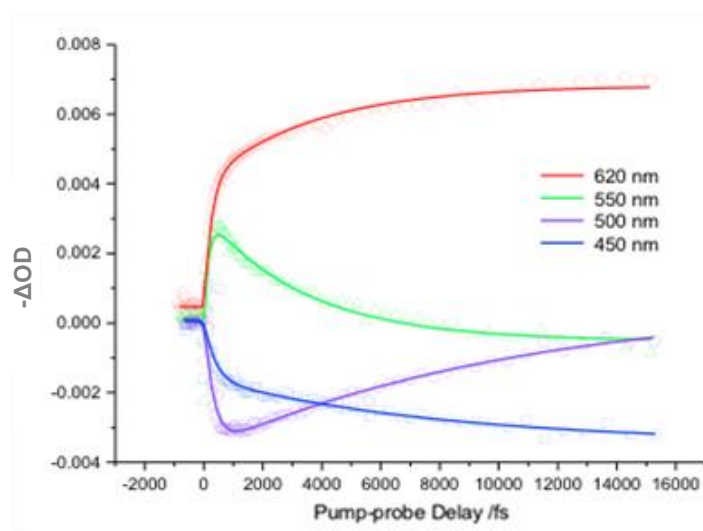


Figure 2.14 | Fitted transients for DCM in ethanol at 620, 550, 500 and 450 nm. *Nota bene* the ΔOD axis has its polarity inverted i.e. $-\Delta OD$ (not the typical $+\Delta OD$).

2.3.9.4. Phenol Reproduction

The replication of studies performed on phenol in solution by Zhang *et al.*¹⁷ were important, firstly to confirm that the liquid jet was operable, and secondly to ensure we were able to observe photoproduct absorption signals of radical species that are convoluted with ESA. Figure 2.15 shows the transient absorption spectrum of a 10 mM solution of phenol in cyclohexane 2

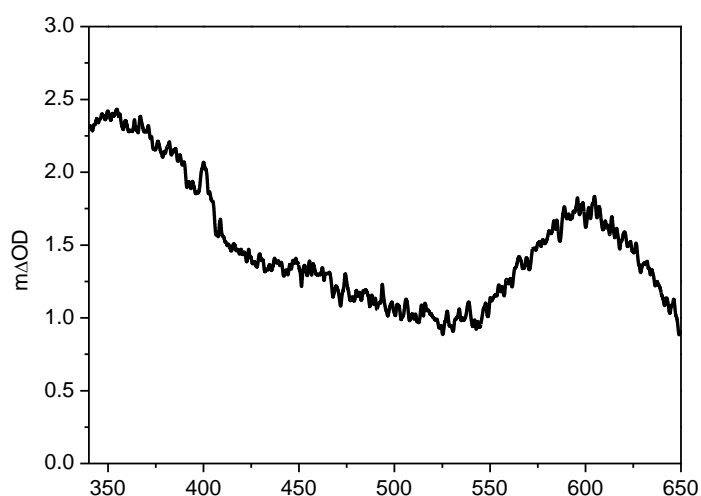


Figure 2.15 | TAS of phenol in cyclohexane at 2 ns after excitation with 267 nm.

ns after excitation with 267 nm. The overall shape and features agree strongly with that seen in the aforementioned work. The phenoxyl radical signature, viewed as a sharp strong peak at 400 nm and a weaker slightly broader peak at ~380 nm are distinguishable.

2.4. Bibliography

- (1) Moulton, P. F. *J. Opt. Soc. Am. B* **1986**, 3, 125.
- (2) Diels, J.-C.; Rudolph, W. In *Ultrashort Laser Pulse Phenomena (Second Edition)*; Diels, J.-C., Rudolph, W., Eds.; Academic Press: Burlington, 2006, p 143.
- (3) Boyd, R. W. In *Nonlinear Optics (Third Edition)*; Boyd, R. W., Ed.; Academic Press: Burlington, 2008, p 1.
- (4) Eckardt, R.; Reintjes, J. *IEEE J. Quantum Electron.* **1984**, 20, 1178.
- (5) Brabec, T.; Krausz, F. *Phys. Rev. Lett.* **1997**, 78, 3282.
- (6) Gaeta, A. L. *Phys. Rev. Lett.* **2000**, 84, 3582.
- (7) Aleksei, M. Z. *Physics-Uspekhi* **2006**, 49, 605.
- (8) Johnson, P. J.; Prokhorenko, V. I.; Miller, R. *Opt. Express* **2009**, 17, 21488.
- (9) Lakowicz, J. R. In *Principles of Fluorescence Spectroscopy*; Lakowicz, J. R., Ed.; Springer US: 2006, p 353.
- (10) Maguire, L. P.; Szilagyi, S.; Scholten, R. E. *Rev. Sci. Instrum.* **2004**, 75, 3077.
- (11) Tauber, M. J.; Mathies, R. A.; Chen, X.; Bradforth, S. E. *Rev. Sci. Instrum.* **2003**, 74, 4958.
- (12) Megerle, U.; Pugliesi, I.; Schrieffer, C.; Sailer, C. F.; Riedle, E. *Appl. Phys. B: Lasers Opt* **2009**, 96, 215.
- (13) Pommeret, S.; Gustavsson, T.; Naskrecki, R.; Baldacchino, G.; Mialocq, J.-C. *J. Mol. Liq.* **1995**, 64, 101.
- (14) Martin, M. M.; Plaza, P.; Meyer, Y. H. *Chem. Phys.* **1995**, 192, 367.
- (15) Kovalenko, S. A.; Ernsting, N. P.; Ruthmann, J. *Chem. Phys. Lett.* **1996**, 258, 445.
- (16) Maciejewski, A.; Naskrecki, R.; Lorenc, M.; Ziolek, M.; Karolczak, J.; Kubicki, J.; Matysiak, M.; Szymanski, M. *J. Mol. Struct.* **2000**, 555, 1.
- (17) Zhang, Y.; Oliver, T. A. A.; Ashfold, M. N. R.; Bradforth, S. E. *Faraday Discuss.* **2012**, 157, 141.

This chapter is based on the following publication:

Greenough, S. E.; Horbury, M. D.; Thompson, J. O. F.; Roberts, G. M.; Karsili, T. N. V.; Marchetti, B.; Townsend, D.; Stavros, V. G.; *Phys. Chem. Chem. Phys.*, **16**, **2014**, 16187.

*TR-PEI measurements discussed in Section 3.4 were performed
by J. O. F. Thompson and D. Townsend*

Theory calculations discussed in Section 3.5 were performed by

T. N. V. Karsili and B. Marchetti



3.1. Introduction

Conformationally controlled reactions are an intrinsic part of chemistry, be it stereoselective synthesis or protein-folding functionality. Molecular conformers, which may interconvert *via* rotations about single bonds, have low-energy barriers that are easily overcome following photoexcitation. This presents difficulties if one wishes to track the dynamics of a single, conformer specific photochemical reaction; the signal is an ensemble average from the various conformers present. Notable examples, where such specificity was achieved, have been in gas-phase experiments and include conformer driven photodissociation of iodopropane ions;¹ propanal cations,^{2,3} morpholine⁵ and 3-pyrroline.⁶

Whilst such gas-phase experiments have provided exquisite insight into conformation-specific photochemistry and offer tremendous scope through sequentially increasing molecular complexity to mimic more biologically relevant systems,^{7,8} they neglect interactions with surrounding solvent and solute molecules, which are critical to the functionality of many biological systems.^{9,10} In this work, we seek to apply this knowledge base to address the role of conformationally driven photodissociation in solution. Conformer specific photochemistry in solution is very well documented in the literature, as exemplified beautifully through excited state intra- and intermolecular proton transfer studies;⁹⁻¹² however, examples concerning conformationally driven photodissociation are sparse and here we demonstrate such findings for guaiacol (2-methoxyphenol).

Guaiacol is a UV chromophore of lignin, the superabundant natural polymer important to the structural rigidity of vegetal tissues. The properties of lignin (and its subunits) have been studied extensively¹³⁻¹⁹ due, in part, to its biological importance²⁰ and also its industrial potential, such as for use in biofuel production.²¹ The addition of a methoxy group at phenol's *ortho* position fosters multiple conformers of guaiacol. The structures of the two lowest energy conformers in the gas-phase, termed **A** and **B**, are shown in Figure 3.1. In the gas-phase, conformer **A** is the lowest in energy, owing to the intramolecular hydrogen bond between the phenolic hydrogen

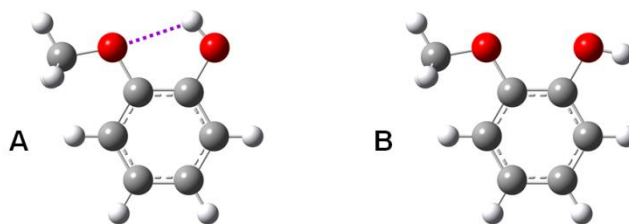


Figure 3.1 | The structures of the two lowest energy conformers, **A** and **B**, of guaiacol.

and methoxy oxygen. *Ab initio* (gas-phase) calculations¹⁵ have found the interconversion barrier between **A** and **B**, to range between 2291 and 2532 cm^{-1} . These calculations also determined the energy difference between the two conformers to fall between 1569 and 1670 cm^{-1} . Given these energies, one may expect the population of **A** to be >99% at room temperature in the gas-phase. In a weakly perturbing environment, such as that of a non-polar solvent (*e.g.* cyclohexane), we would anticipate similar Boltzmann statistics, with conformer **A** dominating. However, in a highly perturbing environment such as that of a hydrogen bonding solvent (*e.g.* methanol or H_2O), we would anticipate significant population of conformer **B** as intermolecular hydrogen bonding stabilises conformer **B**, thus lowering its energy.²²

In this chapter we present our findings of guaiacol's conformation specific photochemistry in solution using transient absorption (TA) spectroscopy following initial excitation to the S_1 ($^1\pi\pi^*$) state with 267 nm radiation. A key finding in our results is that we are able to demonstrate conformational control in the ensuing photodissociation dynamics through choice of solvent, enabling us to effectively switch on O–H bond fission in guaiacol in a polar, H-bonding solvent and switch this process off in a non-polar solvent. In order to explore this conformational control further, we compare our results with highly complementary gas-phase time-resolved photoelectron imaging (TRPEI) measurements and high level complete active space with its second order perturbation theory (CASPT2) calculations, which show that our results in a non-polar solution map on to those observed *in vacuo*, as one may anticipate from a weakly perturbing environment.

3.2. Methods

TA spectroscopy, employing 267 nm (4.64 eV) pump pulses with fluences in the region of $2 \leq F \leq 6 \text{ mJ cm}^{-2}$ and broadband white-light (340 to 690 nm) probe pulses, was used to record TAS of guaiacol (98%, Sigma-Aldrich) in 25 mM solutions of either cyclohexane (99.7%, VWR) or methanol (99.9%, Sigma-Aldrich) flowing through a wire-guided gravity jet (as described in Chapter 2), at a range of pump-probe time delays. The time-window of our experiments is set at 2 ns, although we have recorded transient absorption spectra (TAS) at longer pump-probe time delays (up to 10 ns) merely serving to confirm any qualitative evolution of key spectral features in our TAS after 2 ns. The chosen concentration ensures a sample absorbance of around 0.5 with a $\sim 125 \mu\text{m}$ path length.

TRPEI measurements of guaiacol (98%, Sigma-Aldrich), following excitation at 267 nm (4.64 eV) and probing at 305 nm (4.06 eV), were recorded at pump-probe time delays of -500 fs to +100 ps. The TRPEI setup has been described in detail elsewhere⁴ and is recapped in Appendix B.

Unrelaxed (rigid body) potential energy scans were computed along the O–H bond extension coordinate ($R_{\text{O-H}}$) using the CASPT2 method. The theoretical calculation methods are documented in Appendix B.

3.3. Results and Discussion

3.3.1. Transient Absorption Spectroscopy

TAS of guaiacol/cyclohexane following excitation with 267 nm light at a series of pump-probe time-delays are shown in Figure 3.2a and b, for early ($< 25 \text{ ps}$) and long ($25 \text{ ps} - 8 \text{ ns}$) delays, respectively. The profile of the TAS is broadband, with two distinctive broad peaks (~ 340 and $\sim 620 \text{ nm}$) and resembles that seen in analogous studies of phenol in cyclohexane.²³ Based on this, we similarly assign this broad transient absorption signal to excited state absorption (ESA) from the S_1 state to higher lying singlet states (S_n) – a conclusion made in other similar

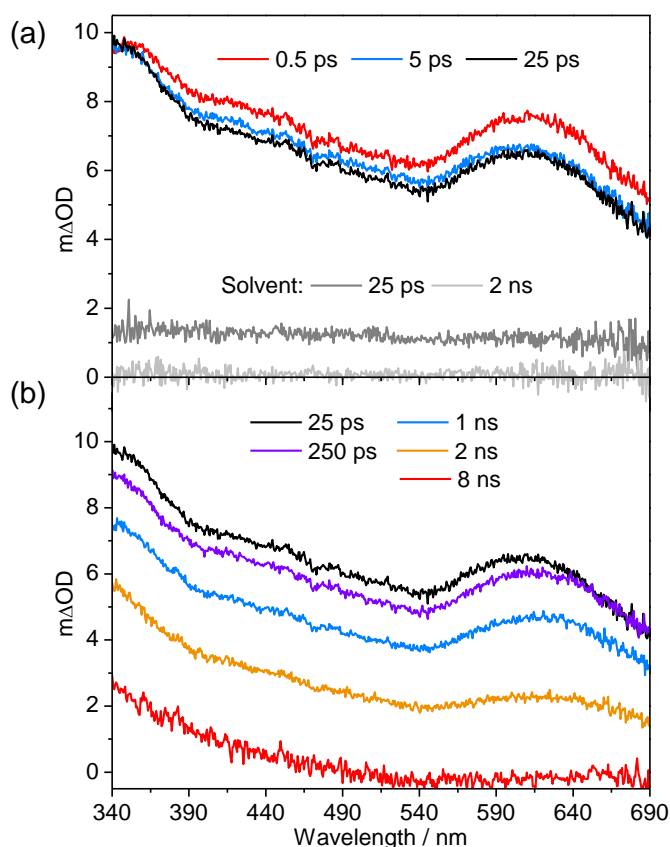


Figure 3.2 | TAS of 25 mM guaiacol/cyclohexane solution at times: (a) <25 ps and (b) 25 ps to 8 ns. Solvent-alone scans at 25 ps (dark grey) and 2 ns (light grey).

studies.^{24,25} Cursory inspection shows that as the pump-probe delay increases from 0.5 ps to 2 ns, the TAS decay almost uniformly across the entire spectral window of the probe. We have also included representative TAS for solvent-alone scans at 25 ps and 2 ns, shown in Figure 3.2a, which has a flat absorption profile across 340 – 690 nm and also decays uniformly with increasing pump-probe delay. At the longest time-delay of 8 ns, transient absorption signal in the red end of our probe window ($\lambda > 500$ nm) recovers to a base line level of $\Delta OD = 0$, in accordance with complete decay of the S₁ ESA as the S₁ state is depopulated. However, at $\lambda < 500$ nm a broad transient absorption signal, which gradually rises towards the blue end of the spectrum, is seen to persist. Given that the profile is significantly different to the S₁ ESA, this must be due to a different absorbing species or state.

It is known that ISC in photoexcited phenol(s) is non-zero in a range of solvents.²⁶ The ISC quantum yield (ϕ_T) in phenol has been shown to be dependent on solvent polarity, with ϕ_T values for phenol in cyclohexane, acetonitrile and ethanol of 0.27, 0.50 and 0.67, respectively.²⁶ Differential TAS on phenol, with and without triplet quenching, has also shown the ESA profile of the populated triplet state (T_n) to be weakly absorbing, broad and structureless in the range 350 – 475 nm.²⁷ However, a number of substituted phenols and related species (*viz.* *p*-cresol and anisole) have remarkably different T_n ESA in this spectral region and display a more sloping character, each rising below ~500 nm with a maximum at ~375 nm, akin to what we observe in Figure 3.2b at 8 ns.²⁷ With some confidence therefore, we assign this feature to T_n ESA, suggesting that ϕ_T for $S_1 \rightarrow T_n$ in guaiacol/cyclohexane is non-zero.

We have repeated these TA measurements with methanol as the solvent, and the obtained TAS are shown in Figure 3.3a and b. The profiles of the TAS are broadband and generally possess the same characteristics as the S_1 ESA seen in cyclohexane. However, the TAS recorded for guaiacol in methanol between 0.5 – 25 ps (Figure 3.3a) differ from those recorded in cyclohexane (Figure 3.2a) in that there is a noticeable increase in the relative size of the absorption profile in the red end of the probe spectrum versus that of the blue. This is reconciled by looking at the solvent-only scan for methanol at 25 ps in Figure 3.3a (dark grey line), which has a clear bias toward the red end of the probe spectrum, and is itself time-dependent, as demonstrated by the solvent-only scan for methanol at 2 ns in the same figure (light grey line).

Spectra at later time delays (25 ps to 2 ns) are shown in Figure 3.3b and also show a similar trend to those obtained for guaiacol in cyclohexane. The S_1 ESA profile decays over time, and once again, at the longest time delay of 10 ns, a similar T_n ESA signature is observed, although this appears to be larger and spans a greater region of our probe window in methanol. Given the increasing ϕ_T trend observed in phenol as a function of increasing solvent polarity (*vide supra*), this may explain the relative difference in size of the T_n ESA signal seen in guaiacol/cyclohexane *versus* guaiacol/methanol solutions at >8 ns.

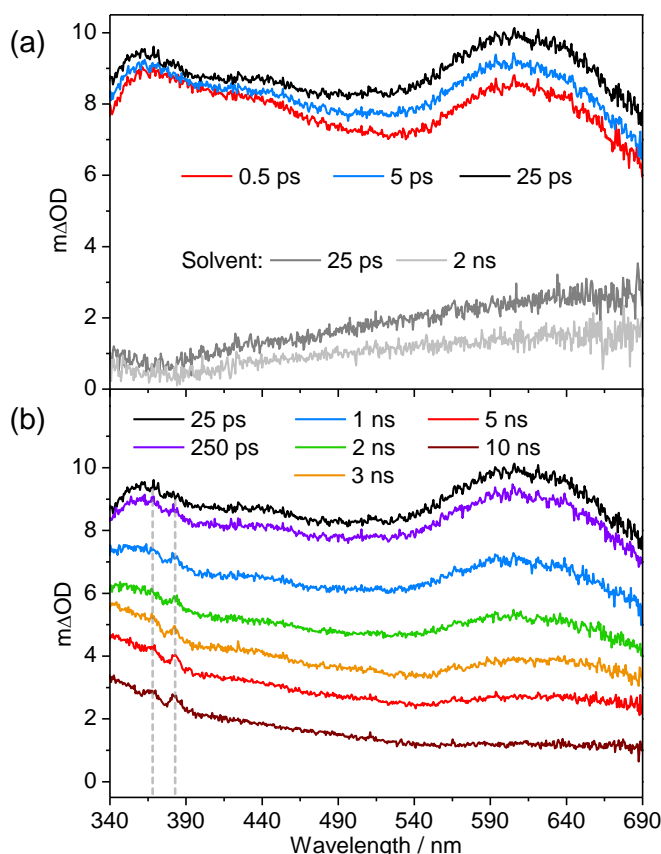


Figure 3.3 | TAS of 25 mM guaiacol/methanol solution at times: (a) <25 ps and (b) 25 ps to 10 ns. Solvent-alone scans at 25 ps (dark grey) and 2 ns (light grey).

Whilst the guaiacol/methanol and guaiacol/cyclohexane TAS are largely similar, notable differences are present. In particular, one can clearly discern a new spectral feature emerging from ~250 ps onwards, with two peaks centred at 368 and 383 nm, in the guaiacol/methanol TAS, which are absent within the signal-to-noise of the guaiacol/cyclohexane measurements, as highlighted with grey dashed lines in Figure 3.3b. Nanosecond TA studies of guaiacol/*tert*-butoxy radical mixtures in acetonitrile reveal that the guaiacoxyl radical [$\text{C}_6\text{H}_4(\text{OCH}_3)(\text{O})$] has a vibrationally structured absorption feature around 380 nm (with peaks at ~365 and ~381 nm) and a broad absorption at around 650 nm.¹³ These are due, respectively, to the $\text{C} \leftarrow \text{X}$ and $\text{B} \leftarrow \text{X}$ electronic transitions in $\text{C}_6\text{H}_4(\text{OCH}_3)(\text{O})$. Whilst the broad absorption band at 650 nm appears to be absent in our TAS, the vibrationally structured features observed at 368 and 383 nm in Figure 3.3b give us confidence that these are due to the formation of guaiacoxyl radicals. Potential reasons for the absence of a clear guaiacoxyl radical absorption signature at ~650 nm

may be due to the fact that the T_n ESA and remaining solvent response are significantly masking this feature. This is supported by the TAS collected at 2 ns in a 35 mM guaiacol/chloroform solution (Figure 3.4) which clearly returns the guaiacoxyl radical absorption spectrum, including the weaker broad absorption feature at 650 nm due to the $B \leftarrow X$ transition.¹³ The excited state quenching properties of chloroform²⁸ are well established and serve to highlight that a combination of solvent signal and T_n ESA is indeed most likely masking the appearance of the weaker broad absorption feature at ~650 nm.

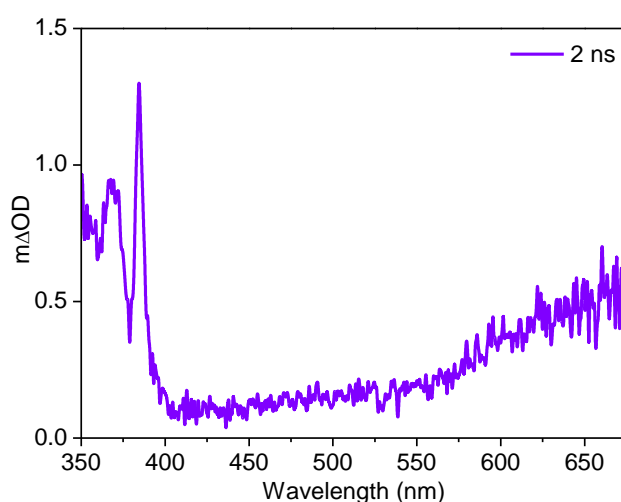


Figure 3.4 | TAS of 35 mM solution of guaiacol in chloroform recorded using a 100 μ m path length Harrick flow-cell at 2 ns after 267 nm irradiation. Quenching of excited state through an electron transfer to solution process yields the absorption spectrum of the guaiacoxyl radical, in good accord with previous studies.¹³

3.3.2. Kinetic Fitting Procedure

Our TAS of guaiacol in cyclohexane and methanol also allows us to extract an S_1 lifetime. Given that the guaiacoxyl radical absorbs at ~380 nm and ~650 nm, and the T_n ESA signal is present at <500 nm, integrating a 5 nm wide slice of the TAS centred at 540 nm (where S_1 ESA dominates) across pump-probe time-delays from 25 ps to 2 ns enables us to probe the S_1 state lifetime with minimal spectral overlap of any possible radical features or T_n ESA; this is shown in Figure 3.5. A stepwise fitting procedure for transients in Figure 3.5 is now described.

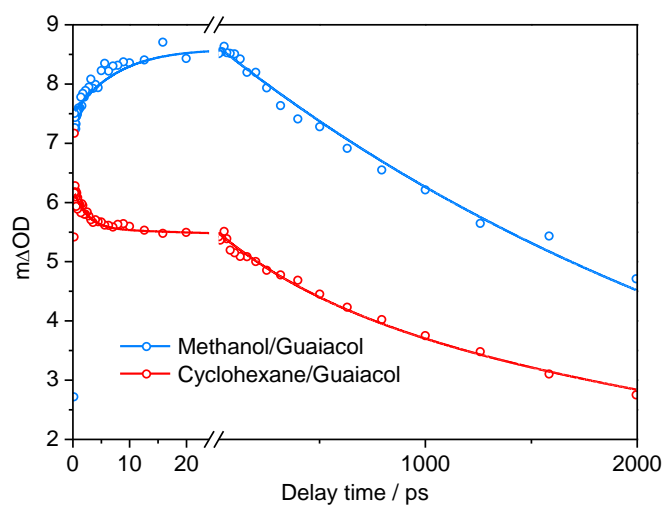


Figure 3.5 | Kinetic traces for guaiacol/cyclohexane and guaiacol/methanol solutions from 0 to 2 ns, each fitted with a multi-exponential decay.

3.3.2.1. Solvent Transients

The same method used to obtain transients from TAS cyclohexane/guaiacol and methanol/guaiacol solutions, *i.e.* 5 nm slices of the spectra shown in Figure 3.2 and Figure 3.3, is used to obtain 0 to 2 ns, 540 nm kinetic traces from *solvent only* TAS. These are each fit with biexponential functions of the type:

$$f(t) = A_i e^{-t/\tau_i} + A_{ii} e^{-t/\tau_{ii}} \quad (3.1)$$

where A are amplitudes, τ are the associated time constants and t is the pump-probe delay. These kinetic traces and their fits are shown in Figure 3.6. The extracted time constants for the cyclohexane are $\tau_i = 2.2 \pm 0.3$ ps and $\tau_{ii} = 570 \pm 51$ ps; and for methanol are $\tau_i = 8.3 \pm 0.9$ ps and $\tau_{ii} = 3.5 \pm 0.4$ ns. The faster component of the methanol response has negative amplitude and is thus a rise in signal; all others are decays. The slow decay of the methanol signal means that it does not reach zero by the end of the 2 ns probe window whereas cyclohexane recovers fully.

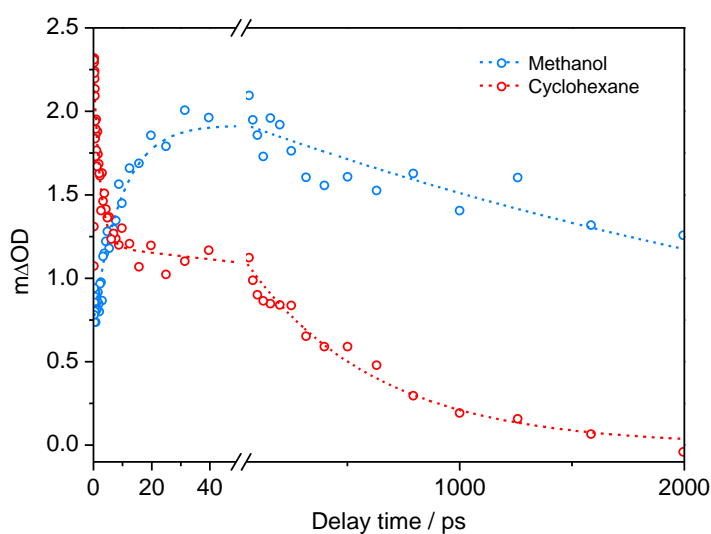


Figure 3.6 | Kinetic traces of the solvent response of methanol (blue) and cyclohexane (red), following excitation at 267 nm from 0 to 2 ns, each fit with biexponential decay functions

3.3.2.2. Multicomponent Solute/Solvent Fits

As there is a significant contribution from the solvent we use values obtained from the solvent response fits to account for these solvent contributions in the fitting of cyclohexane/guaiacol and methanol/guaiacol kinetic traces shown in Figure 3.5. These traces are fit with multi-exponential functions of the type:

$$f(t) = A_i e^{-t/\tau_i} + A_{ii} e^{-t/\tau_{ii}} + A_1 e^{-t/\tau_1} + A_2 e^{-t/\tau_2} \quad (3.2)$$

The first two terms are solvent parameters and the second two terms are solute parameters. During the fitting of guaiacol/cyclohexane and guaiacol/methanol kinetic traces, the solvent parameters are locked (constant) to the values obtained from solvent response fits above. Table 3.1 shows the values of each parameter for the fits.

Table 3.1 | Collated parameters from fitting of solvent-alone and guaiacol solution data

	Parameter	Cyclohexane		Methanol	
		Value	Error [†]	Value	Error [†]
Solvent	A_i	1.2 (mOD)	0	−1.2 (mOD)	0
	τ_i	2.2 ps	0	8.3 ps	0
	A_{it}	1.2 (mOD)	0	2 (mOD)	0
	τ_{it}	570 ps	0	3.5 ns	0
Guaiacol	A_1	−0.5 (mOD)	0.04 (mOD)	−0.6 (mOD)	0.03 (mOD)
	τ_1	2.1 ps	0.4 ps	540 fs	250 fs
	A_2	4.3 (mOD)	0.01 (mOD)	6.7 (mOD)	0.02 (mOD)
	τ_2	4.5 ns	0.16 ns	2.9 ns	0.07 ns

[†]Standard error. Locked parameters return zero error.

The fit of guaiacol/cyclohexane and guaiacol/methanol kinetic traces shown in Figure 3.5 can thus be thought of as the sum of two biexponential functions: a solvent component and a solute component. An alternative version of this figure is shown as Figure 3.7 and Figure 3.8 where the components of the fit are presented separately.

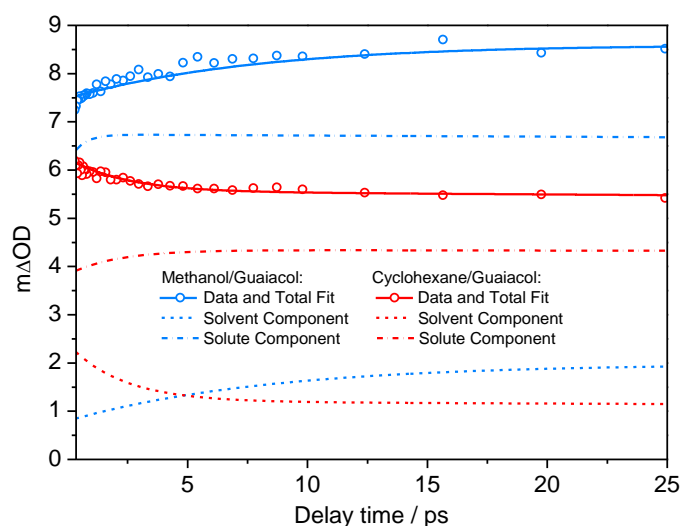


Figure 3.7 | Kinetic traces of the methanol/guaiacol (blue) and cyclohexane/guaiacol (red), following excitation at 267 nm from 0 to 25 ps, each fit with tetraexponential decay functions (solid line). Dotted lines show the solvent component (the same as the fits in Figure 3.6). Dashed-dotted lines show the solute (guaiacol) component.

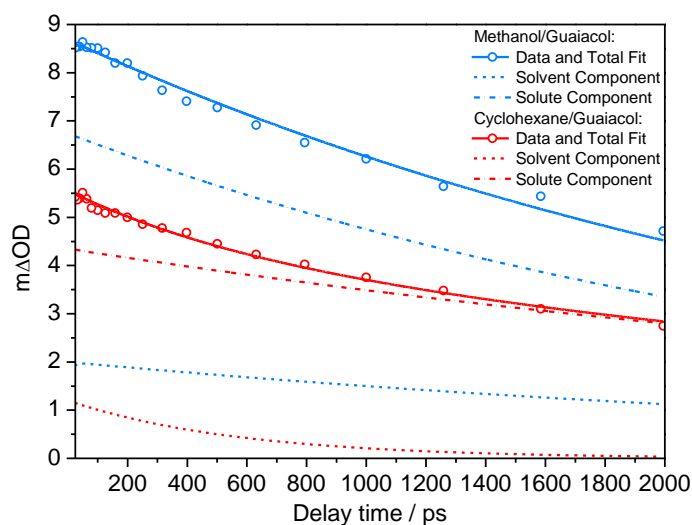


Figure 3.8 | Kinetic traces of the methanol/guaiacol (blue) and cyclohexane/guaiacol (red), following excitation at 267 nm from 25 to 2 ns, each fit with tetraexponential decay functions (solid line). Dotted lines show the solvent component (the same as the fits in Figure 3.6). Dashed-dotted lines show the solute (guaiacol) component.

The results of these fits return S_1 lifetimes of 4.5 ± 0.2 ns and 2.9 ± 0.1 ns for guaiacol in cyclohexane and methanol, respectively. The early dynamics (<25 ps) are a convolution of dynamics of the solvent alone in addition to both intramolecular vibrational relaxation (IVR) in guaiacol and intermolecular energy transfer (IET) between guaiacol and the solvent bath, collectively termed vibrational energy transfer (VET).^{24,29,30} The kinetic fits also yield timescales for VET of 2.1 ± 0.4 ps and 540 ± 250 fs for guaiacol in cyclohexane and methanol, respectively. In each case this manifests as a small increase in S_1 ESA as the Franck-Condon overlap for $S_n \leftarrow S_1$ absorption evolves through VET on S_1 (presumably giving better overlap between S_1 and the S_n states). The faster VET time constant of guaiacol/methanol, relative to guaiacol/cyclohexane, can be rationalised on the basis that the former is an intermolecularly hydrogen bonded system and IET will be significantly increased.³⁸ Whilst these dynamical processes are interesting in themselves, they do not contribute to the main thrust of this work and hence are not discussed further in this chapter.

3.4. Time-Resolved Photoelectron Imaging

To gain further insight into the mode(s) of decay of the initially excited S_1 state in guaiacol, we have also carried out highly complementary TRPEI measurements following excitation at 267 nm and probing at 305 nm. Figure 3.9 depicts: (a) the time-dependent photoelectron spectrum, (b) the results of a global fitting analysis to this spectrum using two exponential basis functions; and (c) the associated residuals, in which the fit is subtracted from the raw data. The energy axis is plotted in electron binding energy (eBE), given the known adiabatic ionisation potential of guaiacol ($IP_{ad} = 7.93 \text{ eV}^{31}$). As is evident from Figure 3.9a and b, there is very little decay in photoelectron signal intensity across all eBEs within the sampled pump-probe delays (-500 fs to $+100 \text{ ps}$), suggestive of very long-lived dynamics in the initially excited S_1 state.

Further information of the excited state dynamics from the TRPEI data can be gleaned through the decay-associated spectrum (DAS) shown in Figure 3.10a. The DAS yields two time components, 3.2 ps and 1.3 ns. The short time component of 3.2 ps, which is positive at low eBE and negative at high eBE (indicative of a flow of vibrational population at early times), is assigned to rapid IVR within S_1 , mediated by vibrational ‘doorway states’, in accordance with

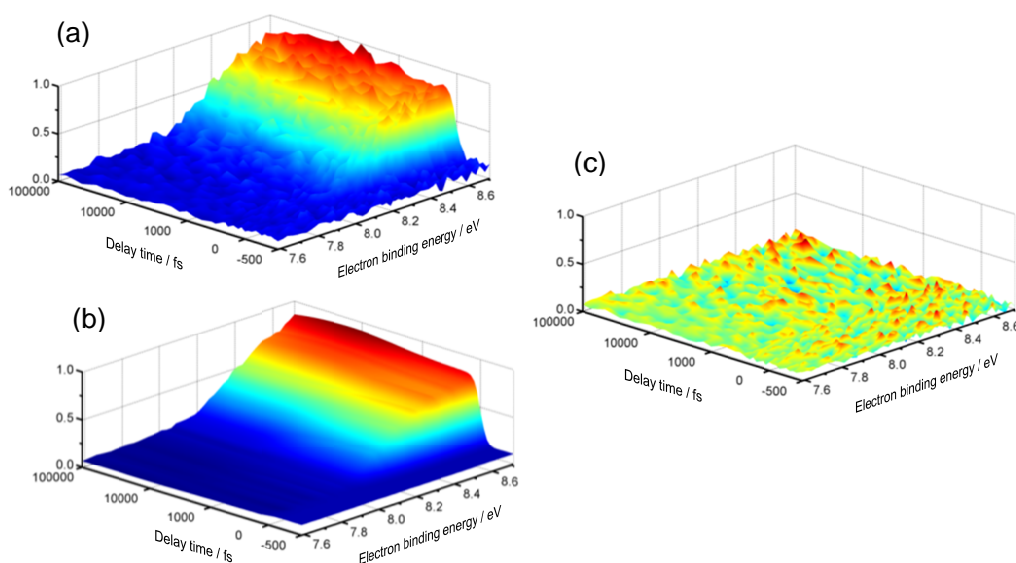


Figure 3.9 | (a) Time-dependent photoelectron spectrum (b) its fit and (c) the associated residuals. Time axes are linear between $\pm 500 \text{ fs}$ and then logarithmic to $+100 \text{ ps}$.

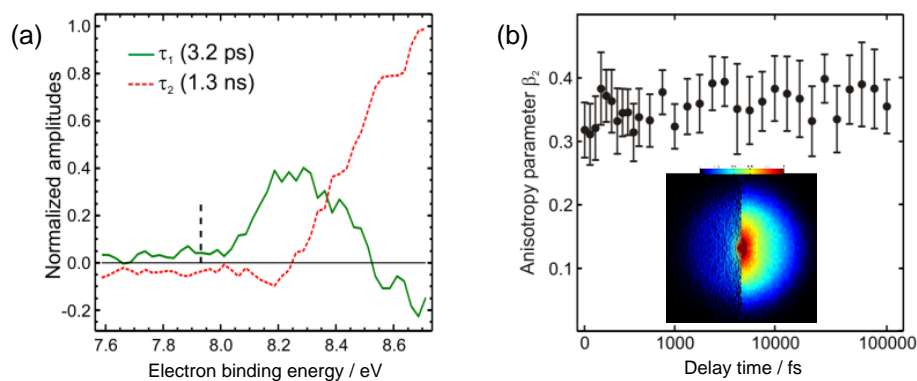


Figure 3.10 | (a) DAS of the TRPEI data (vertical dashed line denotes the ionisation potential), (b) anisotropy parameter β_2 as a function of pump-probe delay, where error bars represent one standard deviation, and (b) (inset) right half: background-subtracted photoelectron image at a pump-probe time delay of 100 ps and left half: same image after Abel inversion performed using methods outlined in ref. 4. Time axis is linear to 500 fs and then logarithmic to +100 ps.

work on several related systems.^{4,8} We note that this IVR time constant is of the same order as the 2.1 ps VET time constant obtained from the kinetic analysis of guaiacol/cyclohexane TAS, although the latter is faster given that IET is also active in solution. In this instance, the IVR process results in a slight increase in ionisation signal at early delay times beyond zero – see Figure 3.9a and b – due to improved Franck-Condon overlap between S_1 and the final guaiacol⁺ cation state. A similar effect has previously been seen in resorcinol (1,3-dihydroxybenzene).⁴ The long-time component of 1.3 ns represents a *lower limit* for the S_1 state lifetime of isolated guaiacol (given the limited temporal window of 100 ps for the TRPEI measurements), and broadly agrees with the nanosecond lifetimes extracted for guaiacol in solution from the TA measurements and the previously reported gas-phase S_1 lifetime of ~ 7 ns.³² However, the decay mechanisms contributing to this lifetime are more difficult to extract from the DAS alone. TA measurements in the weakly interacting cyclohexane solvent might suggest that, in part, $S_1 \rightarrow T_n$ ISC crossing may also contribute in the gas phase. In principle, ionisation of any populated T_n states should be observable using TRPEI, although our measurements here do not extend to sufficient time-delays to indicate whether significant population becomes trapped in T_n at longer timeframes (*viz.* ~ 8 ns in TA).

Additional insight into the modes of decay from S_1 can also be gained by plotting the photoelectron anisotropy parameter, β_2 , as a function of pump-probe delay, as shown by Figure 3.10b. In earlier TRPEI studies on phenol (and related derivatives), clear temporal evolution of β_2 within the first 100 ps was observed, and was taken as a key reporter of vibronic coupling between the initially excited S_1 state and a nearby S_2 ($^1\pi\sigma^*$) state, leading to $S_1 \rightarrow S_2$ internal conversion (IC).⁴ Here though, the invariance in β_2 across all pump-probe delays (and all eBEs), suggests that following initial population of S_1 , there is no similar mixing of the S_1 and S_2 states within 100 ps, implying that (i) $S_1 \rightarrow S_2$ IC is unlikely to be an active decay pathway (as concluded in similar studies³³) and (ii) other pathways such as fluorescence, IC back to S_0 , and ISC to T_n are the favoured deactivation mechanisms of the S_1 state in guaiacol. We return to discuss this in subsequent sections.

3.5. Conformer Specific Photodissociation Dynamics

We now compare our findings from gas- and solution-phase measurements and begin with a comparison of the TRPEI data and the TA measurements in cyclohexane, where conformer **A** is expected to dominate any observed dynamics in both regimes (*vide supra*). Both sets of data clearly show that following excitation to the S_1 state, population flow out of S_1 occurs on a timescale >1.3 ns. The concordance of our gas- and solution-phase measurements is not surprising given that the non-polar, weakly perturbing environment of cyclohexane serves as an adequate model for the gas-phase environment.^{23,24,34} Most notably though, the results of the guaiacol/cyclohexane TAS do not show any clear signature for the formation of guaiacoxyl radicals. This latter observation is particularly critical; previous gas-phase studies on the related species phenol and catechol (1,2-dihydroxybenzene) at 267 nm have shown that the S_1 ($^1\pi\pi^*$) state decays through coupling onto the S_2 ($^1\pi\sigma^*$) state, which is dissociative along an O–H bond, leading to the production of H-atoms in coincidence with a radical co-fragment.^{4,32,35-37} This process occurs through a tunnelling mechanism under a conical intersection (CI)^{38,39} formed between the S_1 and S_2 states. The absence of any guaiacoxyl radicals in our TAS in

cyclohexane therefore suggests that, on the timescale of our measurements (extended to 8 ns), no photo-induced O–H bond fission *via* the S_2 state occurs in conformer **A**. This conclusion is also broadly supported by our TRPEI measurements. One would anticipate an increase in β_2 over time (as observed in phenol and catechol⁴) if non-adiabatic coupling between S_1 and S_2 were occurring in conformer **A** of guaiacol, given the 3s Rydberg character of the S_2 state in the Franck-Condon region (see Ref. 4 for a more expanded discussion); this is clearly absent in Figure 3.10b, in-line with previous studies on aniline where tunnelling mediated $S_1 \rightarrow S_2$ IC is shut off.³³

Whilst conformer **A** is almost exclusive in the gas-phase, and the weakly interacting ‘gas-phase like’ cyclohexane solution, methanol is a polar, hydrogen-bonding species that is expected to play a significant role in dictating the relative energies of the excited states and solute-solvent hydrogen bonding. Previous semi-empirical calculations of guaiacol in a series of solvents suggest that the conformer distribution moves from **A** to **B** with increasing dielectric constant.⁴⁰ From a theoretical standpoint, when one considers that conformer **B** may form an H-bond that approaches optimal angle and experiences a larger dipole moment, as well as, the possibility of bifurcated H-bonds, **B** is likely to experience a stronger H-bond to a solvent molecule than that of the intramolecular H-bond in **A**. Indeed, FTIR studies of catechol in inert solutions show a complete disappearance of the band of free O–H in the presence of high concentrations of a proton acceptor, with the same trend shown in guaiacol (spectra of guaiacol with high concentrations of proton acceptors were not presented in this work, but it seemingly behaves similarly to catechol in this regard).²² As a result, whilst we cannot rule out a mixture of both conformers **A** and **B**, there is strong evidence that conformer **B** dominates in guaiacol/methanol solution. Considering this, it is perhaps surprising that a comparison of our TAS collated in methanol, with the TAS in cyclohexane and the gas-phase TRPEI results, yields very good agreement for the S_1 state lifetime across these three different environments. In methanol however, there is clear evidence for the formation of guaiacoxyl radical photoproducts

(appearing as peaks at 368 and 383 nm), suggesting that an additional process is active in conformer **B**, which is absent in conformer **A** – namely photo-induced O–H bond fission into $\text{C}_6\text{H}_4(\text{OCH}_3)(\text{O}) + \text{H}$ photoproducts. In an attempt to better understand these experimental observations of solvent-induced conformer specific photochemistry in guaiacol, we turn to the results of complementary theoretical calculations. These calculations are presented in Figure 3.11a and show potential energy cuts (PECs) for the electronic ground state (S_0), S_1 ($^1\pi\pi^*$) and S_2 ($^1\pi\sigma^*$) electronic states of (gas-phase) guaiacol, with respect to elongation along the O–H bond ($R_{\text{O-H}}$) in both conformers **A** (red) and **B** (blue), at the CASPT2(12,11)/aug-cc-pVTZ level of theory. Before proceeding further, we first acknowledge that, while these gas-phase calculations inherently lack any account of solvation effects,³⁹ recent solution phase work on phenol and thiophenols in cyclohexane and ethanol has demonstrated that such PECs can nonetheless be instructive for aiding the interpretation of TA measurements,^{23,41} particularly when benchmarked against complementary gas-phase studies (such as TRPEI here). These calculations return an energy difference of $\Delta E_{\text{conf}} = 1860 \text{ cm}^{-1}$ between conformers **A** and **B** in S_0 , in good accord with previous literature.¹⁵ More generally, the profiles of both sets of PECs are qualitatively similar to those observed in many other phenols along their $R_{\text{O-H}}$ coordinates, which are well documented in the literature.^{42,43} Key features include the presence of a CI between the S_1 and S_2 states (S_1/S_2 CI) and, at a more elongated bond length, a CI between S_2 and S_0 (S_2/S_0 CI). There are however, quantitative differences between the PECs for **A** and **B**; most notably, the S_1/S_2 CI lies $\sim 1 \text{ eV}$ above the S_1 origin in **A**, whereas this energy difference is reduced to $\sim 0.7 \text{ eV}$ in **B**. To highlight this more clearly, Figure 3.11b shows the PECs for the S_1 and S_2 states rescaled on a ‘relative energy’ axis, such that the S_1 origin has been set to 0 eV in both conformers. The larger barrier area in **A**, relative to **B**, is a direct consequence of the intramolecular H-bond, which is only present in **A**.

After excitation to S_1 below the S_1/S_2 CI (*viz.* 267 nm) in many (but not all) substituted phenols, H-atom tunnelling through the barrier below the S_1/S_2 CI can occur and lead to O–H bond

3.11b. As with these other related systems, the location of the S_1/S_2 CI will dictate the relative barrier area which must be tunnelled through, and control the likelihood of any subsequent O–H bond fission. From Figure 3.11b it is clear that the predicted barrier area (along R_{O-H} only) in conformer **A** (red + blue shading) is ~ 2 times greater than the predicted barrier for conformer **B** (blue shading only), which will severely reduce the tunnelling probability for coupling between $S_1 \rightarrow S_2$ in **A** relative to **B**. Indeed, 1-D tunnelling calculations using a semiclassical Wentzel-Kramers-Brillouin (WKB) model,^{36,42} in conjunction with these PECs, return tunnelling probabilities of 2.7×10^{-12} and 2.7×10^{-6} from the zero-point vibrational level of the OH stretch ($v=0$) in S_1 ,⁴⁵ which subsequently transform into dramatically different tunnelling lifetimes of 3.5 ms and 3.4 ns for **A** and **B**, respectively.

With the findings from these calculations in mind, we can now return to understand our experimental observations of conformer specific dissociation dynamics across our different TA and TRPEI measurements. After excitation of conformer **A** at 267 nm in cyclohexane and the gas phase, VET (or solely IVR in the gas-phase) will occur with a rate k_{VET} , leading to population of the $v=0$ level in S_1 , on the order of a few picoseconds. From here, our calculations suggest that population decay from S_1 *via* tunnelling onto S_2 is a kinetically unfeasible relaxation pathway in **A**, due to the large barrier area under the S_1/S_2 CI. This prediction is in keeping with our experimental findings from *both* solution phase TA and gas phase TRPEI, which together indicate that decay of the S_1 state in **A** is primarily driven by ISC to T_n (k_{ISC}) and IC (k_{IC}) and fluorescence (k_F) back to the S_0 ground state. In conformer **B** however, which dominates our methanol TAS, our calculations predict a tunnelling barrier which is half that of **A**. This significantly reduced barrier area allows tunnelling (k_T) to become a kinetically competitive process for S_1 population decay in **B** (occurring in competition with k_{ISC} , k_F and k_{IC}), and serves to explain the observed production of guaiacoxyl radicals through O–H bond fission in our methanol TAS.

The substantial overlap between the guaiacoxyl radical absorption features and those of the S_1 ESA signal in our methanol TAS mean that it is currently non-trivial to deconvolute the precise appearance time of the radical photoproduct, although we note that its signature starts to appear after ~250 ps in Figure 3.3b. By way of comparison, we note that in previous TA work on phenol/cyclohexane²³ at 267 nm, the appearance of phenoxyl radicals (also proposed to be formed *via* tunnelling) was evident after ~1 ns. Despite the convoluted nature of our TAS, simple branched kinetics dictate that the appearance timescale of the guaiacoxyl radical should match the observed lifetime of the S_1 state (~3 ns). One may therefore tentatively assert that the S_1 lifetime will be commensurate with the appearance time of the guaiacoxyl radical, although we stress that further experiments (such as transient infra-red absorption spectroscopy^{24,25,46}) are needed to add further weight to this conclusion.

We close by acknowledging that our predictive capabilities of an accurate H-atom tunnelling lifetime in guaiacol (and other systems) are somewhat limited, although our value of 3.4 ns derived from the 1-D PECs in Figure 3.11 compares very favourably with the experimentally determined S_1 lifetime of ~3 ns for **B**. More detailed insight into the tunnelling lifetime for **B** would require knowledge of the *multidimensional* tunnelling barrier beneath the S_1/S_2 CI based on more complex calculated potential energy surfaces,⁴² which is beyond the scope of this current work. Perhaps more importantly though, we acknowledge that solvation will also affect the relative energies of the electronic states involved in this process.³⁴ Nonetheless, the combined theoretical and experimental approaches taken in this study, on the model system guaiacol, serve to re-enforce how different geometric conformations, induced by different solvent environments, can have a profound impact on electronic structure, which dictates the ensuing excited state dynamics. It is clear that combining such geometric and electronic structure information, together with a greater understanding of solvation, will be vital in furthering the comprehension of conformer specific photochemistry in a wide range of photoactive biomolecules and their subunits.

3.6. Conclusions

In summary we have found the photo-initiated dynamics of guaiacol to be highly conformer specific, which is imparted by the hydrogen-bonding nature and polarity of the solvent. In a solution of guaiacol in cyclohexane, we solely observe relaxation of S_1 excited state population in conformer **A**, with a time-constant of $\tau = 4.5 \pm 0.2$ ns, which is mediated primarily through ISC to lower lying T_n states and IC and fluorescence directly back to the S_0 ground state. Given that cyclohexane is a weakly interacting solvent the dynamics map on to those in the gas phase, where conformer **A** also dominates, as verified through highly complementary TRPEI studies. As a result of the intramolecular hydrogen bond in conformer **A**, which dominates in the ground state, H-atom loss *via* tunnelling and subsequent guaiacoxyl radical generation is not observed, due to a large barrier to dissociation.

Upon solvation of guaiacol in methanol, it is thought that conformer **B** now dominates in the ground state, and intramolecular H-bonding is now replaced by an intermolecular H-bond between the methanol solvent and the OH group. Relaxation of the S_1 excited state in **B** occurs with a time constant $\tau = 2.9 \pm 0.1$ ns. The presence of two peaks centred at 368 and 383 nm around ~250 ps onwards have been assigned to the formation of guaiacoxyl radical and are attributable to H-atom elimination from the OH group, mediated by a tunnelling mechanism. This process is found to be specific to conformer **B** by virtue of the smaller tunnelling barrier to dissociation in **B**, relative to **A**, as inferred through complementary theoretical calculations. As one may expect, the S_1 lifetime of **A** in cyclohexane matches more closely to the previously reported gas-phase lifetime of ~7 ns³² than that of **B** in methanol. The faster S_1 relaxation time of **B** is consistent with the postulate that tunnelling here presents an extra relaxation pathway, in addition to the fact that ISC is more efficient in polar solvents. This result serves to illustrate the importance of the solvent on the geometric structure, which converts an intramolecular H-bond to an intermolecular H-bond, essentially resulting in a 'free' O-H bond, which can then undergo H-atom elimination, akin to previous studies in related systems such as phenol and catechol.

The role that the solvent plays in determining geometric structure is clearly evident through these model studies. Further work of this nature will surely pave the way to increasing our understanding of *how* solvent-induced structural changes in photoactivatable biomolecules can manipulate the ensuing excited state dynamics, and ultimately, the species' biological function.

3.7. Bibliography

- (1) Park, S. T.; Kim, S. K.; Kim, M. S. *Nature* **2002**, *415*, 306.
- (2) Kim, M. H.; Shen, L.; Tao, H.; Martinez, T. J.; Suits, A. G. *Science* **2007**, *315*, 1561.
- (3) Tao, H.; Shen, L.; Kim, M. H.; Suits, A. G.; Martinez, T. J. *J. Chem. Phys.* **2011**, *134*, 054313.
- (4) Livingstone, R. A.; Thompson, J. O. F.; Iljina, M.; Donaldson, R. J.; Sussman, B. J.; Paterson, M. J.; Townsend, D. *J. Chem. Phys.* **2012**, *137*, 184304.
- (5) Oliver, T. A. A.; King, G. A.; Ashfold, M. N. R. *Chem. Sci.* **2010**, *1*, 89.
- (6) Oliver, T. A. A.; King, G. A.; Ashfold, M. N. R. *J. Chem. Phys.* **2010**, *133*, 194303.
- (7) Staniforth, M.; Stavros, V. G. *Proc. R. Soc. A* **2013**, *469*, 20130458.
- (8) Roberts, G. M.; Stavros, V. G. *Chem. Sci.* **2014**, *5*, 1698.
- (9) Arnaut, L. G.; Formosinho, S. J. *J. Photochem. Photobiol., A* **1993**, *75*, 1.
- (10) Formosinho, S. J.; Arnaut, L. G. *J. Photochem. Photobiol., A* **1993**, *75*, 21.
- (11) Douhal, A.; Lahmani, F.; Zewail, A. H. *Chem. Phys.* **1996**, *207*, 477.
- (12) Zhao, J.; Ji, S.; Chen, Y.; Guo, H.; Yang, P. *Phys. Chem. Chem. Phys.* **2012**, *14*, 8803.
- (13) Berinstain, A. B.; Whittlesey, M. K.; Scaiano, J. C. In *Photochemistry of Lignocellulosic Materials*; American Chemical Society: 1993; Vol. 531, p 111.
- (14) Lanzalunga, O.; Bietti, M. *J. Photochem. Photobiol., B* **2000**, *56*, 85.
- (15) Agache, C.; Popa, V. I. *Monatsh. Chem.* **2006**, *137*, 55.
- (16) Chang, H. T.; Su, Y. C.; Chang, S. T. *Polym. Degrad. Stab.* **2006**, *91*, 816.
- (17) Bonawitz, N. D.; Chapple, C. *Annu. Rev. Genet.* **2010**, *44*, 337.
- (18) Mu, W.; Ben, H.; Ragauskas, A.; Deng, Y. *BioEnergy Res.* **2013**, *6*, 1183.
- (19) Dean, J. C.; Navotnaya, P.; Parobek, A. P.; Clayton, R. M.; Zwier, T. S. *J. Chem. Phys.* **2013**, *139*, 144313.
- (20) Boerjan, W.; Ralph, J.; Baucher, M. *Annu. Rev. Plant Biol.* **2003**, *54*, 519.
- (21) Weng, J.-K.; Li, X.; Bonawitz, N. D.; Chapple, C. *Curr. Opin. Biotechnol.* **2008**, *19*, 166.
- (22) Varfolomeev, M. A.; Abaidullina, D. I.; Gainutdinova, A. Z.; Solomonov, B. N. *Spectrochim. Acta, Part A* **2010**, *77*, 965.

-
- (23) Zhang, Y.; Oliver, T. A. A.; Ashfold, M. N. R.; Bradforth, S. E. *Faraday Discuss.* **2012**, *157*, 141.
- (24) Harris, S. J.; Murdock, D.; Zhang, Y.; Oliver, T. A. A.; Grubb, M. P.; Orr-Ewing, A. J.; Greetham, G. M.; Clark, I. P.; Towrie, M.; Bradforth, S. E.; Ashfold, M. N. R. *Phys. Chem. Chem. Phys.* **2013**, *15*, 6567.
- (25) Harris, S. J.; Murdock, D.; Grubb, M. P.; Greetham, G. M.; Clark, I. P.; Towrie, M.; Ashfold, M. N. R. *Chem. Sci.* **2014**, *5*, 707.
- (26) Hermann, R.; Mahalaxmi, G. R.; Jochum, T.; Naumov, S.; Brede, O. *J. Phys. Chem. A* **2002**, *106*, 2379.
- (27) Bent, D. V.; Hayon, E. *J. Am. Chem. Soc.* **1975**, *97*, 2599.
- (28) Saperstein, D.; Levin, E. *J. Chem. Phys.* **1975**, *62*, 3560.
- (29) Abmann, J.; Kling, M.; Abel, B. *Angew. Chem., Int. Ed.* **2003**, *42*, 2226.
- (30) Owrutsky, J. C.; Raftery, D.; Hochstrasser, R. M. *Annu. Rev. Phys. Chem.* **1994**, *45*, 519.
- (31) Yuan, L.; Li, C.; Lin, J. L.; Yang, S. C.; Tzeng, W. B. *Chem. Phys.* **2006**, *323*, 429.
- (32) Chatterley, A. S.; Young, J. D.; Townsend, D.; Żurek, J. M.; Paterson, M. J.; Roberts, G. M.; Stavros, V. G. *Phys. Chem. Chem. Phys.* **2013**, *15*, 6879.
- (33) Thompson, J. O.; Livingstone, R. A.; Townsend, D. *J. Chem. Phys.* **2013**, *139*, 034316.
- (34) Bradforth, S. *Faraday Discuss.* **2012**, *157*, 243.
- (35) Dixon, R. N.; Oliver, T. A. A.; Ashfold, M. N. R. *J. Chem. Phys.* **2011**, *134*, 194303.
- (36) Roberts, G. M.; Chatterley, A. S.; Young, J. D.; Stavros, V. G. *J. Phys. Chem. Lett.* **2012**, *3*, 348.
- (37) King, G. A.; Oliver, T. A. A.; Dixon, R. N.; Ashfold, M. N. R. *Phys. Chem. Chem. Phys.* **2012**, *14*, 3338.
- (38) Yarkony, D. R. *Rev. Mod. Phys.* **1996**, *68*, 985.
- (39) Sobolewski, A.; Domcke, W.; Dedonder-Lardeux, C.; Jouvet, C. *Phys. Chem. Chem. Phys.* **2002**, *4*, 1093.
- (40) Shigematsu, M.; Kobayashi, T.; Tanahashi, M. *Jpn. Chem. Program Exchange J.* **2001**, *13*, 177.
- (41) Oliver, T. A. A.; Zhang, Y.; Ashfold, M. N. R.; Bradforth, S. E. *Faraday Discuss.* **2011**, *150*, 439.
- (42) Karsili, T. N. V.; Wenge, A. M.; Harris, S. J.; Murdock, D.; Harvey, J. N.; Dixon, R. N.; Ashfold, M. N. R. *Chem. Sci.* **2013**, *4*, 2434.
- (43) Karsili, T. N. V.; Wenge, A. M.; Marchetti, B.; Ashfold, M. N. R. *Phys. Chem. Chem. Phys.* **2014**, *16*, 588.
- (44) Pino, G. A.; Oldani, A. N.; Marceca, E.; Fujii, M.; Ishiuchi, S.-I.; Miyazaki, M.; Broquier, M.; Dedonder, C.; Jouvet, C. *J. Chem. Phys.* **2010**, *133*, 124313.
- (45) Experimentally determined ground state OH stretch vibrational frequencies were used to perform the 1-D BKW calculations. Frequencies of 3555 cm⁻¹ and 3600
-

cm^{-1} were used for conformers **A** and **B**, respectively, based on experimental findings in Ref. 22.

- (46) Murdock, D.; Harris, S. J.; Karsili, T. N. V.; Greetham, G. M.; Clark, I. P.; Towrie, M.; Orr-Ewing, A. J.; Ashfold, M. N. R. *J. Phys. Chem. Lett.* **2012**, *3*, 3715.

4.1. Introduction

The structure of the novel ruthenium complex, *cis*-[Ru(bpy)₂(NA)₂]²⁺ (bpy = 2,2'-bipyridine and NA = nicotinamide, pyridine-3-carboxamide), termed **1** hereon, is shown in Figure 4.1 inset. Following activation with light, this complex has potential for biological activity through both the release of nicotinamide and the generation of the chemically active Ru centre.¹⁻⁴ Given the high levels of cytotoxicity shown in similar Ru(II) anticancer complexes in the recent literature,³⁻⁹ **1** is likely to provide high cytotoxicity once activated. In aqueous solution, upon irradiation with UV or blue light, **1** undergoes solvolysis to form the mono-aquated photoproduct [Ru(bpy)₂(NA)(H₂O)]²⁺ (**2**). Continued irradiation (*ca.* 1 h) leads to the formation of the bis-aquated photoproduct [Ru(bpy)₂(H₂O)₂]²⁺ (**3**). These stepwise transformations are nicely indicated by the UV/Vis absorption spectra of Figure 4.1. The expected cytotoxicity of **2** and **3** comes about from the lability (better leaving groups) of the newly added H₂O ligand(s), which cater, for example, for crosslinking between two guanine residues. This chapter provides a detailed investigation into the excited state dynamics of the transformation of **1** to **2** (the transformation of **2** to **3** is much slower and beyond the time-window of our experiment) using a

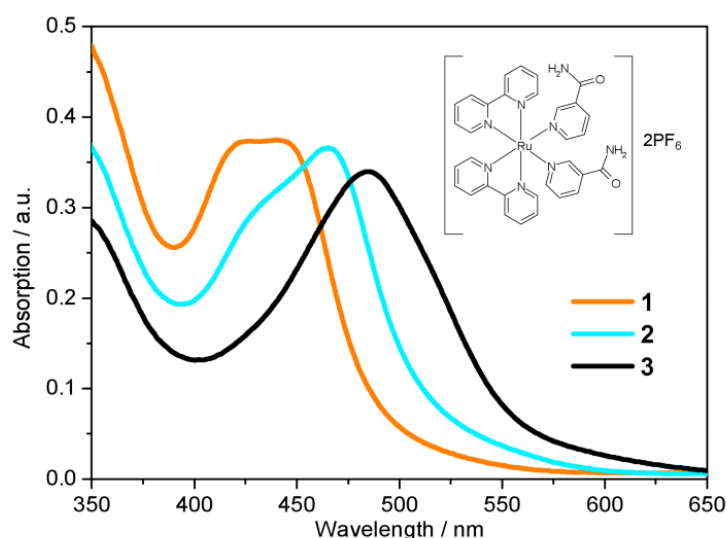


Figure 4.1 | Static UV/Vis absorption spectra of [Ru(bpy)₂(NA)₂]²⁺ (**1**, orange), [Ru(bpy)₂(NA)(H₂O)]²⁺ (**2**, cyan) and [Ru(bpy)₂(H₂O)₂]²⁺ (**3**, black). Irradiation of **1** with 465 nm for 50 s yields **2**. Further irradiation of **2** for 1 h 50 min yields **3**. Molecular structure of **1** is shown inset.

combination of TA in conjunction with detailed theoretical calculations (methods detailed in Appendix C) using density functional theory (DFT) and its time-dependent analogue (TD-DFT), in addition to the complete active space self-consistent field (CASSCF) method.

4.2. Methods

Static UV/Vis absorption spectra (shown in Figure 4.1) of a 40 μ M aqueous solution of **1** were recorded, using Perkin Elmer, *Lambda 25 UV/Vis spectrometer*, before and following excitation at 465 nm with a 50 mW blue LED, for up to 2 hrs. The identity of the mono-aqua adduct **2** was confirmed by mass spectrometry and high-performance liquid chromatography analysis indicated that only one isomer of **2** (see Section 4.3.7 for discussion) was present after irradiation, in-line with previous literature, which state that only the *cis*-**2**, and not *trans*-**2**, isomer will be generated.¹⁰

TA using 340 nm, 650 μ W excitation pulses and broadband white-light (350 to 650 nm) probe pulses, was used to follow the dynamics of an 890 μ M aqueous solution of **1** flowing through a flow cell, at pump-probe time delays ranging from $t = -1$ ps to 1.2 ns

The methodologies for ground state geometry and electronic spectroscopy calculations of **1**, **2**, and the pentacoordinate intermediate (PCI = [Ru(bpy)₂(NA)]²⁺, see Section 4.3.1) conducted using DFT and TD-DFT, respectively, as well as details of CASSCF calculations of the PCI excited state structure-dynamics, are described in Appendix C.

4.3. Results and Discussion

4.3.1. Static UV/Vis Absorption Spectra

Figure 4.1 shows the recorded UV/Vis absorption spectra of complex **1** before, and following excitation at 465 nm using a 50 mW blue LED. **1** has a broad visible absorption maximum, $\lambda_{\text{max}} = 420 - 450$ nm. Following 50 seconds of irradiation, the ground state absorption of **1** decayed and only the absorption of **2** was present with $\lambda_{\text{max}} = 465$ nm. We discuss the lack of

isomerisation (and its origins) further in Section 4.3.7. A further 1 h 50 min of irradiation was required to convert the entire sample to the bis-aqua complex, **3**, further red-shifting the λ_{max} to 483 nm. Power dependence studies of a similar complex (*cis*-[Ru(bpy)₂(CH₃CN)₂]²⁺) and the times of conversion indicated that the stepwise ligand exchange has two separate photochemical mechanisms.¹¹

Static UV/Vis absorption spectra in Figure 4.1 are used to benchmark complementary TD-DFT calculations. Calculated UV/Vis absorption spectra for complexes **1** and **2**, using the TD-B3LYP method, are presented in Figure 4.2a and b, respectively. The B3LYP functional together with an SDD 28 electron ECP (Ru) and a cc-pVTZ (H, C, O and N) basis set, was selected based on the best comparison with experimental findings. For complex **1**, Figure 4.2a shows very good agreement between the calculated spectra and the experimental spectrum. The TD-B3LYP calculations on **1** were performed both on the isolated gas phase species, as well as in the presence of an H₂O polarizable continuum model (PCM), in an attempt to capture some affects (if any) of solvation on the singlet electronic transitions. The results of both of these calculations are given in Figure 4.2(a), and show that for **1**, negligible changes to the energies of singlet electronic excitations are observed between the gas phase and H₂O PCM TD-B3LYP calculations, although an overall enhancement in the transition dipole moments (TDMs) for the dominant ‘bright’ transitions is observed (*cf.* oscillator strengths, *f*, given in Appendix C, Table C.1), the strongest of which belong to excitation of ¹MLCT states at 428 and 408 nm.

Results of analogous calculations for the mono-aqua photoproduct complex **2** are also presented in Figure 4.2b. These generate a UV/Vis absorption spectrum which is blue shifted by ~30 nm relative to experiment, for both the gas phase and H₂O PCM, although in good qualitative agreement with the experimentally observed profile. Once again, the major absorption signatures arise from bright ¹MLCT transitions, as with complex **1** (see Appendix C, Table C.1 and Figure C.1, for orbital transitions). Most notably, experimental findings clearly show an absorption red shift of ~30 nm upon evolution from the starting complex **1** to photoproduct **2**.

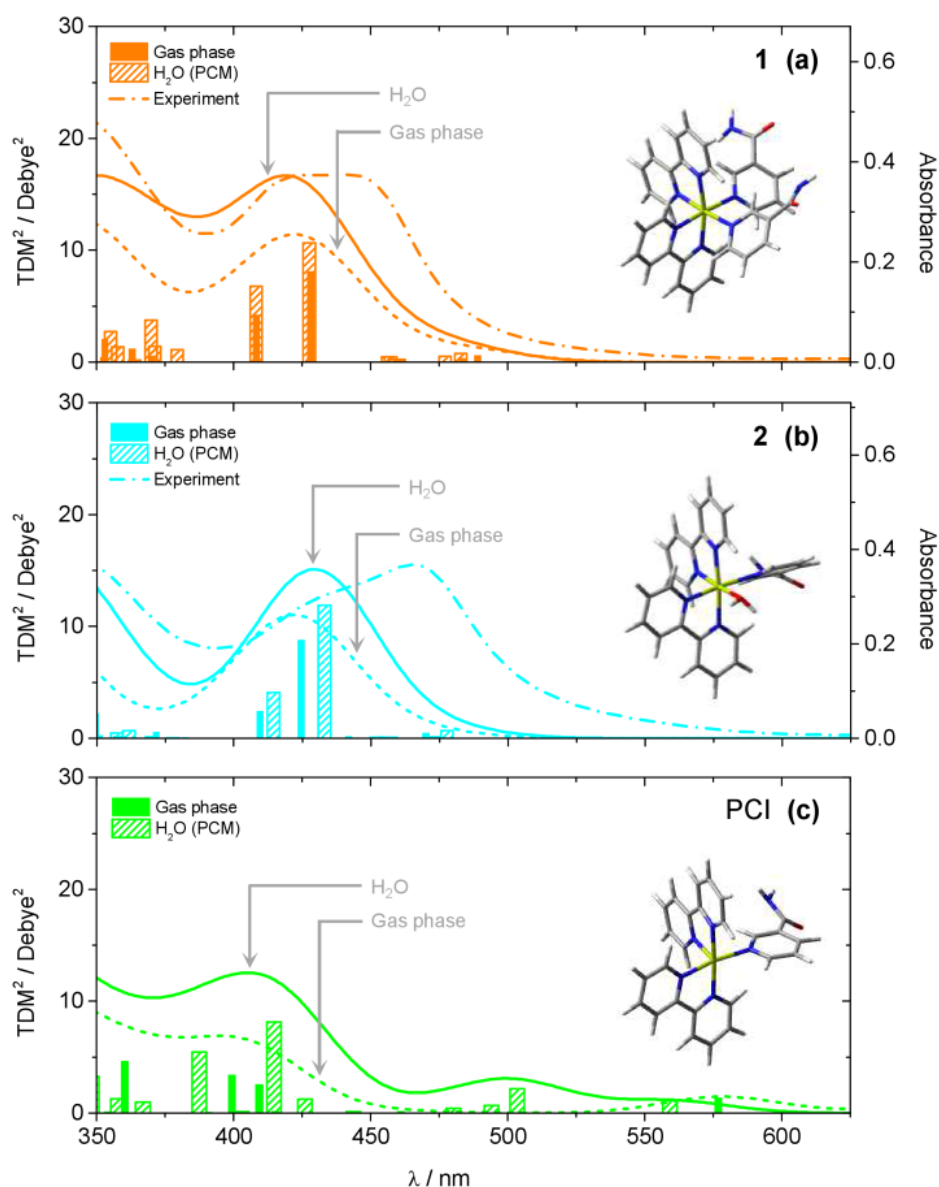


Figure 4.2 | Calculated static UV/Vis absorption spectra for (a) **1**, (b) **2** and (c) PCI, both in the gas phase (dotted lines) and with a H₂O PCM (solid lines). Calculated ground state structures shown inset. Spectra were calculated at the TD-B3LYP level of theory using a 28 electron SDD ECP for Ru and a cc-pVTZ basis set for C, O, N and H atoms. Calculated spectra were generated by convolution of the calculated squared transition dipole moments (TDM²) for singlet excitations with Gaussian functions (50 nm FWHM). Experimentally measured spectra for **1** and **2** from Figure 4.1 are shown in panels (a) and (b), respectively, for comparison (dashed-dotted lines).

Computationally, this red shift is only *qualitatively* captured upon inclusion of the H₂O PCM, while gas phase calculations predicted that **1** and **2** absorb at similar wavelengths. However, even with the inclusion of the H₂O PCM, the calculations only predict a red shift of ~5–10 nm

between **1** and **2** at this level of theory (N.B. similar shifts were observed with other functionals, *e.g.* PBE0). There may be several reasons for this discrepancy. (i) This may be a direct effect of solvation, and more in-depth solvation models (such as hybrid QM/MM methods^{12,13}), although beyond the scope of the present work, may be necessary to capture this behaviour fully. (ii) The TD-B3LYP calculations predict a number of singlet electronic states to lie below the bright ¹MLCT states (in both **1** and **2**), which have minimal transition strengths from the equilibrium ground states of **1** and **2**. Vibronic coupling, however, may lend transition strength to excitations through thermal population of low frequency vibrations modes in the ground state, which are not captured in these vertical excitation calculations. (iii) Finally, for both **1** and **2**, the bright ¹MLCT states will be strongly spin-orbit coupled with the analogous ³MLCT states, which lie lower in energy (see Appendix C, Table C.1); this assumption is reinforced by the fact that in [Ru(bpy)₃]²⁺, ISC between the ¹MLCT and ³MLCT states is observed to occur within ~100 fs.¹⁴

¹⁸ This spin-orbit coupling will lend transition strength for *direct* excitation to these (formally forbidden) ³MLCT states, and may also be responsible for contributing to the observed differences between the experimental and computational UV/Vis spectra.

4.3.2. TAS

Ultrafast UV/Vis TA was used to follow the dynamics of an 890 μM aqueous solution of **1** flowing through a flow cell, following excitation with a 340 nm, 650 μW pump pulse. Figure 4.3 shows TAS at pump-probe time delays ranging from $t = -1$ ps to 1.2 ns. We begin by focusing on the spectra recorded at early pump-probe delays shown in Figure 4.3a ($t < 25$ ps). Inspection of these spectra shows that several distinct regions can be identified immediately following excitation, related to the spectral location. A strong bleach signal is observed, centred on 420 nm (feature **ii**), which closely matches the spectral profile of the steady state absorption of **1** (Figure 4.1, orange line). As such, feature **ii** is assigned to the ground state bleach (GSB) signal of **1**. Relative to the absorption profile of **1** in Figure 4.1, a narrowing of the GSB feature **ii** is also observed at the ‘wings’ of the bleach (~400 and ~475 nm). This is due to overlap with

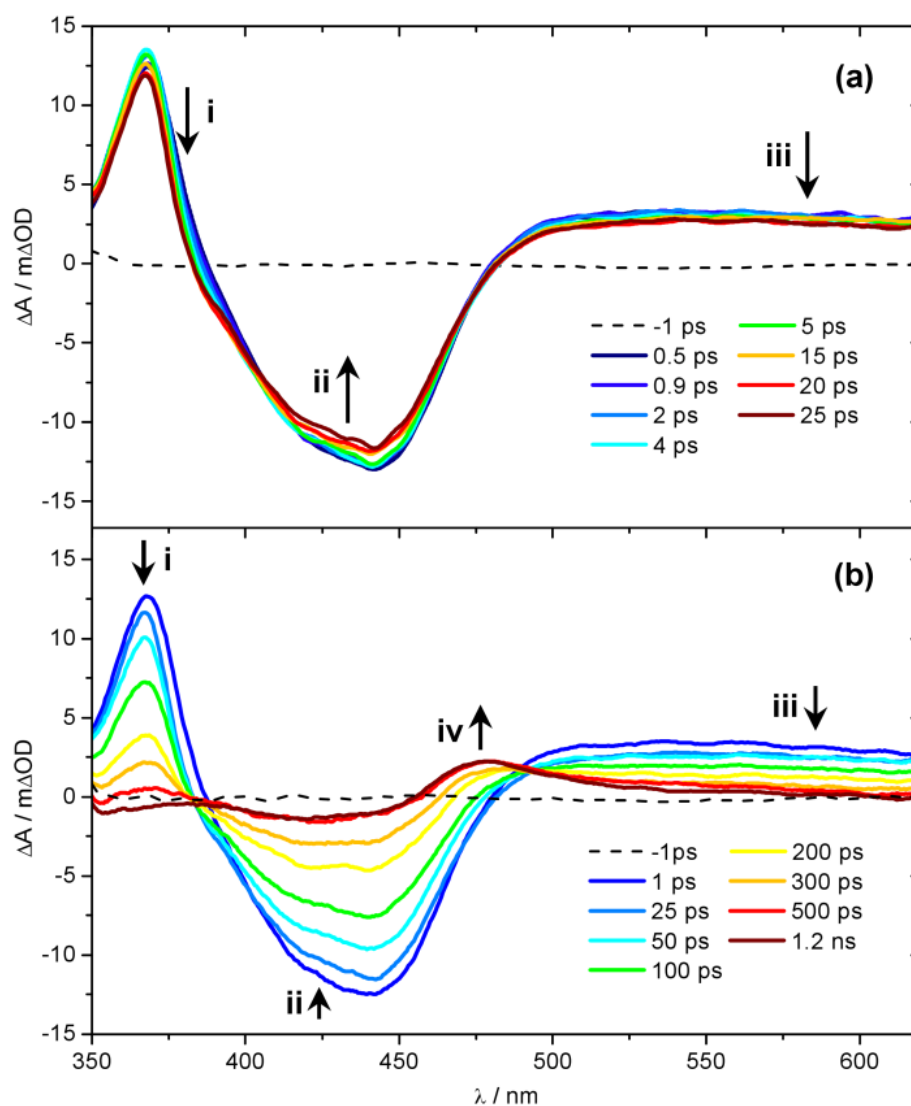


Figure 4.3 | UV/Vis TAS of 890 μ M aqueous solution of **1** over pump-probe delay ranges (a) $t = -1$ to 25 ps and (b) $t = -1$ ps to 1.2 ns, following photoexcitation at 340 nm. Growth/decay features **i** – **iv** highlighted, indicate the spectral location assigned to the ³MLCT ESA, GSB of **1**, absorption of the PCI and, finally, photoproduct **2**, respectively.

positive ΔOD signal either side of this feature, where ΔOD denotes the change in the optical density (absorbance). The strongest of these adjacent features, labelled **i** in Figure 4.3a, is centred at ~ 370 nm. UV/Vis spectroelectrochemistry measurements of [Ru(bpy)₃]²⁺¹⁹ and related complexes with functionalized bpy derivatives¹⁸ indicate that feature **i** can be assigned to an ESA of the ³MLCT excited state, and specifically corresponds to an absorption from the bpy anion (bpy⁻) present within the formally charge-separated character of the ³MLCT state (*i.e.*

[Ru^{III}(bpy)(bpy⁻)(NA)₂]²⁺).²⁰ Further comparison with earlier literature also indicates that there should be a second (less strong) ESA absorption signal associated with the ³MLCT state within the region ~450 – 550 nm.²¹ Between 450 – 500 nm any such signal will be strongly convoluted with the GSB feature **ii**. At $\lambda > 500$ nm; however, a broad plateau of transient absorption signal is observed. We therefore suggest that the absorption between 500 – 550 nm is primarily due to the ESA of the ³MLCT state.

At much longer wavelengths ($\lambda > 550$ nm), another absorbing species must be contributing to this plateau of transient absorption signal, labelled feature **iii**. Once again, comparison with earlier studies can prove instructive here. Very recently, further UV/Vis TAS measurements on [Ru(bpy)₃]²⁺ and its methylated derivatives by Hauser and co-workers,²² have suggested that absorption in this region of the TAS is due to ESA of the ³MC state. In these bidentate-ligand chelated complexes, at larger Ru–N(bpy) bond distances the ³MC surface will exhibit notable bound character, as complete Ru–N(bpy) bond fission is necessarily aborted (see Figure 4 in Ref. 22), enabling population to become trapped transiently in the ³MC state, prior to population transfer back to the ground state. This behaviour will extend the lifetime of population in the ³MC state and make it spectroscopically detectable in the TAS measurements. However, the analogous ³MC state in **1** will be purely repulsive with respect to bond fission, meaning that any population transferred to the ³MC state will undergo rapid (ultrafast) dissociation into a PCI complex and NA ligand, rather than being transiently trapped on this surface. Calculated profiles of the ³MC state along the Ru–N(py) dissociation coordinate in the related *cis*-[Ru(bpy)₂(py)₂]²⁺ complex support this picture.²³ Such a scenario would make it unlikely that any fleeting population in the ³MC state is observable in **1**. In earlier TAS work on *cis*-[Ru(bpy)₂(CH₃CN)₂]²⁺ by Turro and co-workers, a similar signal was instead assigned to absorption of a PCI complex, although limited justification was provided for this assignment.¹¹ To add weight to this postulate here, we have also performed TD-B3LYP calculations in an attempt to predict the absorption profile of the PCI complex, the results of which are shown in

Figure 4.2c. Unlike complex **1** and the mono-aquated photoproduct **2** (Figure 4.2a and b, respectively), the calculated absorption profiles for the PCI (in the gas phase and H₂O PCM) indeed *qualitatively* suggest that: (i) its absorption cross-section is weaker than **1** and **2**; and (ii) it should absorb weakly into the ‘red end’ of our experimental detection window in the TAS ($\lambda > 550$ nm). Given this, we are therefore inclined to assign feature **iii** to absorbance of the PCI complex, [Ru(bpy)₂(NA)]²⁺, in concord to earlier work by Turro and co-workers.¹¹ The presence of feature **iii** in the TAS at the earliest pump-probe delays ($t = 0.5$ ps) also confirms that any Ru–NA bond fission occurs on a sub-picosecond timeframe.

Having assigned the main features in Figure 4.3a, we now consider any observed temporal evolution at early time-delays ($t < 25$ ps). In general, all three labelled features in Figure 4.3a begin to deplete within the first 25 ps. Perhaps most significant though is the evolution of the ³MLCT ESA feature **i**, which both begins to deplete, spectrally narrow and blue-shift over this timeframe. Such behaviour can be broadly attributed to vibrational cooling of the nascent ³MLCT state occurring over the timescale of a few picoseconds and we return to consider this behaviour in greater detail below. Similar depletion of the signal associated with the PCI feature **iii** may also indicate rapid cooling of any nascent PCI species, or alternatively may be due to a structural rearrangement of the PCI after it is formed – we examine this further in Section 4.3.7. Finally, the apparent depletion of the GSB feature **ii** is most likely attributable to the vibrational cooling dynamics in the spectrally overlapped ³MLCT ESA signal, rather than any rapid repopulation of the ground state of **1**.

Figure 4.3b follows the dynamics of these features to longer time delays ($t = 1.2$ ns). The GSB feature **ii** recovers whilst the ³MLCT ESA feature **i** and the PCI feature **iii** concomitantly decay over the following few hundred picoseconds and a new absorption feature centred at 475 nm (labelled feature **iv**) emerges at $t > 300$ ps, reaching a maximum intensity after ~500 ps. The growth of feature **iv** results in a *quasi*-isosbestic point at 490 nm as this new feature rises and the ³MLCT ESA and PCI absorption features at $\lambda > 500$ nm decay over this time window. We

attribute this absorption to mono-aquation of the PCI and the formation of photoproduct **2**, as the location of feature **iv** is concordant with the static UV/Vis absorption spectrum of **2** in Figure 4.1 (cyan line). The formation of a photoproduct is in-line with the fact that the GSB feature **ii** never fully recovers back to a baseline signal of $\Delta OD = 0$, confirming that some portion of initially photo-excited population in **1** never returns to the ground state. Further confirmation of the assignment of feature **iv** to the formation of **2** can be seen when TAS measurements on **1** are recorded from an acetone solution (shown in Figure 4.4); acetone is a weakly coordinating ligand compared to H₂O. In this comparative data set (i) no obvious transient absorption signal of a ligand substituted photo-product is present within our probe window of 340 – 700 nm and (ii) the GSB feature fully recovers to a baseline of $\Delta OD = 0$, suggesting an absence of any significant photoproduct build up (even if its absorption signature were to lie outside our probe window).

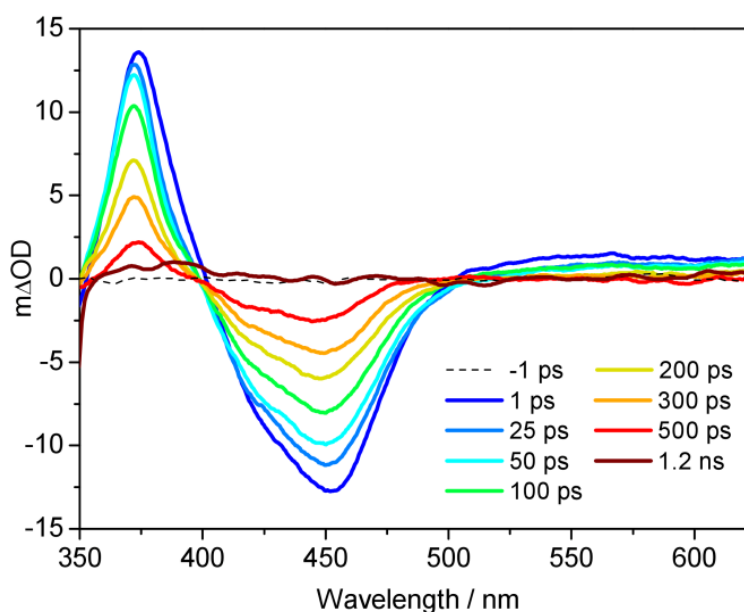


Figure 4.4 | UV/Vis TAS of 890 μ M solution of **1** in acetone over pump-probe delay ranges $t = -1$ ps to 1.2 ns, following photoexcitation at 340 nm. The ground state bleach of **1** is spectrally red-shifted in acetone relative to H₂O.

4.3.3. Target Analysis of TAS

In earlier ultrafast transient absorption studies of related Ru(II) complexes, a more quantitative insight into the timescales for ³MLCT state decay (and vibrational cooling), GSB recovery, decay of the PCI species and the formation of the mono-aquated photoproduct was attempted by integrating ‘slices’ through different spectral regions of the recorded TAS and then fitting the decay/growth of these traces to either mono- or bi-exponential functions.¹¹ However, given that many of the spectral signatures for each of these individual species are heavily convoluted within the recorded TAS (*vide supra*), such an analysis can return misleading timescales and quantum yields (ϕ) for the dissociation dynamics (*e.g.* Figure 4.1 clearly shows that the spectral signatures for **1** and **2** are strongly overlapped). In an attempt to circumvent this issue, we elect instead to perform a ‘target analysis’ of the TAS by fitting each of the time-resolved spectra with appropriate basis functions (associated with each of the absorption/bleach features) using the spectral analysis package KOALA.²⁴ For further details on the exact methods used in this fitting program the reader is referred to the comprehensive description of KOALA provided in Ref. 24.

Integration of each of these fitted basis functions as a function of time then returns kinetic traces that solely correlate to the population dynamics of individual species involved in the dissociation of **1** (see Section 4.3.5). Representative fit examples, obtained for time-resolved spectra recorded at $t = 1$ ps and 1 ns, are given in Figure 4.5a and b, respectively. The static UV/Vis absorption spectra recorded for **1** and **2** in Figure 4.1 are used as basis functions for modelling the evolution of the GSB of **1** and the formation of photoproduct **2** (orange and cyan lines, respectively). For the ³MLCT component, two Gaussians are used to approximate the ESA profile (blue line), with their precise locations, relative amplitudes and widths based on the known spectral profile of the bpy[−] absorption of similar complexes.¹⁸⁻²¹

Finally, the spectral profile of the PCI species present at long wavelengths is modelled with a broad Gaussian function (green line). In the case of the PCI, we acknowledge that, like **1** and **2**,

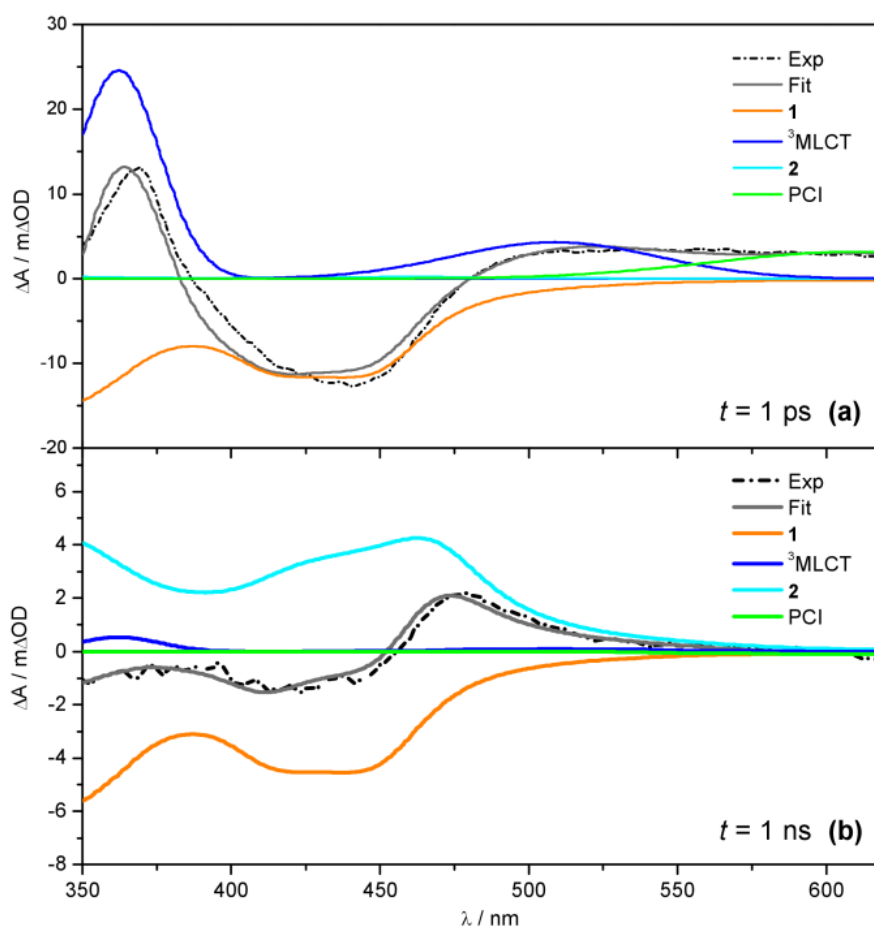


Figure 4.5 | Representative fits (grey) to transient absorption spectra (black dashed) at (a) $t = 1$ ps and (b) $t = 1$ ns, showing the individual basis functions used in the ‘target analysis’ of the TAS in Figure 4.3. Basis functions have been assigned to the ³MLCT ESA (blue), PCI complex (green), GSB recovery of **1** (orange) and formation of the photoproduct **2** (cyan). Static UV/Vis absorption spectra in Figure 4.1 are used as basis functions for **1** and **2**.

TD-B3LYP calculations predict this species should also absorb in the blue end of our detection window ($\lambda < 450$ nm), albeit less strongly (see Figure 4.2c). However, attempts to include this behaviour make the target analysis far more cumbersome, due to the multiple absorbing species in this spectral region. To make the analysis feasible, we therefore elect to only model the PCI absorption at $\lambda > 550$ nm. The representative fits in Figure 4.5 serve to highlight the convoluted nature of the final TAS. This is particularly clear at longer time-delays (Figure 4.5b, $t = 1$ ns) where the remaining GSB signal for **1** and the photoproduct **2** are directly overlapped at $\lambda < 450$ nm, and the sum of the basis function profiles generated in the fit (grey line) replicates the experimental spectrum (black dashed line) exceptionally well.

4.3.4. Kinetic Model for Dissociation of *cis*-[Ru(bpy)₂(NA)₂]²⁺

Before proceeding with any fitting of these traces, we first establish a full kinetic model for the dissociation of **1** by considering the dynamical pathways that give rise to Ru–NA bond fission, as well as any (dominant) competing relaxation processes. We herein discuss these with reference to the scheme in Figure 4.6.

The predominant models for photo-induced ligand exchange/dissociation in similar Ru(II) complexes in the literature, propose extremely efficient traversal of excited state flux from the vertical Franck-Condon excitation region of the ¹MLCT state(s) to the PCI *via* ³MLCT state(s) and a dissociative ³MC state. Following ISC and geometry rearrangements, the PCI can then accommodate the addition of an H₂O molecule to yield **2**. To help construct such a model for **1**, and to gain some insight into the relative energies of the ¹MLCT, ³MLCT and ³MC states postulated to drive ligand dissociation, we once again turn to our complementary TD-DFT calculations. The results of these TD-B3LYP calculations (summarised in Appendix C, Table C.1) show an optically bright ¹MLCT centred around 2.90 eV (428 nm), in both the gas phase and with a H₂O PCM. This state is the central component of the ‘triply degenerate’ state (split by only ~0.15 eV) that one would expect in a d⁶ metal complex with metal- π interactions.

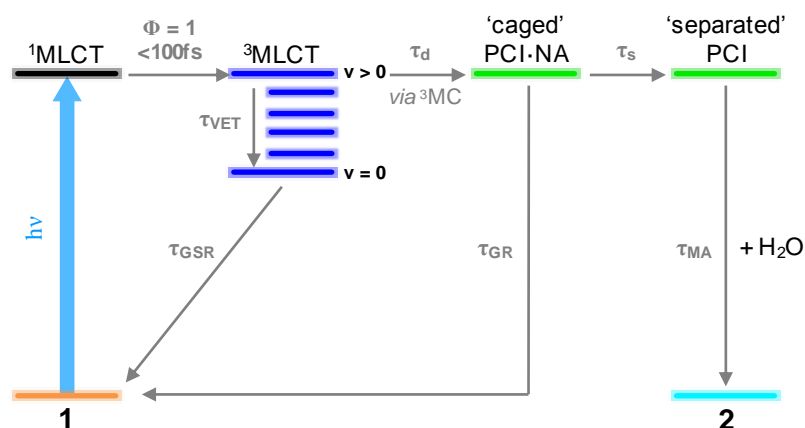


Figure 4.6 | Kinetic scheme illustrating the major pathways and associated time constants (τ), used to model the photodissociation dynamics of **1** in H₂O. The individual steps involved in this kinetic scheme are discussed further in the main text (Section 4.3.4).

Analysis of the (dominant) orbital transition associated with this state confirms it to be of MLCT type, with the relevant orbital transition shown in Appendix Figure C.1a (LUMO \leftarrow HOMO-2). A higher energy, but more weakly absorbing, ¹MLCT component is identified to lie at 3.04 eV (408 nm), with the associated orbital transition for this state shown in Appendix Figure C.1b (LUMO+1 \leftarrow HOMO-2); for both of these ¹MLCT states the associated orbital transitions further highlight their formally charge separated [Ru^{III}(bpy)(bpy⁻)(NA)₂]²⁺ character (*vide supra*). Based on the oscillator strengths, f , returned by the TD-B3LYP calculations, the absorption of photons with energy around 2.90 eV or higher, *viz.* $\lambda_{\text{excitation}} = 340$ nm (4.76 eV), will most likely result in the initial population of highly electronically excited ¹MLCT states, rather than ¹MC states (see Appendix C, Table C.1), followed by ultrafast internal conversion to the lower energy ¹MLCT states. We note for completeness that the TAS pump wavelength of 340 nm is selected since it lies outside our probe window and thus avoids contaminating part of our TAS spectra.

The associated ³MLCT state (of analogous LUMO \leftarrow HOMO-2 character) is calculated to lie at ~2.70 eV (~458 nm); ~0.2 eV lower in energy than ¹MLCT (see Appendix C, Table C.1). Similarly, the ³MLCT state dominated by the LUMO+1 \leftarrow HOMO-2 transition lies lower in energy again at ~2.65 eV (~468 nm). The high-density of states will promote very efficient vibronic coupling *via* multiple Jahn-Teller (JT) and *pseudo*-JT type couplings between these ¹MLCT and ³MLCT potential energy surfaces.²⁵ For the archetypal complex, [Ru(bpy)₃]²⁺, ¹MLCT \rightarrow ³MLCT ISC is reported to: (i) possess a (near) unity quantum yield ($\phi \sim 1$);²⁶ and (ii) be ultrafast (~100 fs^{24,64-67}), leading to a non-thermally equilibrated (vibrationally excited/hot) ³MLCT state, henceforth termed ³MLCT_{v>0} in Figure 4.6.²⁷ McGarvey and co-workers²⁸ found there to be remarkably little difference in ¹MLCT \rightarrow ³MLCT_{v>0} coupling within the [Ru(bpy)₃]²⁺ complex and other similar complexes, where similar sub-picosecond population of ³MLCT_{v>0} state(s) is also observed. Such behaviour is also consistent with observations from our TAS spectra of **1** in Figure 4.3, which indicate that population is present in the ³MLCT state at our

earliest recorded time-delay ($t = 0.5$ ps), and confirms that $^1\text{MLCT} \rightarrow ^3\text{MLCT}_{v>0}$ ISC occurs on a sub-500 fs timeframe.

Once populated, intramolecular and/or intermolecular (solute-solvent mediated) vibrational relaxation (collectively termed vibrational energy transfer (VET)²⁹) of $^3\text{MLCT}_{v>0}$ may subsequently occur with a lifetime τ_{VET} , leading to the formation of a vibrationally-cold $^3\text{MLCT}$ state, termed $^3\text{MLCT}_{v=0}$, as indicated in the schematic in Figure 4.6. Once again, this is consistent with our observations for band narrowing of the $^3\text{MLCT}$ ESA feature **i** at $t < 25$ ps in Figure 4.3a. Integrating the signal on the ‘red edge’ ($\lambda = 375 - 380$ nm) of the $^3\text{MLCT}$ ESA feature **i** in Figure 4.3a yields the kinetic trace in Figure 4.7e, which when fitted to a bi-exponential decay returns a time-constant of 3.6 ps for τ_{VET} (see Table 4.1). Once cooled, the population located in $^3\text{MLCT}_{v=0}$ may then undergo relaxation (*via* either ISC or phosphorescence) back to the singlet electronic ground state of **1** (ground state recovery, GSR) with a time constant τ_{GSR} , which based on observations in Figure 4.3b and the kinetic trace for $^3\text{MLCT}$ in Figure 4.7a, must occur over a longer timeframe of hundreds of picoseconds.

In addition to the VET and recovery of the ground state of **1** from the $^3\text{MLCT}$ state, population in this state must also couple onto a neighbouring dissociative ^3MC surface to drive Ru–NA bond fission.¹⁰ The TD-B3LYP calculations (see Appendix C, Table C.1) predict the lowest energy of these ^3MC states to lie between $\sim 2.9 - 3.0$ eV (425 – 413 nm), ~ 0.25 eV higher in energy than the lower lying $^3\text{MLCT}$ (LUMO \leftarrow HOMO–2) state in the vertical Franck-Condon region. The dominant orbital transition associated with this ^3MC state (LUMO+10 \leftarrow HOMO, see Appendix Figure C.1c) populates an anti-bonding MC orbital which has strong $4d_{x^2-y^2}$ character and is dissociative with respect to both of the Ru–NA dative bonds (as well as the equatorial Ru–N(bpy) bonds). For completeness, the analogous ^1MC state is calculated to lie at ~ 3.6 eV (~ 345 nm). We recall that, as with the $^3\text{MLCT}$ ESA feature **i** in Figure 4.3, a transient absorption signature for the nascent PCI species, formed as a result of Ru–NA dissociation, is

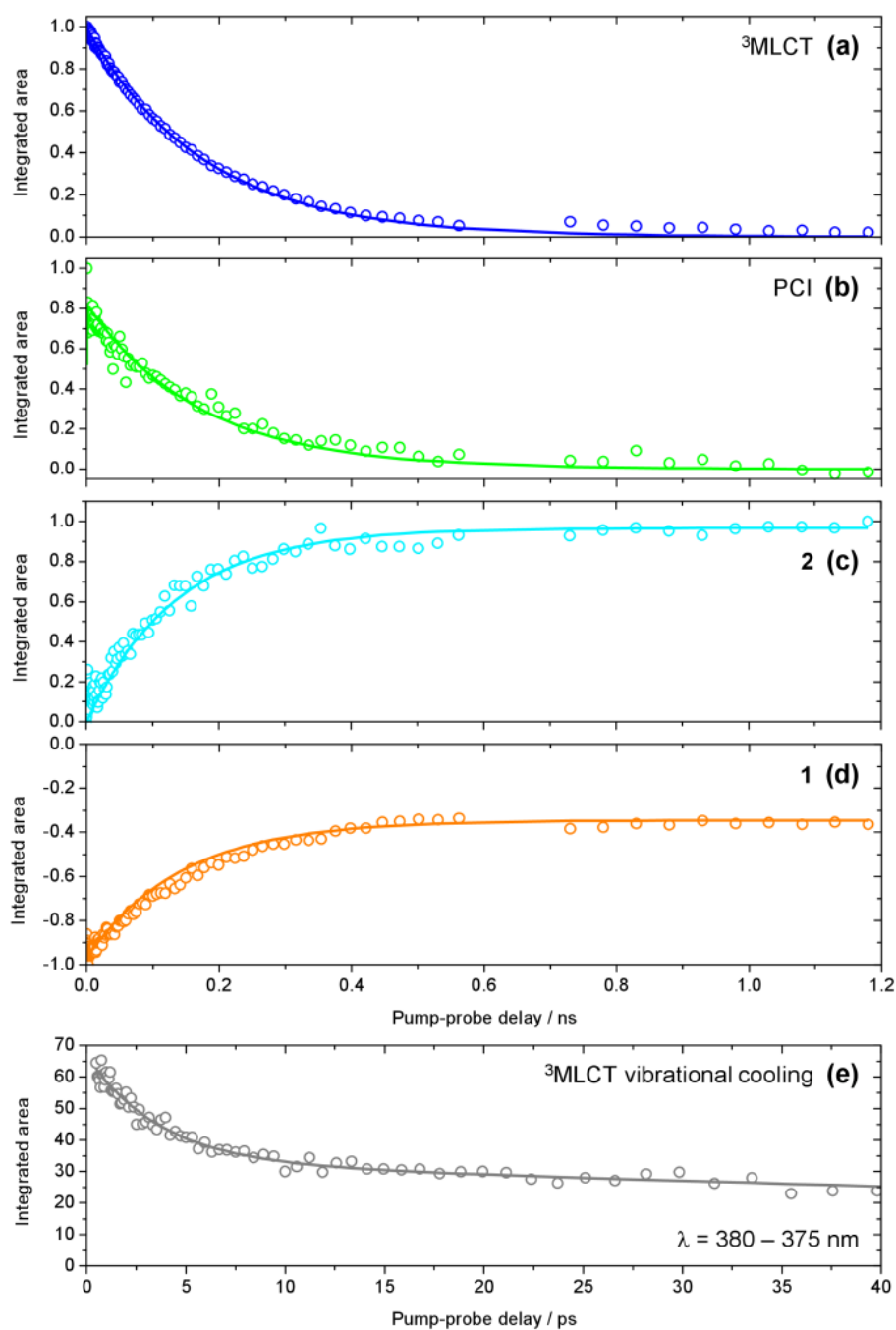


Figure 4.7 | (a – d) Kinetic traces for the time-dependent evolution of the ³MLCT state population (blue), PCI (green), photoproduct **2** (cyan) and GSB recovery of **1** (orange), obtained by integration of the basis functions (see Figure 4.5) used in the ‘target analysis’ of the TAS in Figure 4.3. Kinetic fits to these traces, in accordance with the scheme in Figure 4.6, are shown by the solid lines – see main text for details. (e) Kinetic trace reflecting the vibrational cooling of the ³MLCT state at $t < 40$ ps (grey squares), obtained by integration of the ‘red edge’ of the ³MLCT feature **i** in Figure 4.3a over a range $\lambda = 375 - 380$ nm. The solid grey line represents a fit to the trace with a bi-exponential decay function.

also observed at the earliest time-delay of $t = 0.5$ ps in the TAS, indicating that Ru–NA bond fission must also occur on a sub-500 fs timeframe, with a time-constant τ_d . Based on simple kinetics grounds, if coupling onto the ³MC surface were barrierless (*i.e.* accessible from both the ³MLCT_{v>0} and ³MLCT_{v=0} levels), the observed lifetime of the ³MLCT state should in turn be solely defined by the rapid dissociation lifetime τ_d . However, this picture is clearly not consistent with general observations from Figure 4.3 and the kinetic trace for ³MLCT in Figure 4.7a, which decays over hundreds of picoseconds, rather than a sub-500 fs timeframe. Given this, we invoke a simple model where a barrier to dissociation (coupling onto the ³MC state) can only be surmounted from a vibrationally hot ³MLCT_{v>0} state; the presence of a barrier to coupling between ³MLCT and ³MC states is generally supported by the fact that our TD-B3LYP calculations predict the ³MC to lie above the ³MLCT in the vertical Franck-Condon region.³⁰ Within this model, VET out of the ³MLCT_{v>0} level over $\tau_{\text{VET}} = 3.6$ ps acts as a ‘time dependent switch’, preventing population transfer between ³MLCT and ³MC states as the process becomes energetically inaccessible (a barriered process) after population is funnelled into ³MLCT_{v=0}. Figure 4.6 therefore shows that population subsequently trapped in ³MLCT_{v=0} following VET may then only undergo relaxation back to the ground state of **1**.³¹

Immediately after dissociation, the size of both the PCI complex and NA ligand will mean that they undergo strong caging within the solvation shell, and can be viewed as ‘loosely associated’, as illustrated pictorially in Figure 4.8. These nascent caged photoproducts, henceforth labelled PCI·NA (Figure 4.8), may then geminately reform the initial complex **1** with a time-constant τ_{GR} , or alternatively undergo some degree of diffusional separation on a timescale τ_s . The later of these processes will yield the formation of a PCI complex that may then accept a free H₂O solvent molecule into its now open coordination site, simply termed ‘separated’ PCI in Figure 4.8, and undergo mono-aquation to form the final photoproduct **2** on a timescale τ_{MA} .

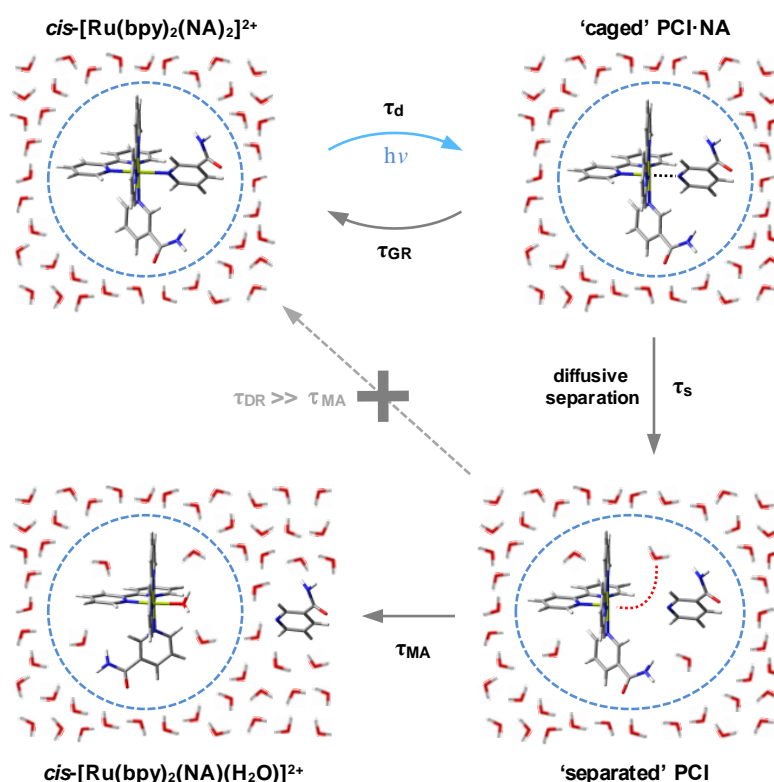


Figure 4.8 | Pictorial schematic of the post-dissociation processes involving the PCI and formation of the photoproduct **2**.

The above kinetic picture of dissociation is broadly consistent with phenomenological models used to treat VET, bond fission, caging and diffusional separation/escape dynamics observed in ultrafast photodissociation studies of smaller organic species.^{32,33} However, before proceeding further we first briefly justify some of the inherent assumptions surrounding the aforementioned picture, for the dissociation of **1** in H₂O. (i) After dissociation the 'caged' PCI·NA pair are in close proximity and as a result we make the assumption that direct formation of **2** from this species will be strongly hindered on steric grounds – hence this pathway is absent in Figure 4.8. (ii) After some degree of diffusional separation, the 'separated' PCI and NA species may in principle re-encounter one another, leading to a 'diffusive recombination' pathway for the reformation of **1**, rather than the production of **2**. However, given the vast excess of H₂O solvent molecules, and their relative lability compared to the bulkier PCI and NA, we propose that τ_{MA} will strongly out-compete any timescale for diffusive recombination, τ_{DR} (*i.e.* $\tau_{DR} \gg \tau_{MA}$). As

such, τ_{DR} is neglected in our kinetic model for the dissociation of **1** in H₂O in Figure 4.6, and is represented as a kinetically inactive channel for the post-dissociation processes illustrated in Figure 4.8, which we justify further below.

4.3.5. Kinetic Analysis

Integration of the fitted basis functions from the target analysis (as described in Section 4.3.3) for the ³MLCT ESA, GSB recovery of **1**, the PCI and the growth of photoproduct **2** are presented in Figure 4.7a – d. Using the kinetic model shown in Figure 4.6 for the photodissociation of **1** in H₂O, full kinetic fits to the traces were performed. These traces, presented in Figure 4.7a – d, were *simultaneously* fit to the analytical solutions for the time-dependent populations of each of these species within our model in Figure 4.6. The rate equations of the states (shown in Figure 4.6) involved in the dynamics of **1** in H₂O are:

$$\frac{d[{}^3\text{MLCT}_{v>0}]}{dt} = -(k_{\text{VET}} + k_d)[{}^3\text{MLCT}_{v>0}] \quad [{}^3\text{MLCT}_{v>0}](0) = A_0 \quad (4.1)$$

$$\frac{d[{}^3\text{MLCT}_{v=0}]}{dt} = k_{\text{VET}}[{}^3\text{MLCT}_{v>0}] - k_{\text{GSR}}[{}^3\text{MLCT}_{v=0}] \quad [{}^3\text{MLCT}_{v=0}](0) = 0 \quad (4.2)$$

$$\frac{d[\text{PCI} \cdot \text{NA}]}{dt} = k_d[{}^3\text{MLCT}_{v>0}] - (k_s + k_{\text{GR}})[\text{PCI} \cdot \text{NA}] \quad [\text{PCI} \cdot \text{NA}](0) = 0 \quad (4.3)$$

$$\frac{d[\text{PCI}]}{dt} = k_s[\text{PCI} \cdot \text{NA}] - k_{\text{MA}}[\text{PCI}] \quad [\text{PCI}](0) = 0 \quad (4.4)$$

$$\frac{d[\mathbf{2}]}{dt} = k_{\text{MA}}[\text{PCI}] \quad [\mathbf{2}](0) = 0 \quad (4.5)$$

$$\frac{d[\mathbf{1}]}{dt} = k_{\text{GSR}}[{}^3\text{MLCT}_{v=0}] + k_{\text{GR}}[\text{PCI} \cdot \text{NA}] \quad [\mathbf{1}](0) = -A_0 \quad (4.6)$$

where k_{VET} , k_d , k_s , k_{GSR} , k_{GR} , k_{MA} are rate constants of vibrational energy transfer, dissociation, ligand separation, ground state recovery, geminate recombination and mono-aquation, respectively. As we are blind to ¹MLCT → ³MLCT_{v>0} intersystem crossing, and this occurs within our instrumental resolution, we set time $t = 0$ for the kinetic analysis from the event of population of ³MLCT_{v>0}. The initial excited state

population transferred from the ¹MLCT following irradiation, [³MLCT_{v>0}](0), is given as A_0 and the ground state bleach of **1** at $t = 0$, [**1**](0), is thus $-A_0$.

Equations 4.1 to 4.6 are solved analytically to give exponential equations that are used to *simultaneously* fit kinetic traces (shown in Figure 4.7). For example, Equation 4.1 gives:

$$[{}^3MLCT_{v>0}](t) = A'e^{-(k_d+k_{VET})t} \quad (4.7)$$

A' is an amplitude for the exponential function which indicates signal intensity *i.e.* it replaces A_0 (population only) to take into account oscillator strengths of transitions that contribute to the observed signal.

We note that during this fitting procedure, the τ_{VET} timescale of 3.6 ps, extracted earlier from Figure 4.7e, is held fixed. Given that our kinetic model in Figure 4.6 displays branched kinetic pathways, fixing τ_{VET} helps to make the fitting procedure more reliable (and less cumbersome). The results of these fits are presented as solid lines through the data sets in Figure 4.7a – d, and the time-constants returned are collated in Table 4.1.

For the case of the ³MLCT feature in Figure 4.7a, this trace is fitted to both the kinetic equations for ³MLCT_{v>0} and ³MLCT_{v=0}, given that they will both contribute to this feature. Similarly, the PCI feature in Figure 4.5b is fitted with the equations for both the ‘caged’ PCI·NA and ‘separated’ PCI species in our model, as they will both possess the same spectral signature. In this case though, the amplitude of the ‘separated’ PCI component required to fit this trace is found to be negligible. This is in-line with the time-constants returned by the kinetic fits, which indicate that the steady-state population of the ‘separated’ PCI complex will be minimal, as it is rapidly consumed to generate the mono-aquated photoproduct **2**, with a timescale of $\tau_{MA} < 1$ ps.

More generally the results of this analysis confirm that Ru–NA bond fission, *via* coupling from ³MLCT_{v>0} onto the dissociative ³MC state, does indeed occur on a sub-picosecond timeframe ($\tau_d = 0.4$ ps). After dissociation into ‘caged’ PCI·NA species, geminate reformation of **1** or

diffusive separation, forming ‘separated’ PCI complexes, occur. Both are strongly competitive processes, taking place on the order of a few hundred picoseconds ($\tau_{\text{GR}} = 263$ ps and $\tau_s = 377$ ps). For the fraction of PCI·NA that do go on to form ‘separated’ PCI complexes, the PCI may then rapidly accommodate a H₂O solvent molecule into the now open coordination site ($\tau_{\text{MA}} < 1$ ps), and our analysis indicates that it is the diffusional separation/reorganization process from ‘caged’ PCI·NA to ‘separated’ PCI that acts as the rate limiting step to the formation of photoproduct **2** (*i.e.* $\tau_{\text{MA}} \ll \tau_s$) – hence the observed build-up of **2** over hundreds of picoseconds in the TAS. Moreover, the hundreds of picoseconds timeframe extracted for diffusive separation, further serves to confirm our assertion from Section 4.3.4 that diffusive recombination, τ_{DR} , of the separated PCI and NA in aqueous solution (which is also a diffusion limited process) must also occur over a similar timeframe post-separation, and as such can be negated from our kinetic model in Figure 4.6, as $\tau_{\text{MA}} \ll \tau_{\text{DR}}$. In tandem with these dissociative pathways, a fraction of the population initially present in $^3\text{MLCT}_{v>0}$ will be vibrationally quenched into a cold $^3\text{MLCT}_{v=0}$ state ($\tau_{\text{VET}} = 3.6$ ps), and from here undergo relaxation back to the ground state of **1** with a time constant of $\tau_{\text{GSR}} = 180$ ps.

4.3.6. Quantum Yields

In the above kinetic analysis, we have assumed that *all* population initially imparted to the optically bright $^1\text{MLCT}$ state by the excitation pulse is transferred through ISC to the $^3\text{MLCT}$ surface.²⁶ In assuming this initial $^1\text{MLCT} \rightarrow ^3\text{MLCT}_{v>0}$ ISC quantum yield to be unity ($\phi = 1$), subsequently we can extract values for ϕ for all of the remaining processes within our kinetic model in Figure 4.6, which are also collated in Table 4.1. Based on our model in Figure 4.6, the quantum yield for dissociation (ϕ_d) can be determined by the relative magnitudes of the rate constants for VET (k_{VET}) and dissociation (k_d), where the rate constant k is related to the lifetime τ through $k = 1/\tau$. Formally, $\phi_d = k_d / (k_d + k_{\text{VET}})$ and returns a value of $\phi_d = 0.89$ for the photodissociation of **1** in H₂O. Meanwhile, the remaining fraction of population ($\phi_{^3\text{MLCT}_{v=0}} = 1 - \phi_d$) will be funnelled into vibrationally cold $^3\text{MLCT}_{v=0}$. In deriving these values for ϕ_d and

Table 4.1 | Time constants (τ) and quantum yields (ϕ) extracted for the dissociation of **1**. Values for τ are extracted from kinetic fits to the traces in Figure 4.7, in accordance with the kinetic model presented in Figure 4.6. See main text for further details.

Parameter	Value
τ_d	0.4 ps
τ_{VET}	3.6 ps
τ_{GSR}	180 ps
τ_{GR}	263 ps
τ_s	377 ps
τ_{MA}	<1 ps
ϕ_d	0.89
$\phi_{3\text{MLCT}_{v=0}}$	0.11
ϕ_{GR}	0.53
ϕ_2	0.36
ϕ_1	0.64

$\phi_{3\text{MLCT}_{v=0}}$, an assumption is made that the timescale for VET remains constant for the duration of the vibrational cooling process in $^3\text{MLCT}$. However, this is an over simplification and, in reality, the initial VET rate around the hot $^3\text{MLCT}_{v>0}$ levels is likely to be much more rapid than the value for τ_{VET} reported in Table 4.1, due to the comparatively high density of vibrational levels and the smaller energy spacing (*cf.* closer to $^3\text{MLCT}_{v=0}$). As vibrational energy is quenched away from $^3\text{MLCT}_{v>0}$, relaxation will populate lower vibrational levels where the density of states is reduced and the inter-state spacing is increased, leading to a reduction in the VET rate as $^3\text{MLCT}_{v=0}$ is approached. VET out of these lower vibrational levels will therefore act as a rate-limiting step in vibrational cooling,^{29,32,33} and our value for τ_{VET} in H₂O most likely reflects these later stages of this process. Taking this into consideration, the value we extract for ϕ_d from this ‘zero-order’ model should be considered as an *absolute upper limit* for the fraction of population evolving towards dissociation. Even so, the value for ϕ_d derived here is still instructive and leads to a general conclusion that $\phi_d \geq \phi_{3\text{MLCT}_{v=0}}$ for **1** – such a conclusion is broadly supported by previous work on other related Ru(II) systems,^{11,23,34,35} which also suggest

ϕ_d will be large. Given this, it is striking that the relative intensity of the ³MLCT ESA features in the TAS are comparable to, or greater than, the spectral signature for the PCI complex formed through Ru–NA dissociation (*cf.* feature **i** vs. feature **iii** in Figure 4.3a). This generally suggests that the ESA cross-section from the ³MLCT state is significantly greater than the absorption cross-section of the PCI species. Similar findings can also be seen in the TAS for **1** in acetone (Figure 4.4), and are qualitatively supported by the predicted weak absorption intensity of the PCI complex at $\lambda > 550$ nm by the TD-B3LYP calculations in Figure 4.2c.

After dissociation, some fraction of the ‘caged’ PCI·NA pair will geminately reform **1** (ϕ_{GR}), the quantum yield for which is determined according to $\phi_{GR} = [k_{GR} / (k_{GR} + k_s)] \times \phi_d$. This returns a value of $\phi_{GR} = 0.53$. The remaining fraction of the PCI·NA pair will also undergo a degree of diffusional rearrangement into ‘separated’ PCI and NA. In H₂O, the portion of PCI·NA that diffusively separates will rapidly form **2**, with a quantum yield of $\phi_2 = 0.36$ (defined as $\phi_2 = \phi_d - \phi_{GR}$). Knowing this, and based on our above discussion that ϕ_d must be taken as an absolute upper limit, we can state more definitively that $0.36 \leq \phi_d \leq 0.89$ must be true. Consistent with ϕ_2 , the quantum yield for the ground state recovery of **1** (ϕ_1) will be defined as $\phi_1 = 1 - \phi_2 = \phi_{GR} + \phi_{3MLCTv=0} = 0.64$. These values for ϕ_1 and ϕ_2 are in excellent agreement with the percentage recovery of the GSB determined through our target analysis (see Figure 4.7d), which recovers by ~65 %. We draw attention to the fact that had ϕ_1 and ϕ_2 simply been estimated through inspection of the percentage recovery of GSB feature **ii** in the TAS in Figure 4.3b, the returned quantum yields would have been incorrect (*cf.* $\phi_2 \sim 0.1$), due to the strong spectral overlap of the signatures for **1** and **2** in the TAS. This emphasizes that, where possible, target analysis is a vital tool for extracting reliable kinetic information and quantum yields from UV/Vis TAS.

4.3.7. Formation and Relaxation Dynamics of the Intermediate [Ru(bpy)₂(NA)]²⁺

The methodologies used here are not sensitive to tracing the precise pathways for the formation of the ‘caged’ PCI·NA pair from the ³MLCT state of **1**, after flux leaves the vertical Franck-

Condon region. After population leaves the ³MLCT state, not only do we lose our optical handle on any population which may be transiently present in the ³MC surface (recall the discussion in Section 4.3.1), but identifying precise geometries where strong electronic state couplings occur along the Ru–NA dissociation coordinate with theoretical calculations, such as CASSCF methods, becomes problematic due to active space impurities incurred by mixing with the large number of near-degenerate states. However, the schematic potential energy profiles in Figure 4.9 depict a qualitative picture of the Ru–NA bond fission in **1**, and the involvement of the MLCT and MC states (based on earlier calculated potentials in related systems^{64,73}). Coupling between the ³MLCT state and the ³MC state most likely involves motion along anti-symmetric Ru–N stretch vibrations, which is then energetically stabilized by the distorted ³MC state

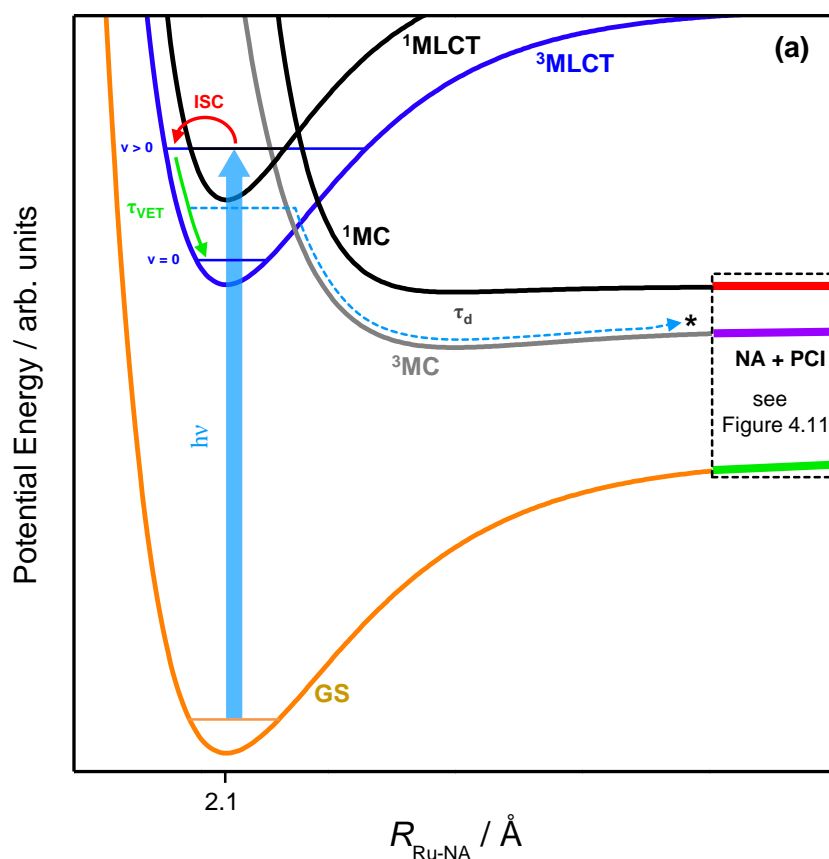


Figure 4.9 | Schematic potential energy profiles of the ¹MLCT, ³MLCT, ³MC, ¹MC and singlet ground state (GS) along the Ru–NA bond dissociation coordinate in **1**, including the major relaxation channels after excitation (*hν*) to the ‘bright’ ¹MLCT state.

geometry,³¹ as previously described for related complexes.³⁵ Moreover, our above kinetic analysis and quantum yields indicate very efficient mixing of the ³MLCT_{v>0} and ³MC states (*vide supra*), and find that crossing between these states must take place on a timescale of <400 fs (*cf.* τ_d in Table 4.1).

As with simpler d⁶ metal systems, the ³MC state, which involves a singly occupied 4d_{x²-y²} orbital (see Appendix Figure C.1c), will become strongly stabilised upon Ru–NA dissociation and at infinite separation will transform into the lowest energy excited ³MC state of the PCI complex – see Refs 36 and 37 for a more expanded discussion of this behaviour. In the immediate wake of NA loss from the ³MC state of **1**, the PCI complex present within the PCI·NA pair will therefore be formed in its lowest energy electronically excited ³MC state (involving singly occupied 4d_{x²-y²} and 4d_{yz} orbitals), consistent with the thesis in previous literature.³⁶⁻³⁹ Thus, in order to gain a greater understanding of how these electronically excited ³MC PCI species relax to their electronic ground state (GS) before generating **2**, we close by discussing the results of complementary CASSCF calculations aimed at identifying regions of strong electronic state coupling (either *via* internal conversion or ISC) within the excited state potential energy landscape of the PCI species.

These calculations locate a region in nuclear co-ordinate space for strong ISC between the electronically excited ³MC and ¹MC states (of the same character) in the PCI. The geometry presented in Figure 4.10a is a minimum energy crossing point (MECP) on the 3*N* – 7 (where *N* is the number of atoms)⁴⁰ dimensional seam of electronic state degeneracy⁴¹ between the ³MC and ¹MC surfaces (³MC/¹MC ISC seam), involving predominantly population of the 4d_{x²-y²} orbital. Due to the presence of a seam around the ISC minimum, ³MC → ¹MC population transfer *via* ISC is expected to be extremely efficient in the PCI. This MECP geometry has a combination of both trigonal bipyramid (TBP) and square pyramidal (SP) character around the Ru(II) metal centre, and also shows the vibrational motion responsible for lifting the degeneracy

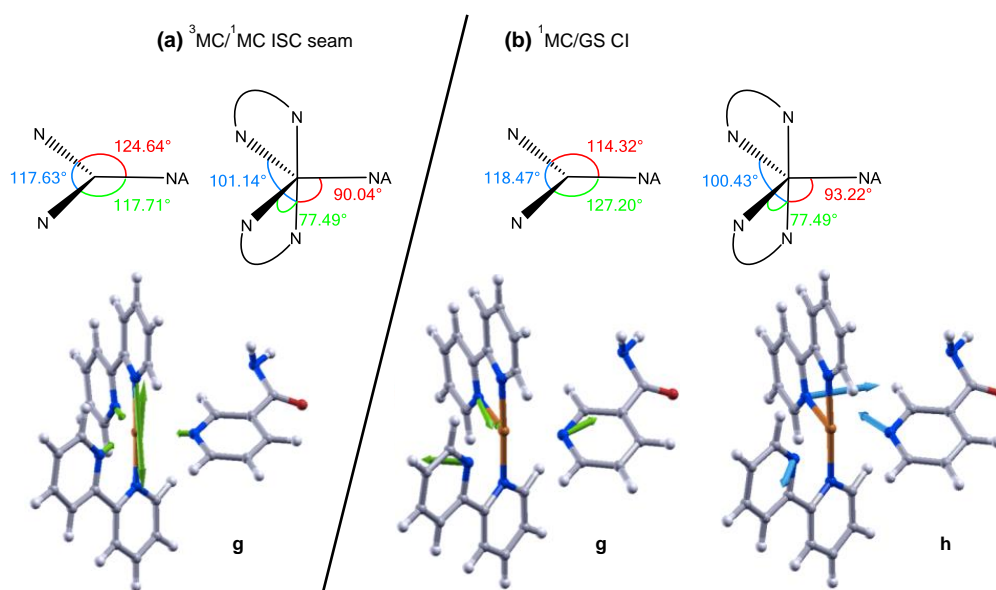


Figure 4.10 | (a) MECP of the CASSCF calculated ³MC/¹MC ISC seam. Equatorial and axial angles of this geometry as well as the gradient difference motion (**g**) are presented. (b) MECP of the CASSCF calculated ¹MC/GS CI, of quasi-JT type, and branching space. Equatorial and axial angles of this geometry as well as the gradient difference (**g**) and derivative coupling motions (**h**) are presented.

between the ³MC and ¹MC surfaces (labelled **g** in Figure 4.10a). This vibration corresponds to a contraction/expansion of all Ru–N bonds in the PCI, with the most pronounced motion lying along the axial Ru–N(bpy) coordinate.

Further to the ³MC/¹MC ISC seam, a conical intersection (CI)⁴¹ geometry, of *quasi*-TBP nature, subsequently connects the ¹MC surface with the electronic GS of the PCI, the calculated MECP of which is shown in Figure 4.10b (¹MC/GS CI). Minimal distortion away from the (higher energy) MECP geometry of ³MC/¹MC ISC seam is subsequently required to access the MECP geometry of the ¹MC/GS CI, which is *pseudo*-JT like due to the degeneracy imposed by partial occupancy of both the 4d_{xy} and 4d_{x²–y²} orbitals.⁴² As can be seen in Figure 4.10b, the MECP structure is ‘skewed’ from a pure TBP in that the axial-equatorial angles between bpy ligands differs from 90° with one angle at approximately 77°, and the other at approximately 100° – hence the structural designation of *quasi*-TBP. The equatorial-axial angle to the NA ligand is around 90°, and the equatorial-equatorial angles are all close to 120°. Further analysis of the

CASSCF calculations indicate that the topography of this ¹MC/GS CI is of ‘peaked’ type in the terminology of Ruedenberg and co-workers⁴³ (as one would anticipate for a *pseudo*-JT type CI⁴¹), and is calculated to lie around 0.5 eV below the MECP of the ³MC/¹MC ISC seam (see Figure 4.11). The two nuclear motions that remove the degeneracy between the ¹MC state and GS, termed the gradient difference (**g**) and derivative coupling (**h**), are also presented in Figure 4.10b, where the latter is typically responsible for enabling population transfer through the CI.⁴¹ Both of these motions lie in the equatorial plane, and evolution along a linear combination of these vibrational modes will lead to the creation of a PCI structure with an open coordination site on the electronic GS (*i.e.* *quasi*-SP). We note that the ¹MC/GS CI and associated connected minima identified in the PCI are very similar to those identified in related species (see, for example, Refs 44, 45 and 46), for both open- and closed-shell transition metal complexes, that undergo ligand photodissociation and subsequent non-adiabatic relaxation in their associated PCI complexes.

Depending on how population evolves through the ¹MC/GS CI, two different minima may be accessed on the electronic GS of the PCI, corresponding to two different structural isomers. The lowest energy of these GS isomers is calculated to be around 2.1 eV below the MECP of the ¹MC/GS CI. In Figure 4.11 this minimum is labelled *pro-cis*-PCI, together with its calculated structure, given that insertion of a H₂O solvent molecule into its free coordinate site will give rise to the *cis* isomer of **2**. Alternatively, rearrangement of the bpy ligands upon evolution through the CI could yield the *pro-trans*-PCI to enable subsequent formation of *trans*-**2** mono-aquated photoproducts; the *pro-trans*-PCI is calculated to lie ~0.4 eV above the *pro-cis*-PCI species using B3LYP/cc-pVTZ-SDD. Note that, isomerisation as a result of excited state PCI relaxation has been reported previously for other metal complexes.^{45,46} Here though, we only experimentally observe evidence for the formation of the *cis* isomer of **2**, suggesting that the *pro-trans*-PCI structure is never accessed. Unlike the *pro-cis*-PCI, the *pro-trans*-PCI clearly exhibits much greater deviation from a true SP geometry due to steric distortion of the two bpy

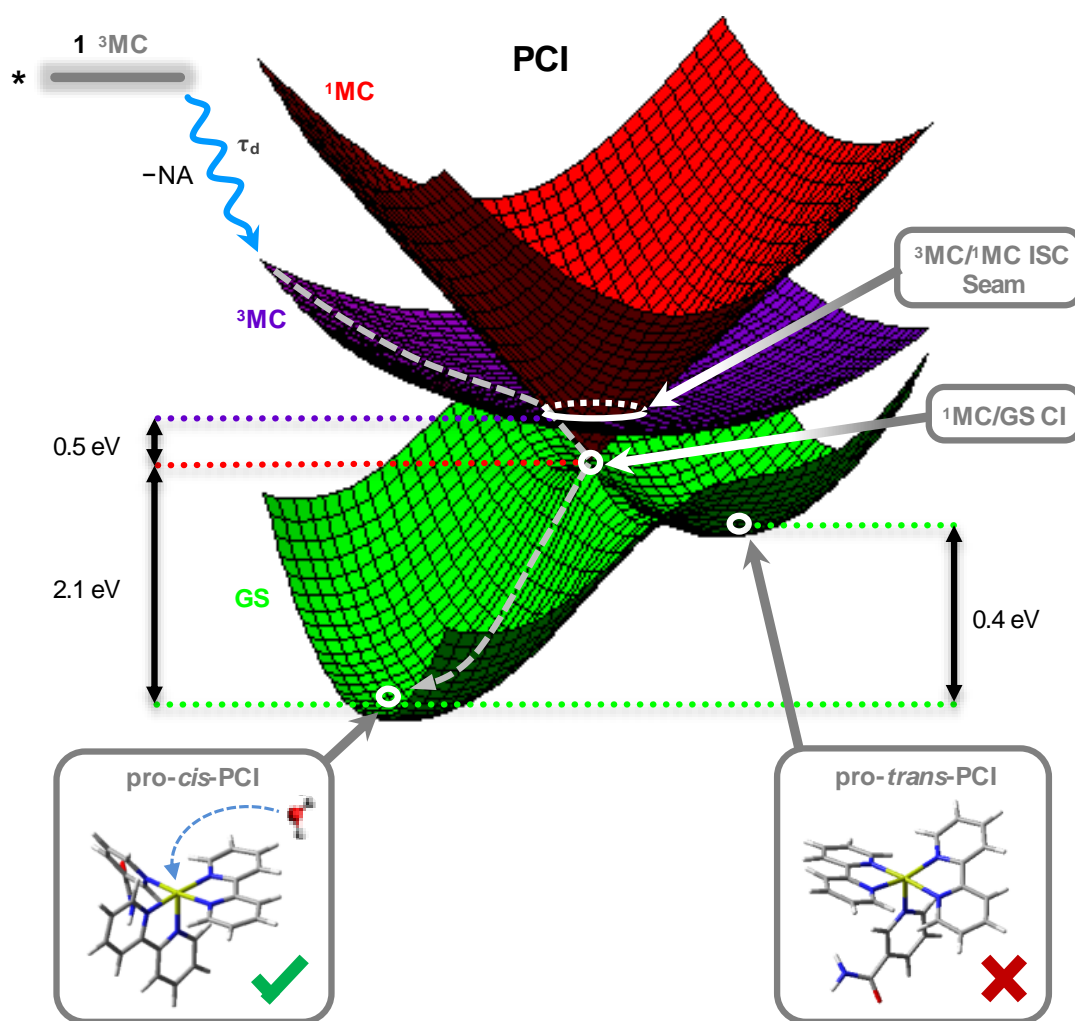


Figure 4.11 | Schematic potential energy surfaces for the significant electronic states in the PCI complex. From the top left, downwards: excited state population from the ³MC of **1** (black) may land on the ³MC PCI (purple) following NA ligand elimination; displacement through the ³MC/¹MC ISC seam minimum (Figure 4.10a) to the ¹MC PCI (red); and then through the ¹MC/GS CI minimum (Figure 4.10b) leading to the GS of the PCI (green). On the GS, two possible isomers of PCI exist, labelled pro-*cis* and pro-*trans*, into which a solvent molecule may be accommodated to complete the formation of **2**.

ligands induced by the adjacent NA (see structures in Figure 4.11), hence why the pro-*cis*-PCI lies lower in energy. This may be a contributing factor in the sole formation of pro-*cis*-PCI. Perhaps more importantly though, the electronic state relaxation of the PCI will occur within the ‘caged’ PCI·NA pair, and the close proximity of the neighbouring NA partner will aid to prevent isomerisation to the pro-*trans*-PCI structure on steric grounds as flux relaxes through the ¹MC/GS CI.

The electronic state relaxation scheme presented for the PCI complex from these CASSCF calculations implies that during this process, a structural evolution from *quasi*-SP \rightarrow *quasi*-TBP \rightarrow *quasi*-SP must occur. Following dissociation in simpler systems, this rearrangement process was observed to be ultrafast (sub-200 fs).^{37,39} This is also likely to be the case here, meaning that any spectral signature for this process will be too fast to observe in our current TAS measurements. However, after relaxation to the GS, the nascent pro-*cis*-PCI will necessarily be formed vibrationally hot. Experimentally, we noted in Section 4.3.2 that the early time TAS in Figure 4.3a ($t < 25$ ps) display some rapid depletion of the PCI feature **iii**, on the order of ~ 10 ps. These earlier time dynamics may, in part, be due to relaxation of a vibrationally hot pro-*cis*-PCI in the GS, undergoing vibrational cooling through VET to the solvent.²⁹ Therefore, our combined experimental and computational findings lead us to broadly conclude that after Ru–NA bond fission in **1**, electronically excited PCI complexes in the nascent PCI·NA pair can relax *via* an efficient sequential $^3\text{MC} \rightarrow ^1\text{MC} \rightarrow \text{GS}$ coupling process, mediated by appropriate $^3\text{MC}/^1\text{MC}$ ISC and $^1\text{MC}/\text{GS}$ CI seams, on a sub-500 fs timescale, followed by vibrational relaxation of the pro-*cis*-PCI on the order of ≤ 10 ps, after which diffusional separation can occur and enable the formation of photoproduct **2**.

4.4. Conclusions

One of the primary aims of the study presented here has been to increase our understanding of the key mechanistic pathways of photoactivation of a potential prodrug. Specifically, a synergy between experiment and theory has revealed that *cis*-[Ru(bpy)₂(NA)₂]²⁺ (**1**) has several efficient excited state pathways that are pivotal in the control of the branched kinetics that ultimately dictate the quantum yield for forming the reactive photoproduct, [Ru(bpy)₂(NA)(H₂O)]²⁺ (**2**). The ability of target analysis to decipher accurate timescales and quantum yields from congested transient absorption spectra is critical to these investigations. In identifying these important ‘crossroads’, we can propose the following arguments, which afford the relatively high reported quantum yield of **2**, $\phi_2 = 0.36$: (i) complete conversion of the initial excited

¹MLCT state population to the vibrationally excited ³MLCT with a lifetime of <100 fs; (ii) efficient traversal of flux from the vibrationally excited ³MLCT state to the dissociative ³MC state, and subsequent dissociation with the quantum yield $0.36 \leq \phi_d \leq 0.89$, occurs on a <400 fs timescale; (iii) the nascent photodetached ligand may be viewed as part of a ‘caged’ product pair within the solvation shell, PCI·NA; and (iv) the nascent PCI·NA pair may either geminately reform **1** or undergo a degree of diffusional separation, both of which are kinetically competitive processes, where the later subsequently enables ultrafast (sub-1 ps) solvent substitution to finally form **2**.

The results presented here provide an excellent basis for understanding the initial stages involved in photoactivation of potential metal complex prodrugs and how we can tailor molecular properties to improve their performance. One clear notion is that bulkier ligands will suffer severe caging in the immediate wake of dissociation, which will, in turn, significantly dictate the formation of the target species **2**. The quantum yield for forming the target product will ultimately be governed by a combination of (i) the quantum yield for dissociation and (ii) the relative rates of diffusive separation versus geminate recombination for the nascent caged product pair.

4.5. Bibliography

- (1) Bruijninx, P. C. A.; Sadler, P. J. *Curr. Opin. Chem. Biol.* **2008**, *12*, 197.
- (2) Kelly, J. M.; McConnell, D. J.; OhUigin, C.; Tossi, A. B.; Mesmaeker, A. K.-D.; Masschelein, A.; Nasielski, J. J. *Chem. Soc., Chem. Commun.* **1987**, 1821.
- (3) Novakova, O.; Kasparkova, J.; Vrana, O.; van Vliet, P. M.; Reedijk, J.; Brabec, V. *Biochemistry* **1995**, *34*, 12369.
- (4) Singh, T. N.; Turro, C. *Inorg. Chem.* **2004**, *43*, 7260.
- (5) Wachter, E.; Heidary, D. K.; Howerton, B. S.; Parkin, S.; Glazer, E. C. *Chem. Commun.* **2012**, *48*, 9649.
- (6) Gill, M. R.; Thomas, J. A. *Chem. Soc. Rev.* **2012**, *41*, 3179.
- (7) Howerton, B. S.; Heidary, D. K.; Glazer, E. C. *J. Am. Chem. Soc.* **2012**, *134*, 8324.
- (8) Sun, Y.; Joyce, L. E.; Dickson, N. M.; Turro, C. *Chem. Commun.* **2010**, *46*, 2426.

-
- (9) Salassa, L.; Ruiu, T.; Garino, C.; Pizarro, A. M.; Bardelli, F.; Gianolio, D.; Westendorf, A.; Bednarski, P. J.; Lamberti, C.; Gobetto, R.; Sadler, P. J. *Organometallics* **2010**, *29*, 6703.
- (10) Pinnick, D. V.; Durham, B. *Inorg. Chem.* **1984**, *23*, 1440.
- (11) Liu, Y.; Turner, D. B.; Singh, T. N.; Angeles-Boza, A. M.; Chouai, A.; Dunbar, K. R.; Turro, C. *J. Am. Chem. Soc.* **2009**, *131*, 26.
- (12) Bo, C.; Maseras, F. *Dalton Trans.* **2008**, 2911.
- (13) Wang, L.-P.; Van Voorhis, T. *J. Chem. Theory Comput.* **2012**, *8*, 610.
- (14) Bhasikuttan, A. C.; Suzuki, M.; Nakashima, S.; Okada, T. *J. Am. Chem. Soc.* **2002**, *124*, 8398.
- (15) Yoon, S.; Kukura, P.; Stuart, C. M.; Mathies, R. A. *Mol. Phys.* **2006**, *104*, 1275.
- (16) Cannizzo, A.; van Mourik, F.; Gawelda, W.; Zgrablic, G.; Bressler, C.; Chergui, M. *Angew. Chem., Int. Ed.* **2006**, *45*, 3174.
- (17) Damrauer, N. H.; Cerullo, G.; Yeh, A.; Boussie, T. R.; Shank, C. V.; McCusker, J. K. *Science* **1997**, *275*, 54.
- (18) Damrauer, N. H.; McCusker, J. K. *J. Phys. Chem. A* **1999**, *103*, 8440.
- (19) Heath, G. A.; Yellowlees, L. J.; Braterman, P. S. *J. Chem. Soc., Chem. Commun.* **1981**, 287.
- (20) McCusker, J. K. *Acc. Chem. Res.* **2003**, *36*, 876.
- (21) For related complexes in refs 18 to 20 oxidation of Ru(II) to Ru(III) adds a red shift of the first MLCT of ~50 nm.
- (22) Sun, Q.; Mosquera-Vazquez, S.; Lawson Daku, L. M.; Guénée, L.; Goodwin, H. A.; Vauthey, E.; Hauser, A. *J. Am. Chem. Soc.* **2013**, *135*, 13660.
- (23) Salassa, L.; Garino, C.; Salassa, G.; Gobetto, R.; Nervi, C. *J. Am. Chem. Soc.* **2008**, *130*, 9590.
- (24) Grubb, M. P.; Orr-Ewing, A. J.; Ashfold, M. N. *Rev. Sci. Instrum.* **2014**, *85*, 064104.
- (25) Mckinlay, R. G.; Žurek, J. M.; Paterson, M. J. *Adv. Inorg. Chem.* **2010**, *62*, 351.
- (26) Demas, J. N.; Taylor, D. G. *Inorg. Chem.* **1979**, *18*, 3177.
- (27) Wallin, S.; Davidsson, J.; Modin, J.; Hammarström, L. *J. Phys. Chem. A* **2005**, *109*, 4697.
- (28) Henry, W.; Coates, C. G.; Brady, C.; Ronayne, K. L.; Matousek, P.; Towrie, M.; Botchway, S. W.; Parker, A. W.; Vos, J. G.; Browne, W. R.; McGarvey, J. J. *J. Phys. Chem. A* **2008**, *112*, 4537.
- (29) Owrutsky, J. C.; Raftery, D.; Hochstrasser, R. M. *Annu. Rev. Phys. Chem.* **1994**, *45*, 519.
- (30) Durham, B.; Caspar, J. V.; Nagle, J. K.; Meyer, T. J. *J. Am. Chem. Soc.* **1982**, *104*, 4803.
- (31) Juris, A.; Balzani, V.; Barigelletti, F.; Campagna, S.; Belser, P.; von Zelewsky, A. *Coord. Chem. Rev.* **1988**, *84*, 85.
-

- (32) Harris, S. J.; Murdock, D.; Zhang, Y.; Oliver, T. A. A.; Grubb, M. P.; Orr-Ewing, A. J.; Greetham, G. M.; Clark, I. P.; Towrie, M.; Bradforth, S. E.; Ashfold, M. N. R. *Phys. Chem. Chem. Phys.* **2013**, *15*, 6567.
- (33) Karsili, T. N. V.; Wenge, A. M.; Harris, S. J.; Murdock, D.; Harvey, J. N.; Dixon, R. N.; Ashfold, M. N. R. *Chem. Sci.* **2013**, *4*, 2434.
- (34) Salassa, L.; Borfecchia, E.; Ruiiu, T.; Garino, C.; Gianolio, D.; Gobetto, R.; Sadler, P. J.; Cammarata, M.; Wulff, M.; Lamberti, C. *Inorg. Chem.* **2010**, *49*, 11240.
- (35) Borfecchia, E.; Garino, C.; Salassa, L.; Ruiiu, T.; Gianolio, D.; Zhang, X.; Attenkofer, K.; Chen, L. X.; Gobetto, R.; Sadler, P. J.; Lamberti, C. *Dalton Trans.* **2013**, *42*, 6564.
- (36) Pollak, C.; Rosa, A.; Baerends, E. J. *J. Am. Chem. Soc.* **1997**, *119*, 7324.
- (37) Paterson, M. J.; Hunt, P. A.; Robb, M. A.; Takahashi, O. *J. Phys. Chem. A* **2002**, *106*, 10494.
- (38) Burdett, J. K.; Grzybowski, J. M.; Perutz, R. N.; Poliakoff, M.; Turner, J. J.; Turner, R. F. *Inorg. Chem.* **1978**, *17*, 147.
- (39) Trushin, S. A.; Fuss, W.; Schmid, W. E.; Kompa, K. L. *J. Phys. Chem. A* **1998**, *102*, 4129.
- (40) Two surfaces of the same spin intersect in a space of dimension 3N-8, with the gradient difference and derivative coupling vectors lifting the degeneracy at first order. By symmetry the derivative coupling is the zero vector if the states have different symmetries.
- (41) Yarkony, D. R. *Rev. Mod. Phys.* **1996**, *68*, 985.
- (42) McKinlay, R. G.; Paterson, M. J. In *The Jahn-Teller Effect*; Köppel, H., Yarkony, D. R., Barentzen, H., Eds.; Springer Berlin Heidelberg: 2009; Vol. 97, p 311.
- (43) Atchity, G. J.; Xantheas, S. S.; Ruedenberg, K. *J. Chem. Phys.* **1991**, *95*, 1862.
- (44) Paterson, M. J.; Blancafort, L.; Wilsey, S.; Robb, M. A. *J. Phys. Chem. A* **2002**, *106*, 11431.
- (45) Żurek, J. M.; Paterson, M. J. *J. Phys. Chem. A* **2012**, *116*, 5375.
- (46) Żurek, J. M.; Paterson, M. J. *J. Chem. Phys.* **2012**, *137*, 034308.

*“Just dust and echoes. We’re
all that’s left... Halo. It’s
finished”*

– Cortana

– Cortana



5.1. Summary

This thesis documents the implementation of a transient absorption spectrometer to study photodissociation reactions in solution. On the face of it, it may seem that the two areas of study presented in this thesis: photostability of biomolecules and photoactivation of transition metal complexes, are two divorced fields. The premise that biologically important molecules must resist photodegradation in order to prevent harmful cellular reactions is antithetical to the activation method for photochemotherapy. Since the majority of small biological motif studies, *e.g.* phenols, indicate that $\pi\sigma^*$ photodissociation pathways are active, the knowledge base of such mechanisms has become significant. In understanding how these deactivation modes may be shut off – as seen for guaiacol in Chapter 3 through solvent choice – we may apply this perspicacity toward enhancing photodissociation when it is desired.

The first chapter provided a crash course in photophysics and femtochemistry. It was by no means comprehensive but covered the fundamental concepts seen in the ensuing results chapters. The technique of transient absorption spectroscopy was discussed in detail. An overview of photostability of biologically relevant molecules was provided, focussing on studies of phenol since this is the most pertinent to Chapter 3, due its structural likeness to guaiacol, and seen as an archetype for $\pi\sigma^*$ photodissociation that has gained myriad attention from gas- and (to a lesser extent) solution-phase spectroscopists.

Chapter 2 documented the construction and optimisation of the transient absorption spectrometer. An important part of this section is the description of the gravity driven thin-film liquid jet, which may prove useful to spectroscopists seeking to remove sample/glass interaction or maximise their temporal resolution. The purpose coded LabVIEW programme (which was not documented here) has been a significant part of the development of this spectrometer.

In Chapter 3 we demonstrated that we are able to track conformer-specific photodissociation dynamics in solution through solvent choice. We revealed this phenomenon in guaiacol (2-

methoxyphenol), a key subunit of the natural biopolymer lignin. In cyclohexane, the first electronically excited $^1\pi\pi^*$ (S_1) state in guaiacol relaxes with a time-constant of $\tau = 4.5 \pm 0.2$ ns, mediated through intersystem crossing to lower lying triplet (T_n) states and internal conversion and fluorescence back to ground electronic state (S_0). In contrast, in methanol, a fourth relaxation channel is also present; the S_1 state relaxes with a time-constant of $\tau = 2.9 \pm 0.1$ ns, which is now additionally mediated through coupling onto a dissociative $^1\pi\sigma^*$ (S_2) state and subsequent O–H bond fission, evidenced through the appearance of a spectral signature for the guaiacoxyl radical after ~ 250 ps. With aid of complementary calculations, we attributed this to the now absent intramolecular H-bond between OH and OMe moieties, which now favours intermolecular H-bonding to methanol, lowering the barrier to O–H dissociation and facilitating H-atom loss via tunnelling.

Chapter 4 provided mechanistic insight into the photo-induced solvolysis of *cis*-[Ru(bipyridine)₂(nicotinamide)₂]²⁺ (**1**). Complex **1** is a photoactive species, designed to display high cytotoxicity following irradiation, for potential use in photodynamic therapy (photochemotherapy). In Ru(II) complexes of this type, efficient population of a dissociative triplet metal-centred (3MC) state is key to generating high quantum yields of a pentacoordinate intermediary (PCI) species, which in turn may form the target species: a mono-aqua photoproduct [Ru(bipyridine)₂(nicotinamide)(H₂O)]²⁺ (**2**). Following irradiation of **1**, a thorough kinetic picture was derived from ultrafast UV/Vis transient absorption spectroscopy measurements, using a ‘target analysis’ approach, and provided both timescales and quantum yields for the key processes involved. We showed that photoactivation of **1** to **2** occurs with a quantum yield ≥ 0.36 , all within a timeframe of ~ 400 ps. Characterization of the excited states involved, particularly the nature of the PCI and how it undergoes a geometry relaxation to accommodate the water ligand, which is a keystone in the efficacy of the photoactivation of **1**, was accomplished through state-of-the-art computation including complete active space self-consistent field methods and time-dependent density functional theory. Importantly, the

conclusions here provided a detailed understanding of the initial stages involved in this photoactivation and the foundation required for designing more efficacious photochemotherapy drugs of this type.

5.2. Outlook

5.2.1. Photostability in Biomolecules

The work here on guaiacol lends toward the ‘bottom-up’ approach that has been employed in gas-phase studies on dynamics of molecules that have biological importance.^{1,2} Within this idea of ‘bottom-up’ spectroscopy, there is a hierarchy of system complexity in which biological chromophores may be regarded as the ground level; substituted chromophores as the first step up; and many levels later, full systems, such as protein structures or tissues, taking the top step. As an example, much of the gas-phase work conducted on substituted phenols³⁻¹⁰ may be regarded as first step work, and adding solution adds a further level of complexity. Given the differences observed due to substitution or solvation and new gas-phase techniques,² which allow the study of larger molecules *in vacuo*, it is clear that this is a fertile area of study.

The immediate aim for expansion upon this study of guaiacol is gas-/solution-phase comparative studies of similarly substituted phenols. Then, the way in which solvent changes the dynamics must be explored further; it is known that solvent affects potential energy surfaces but is this attributable to solvent H-bonding or solvent polarity or a combination? Studies of particular motifs in ranges of solution environments will broaden this understanding.

5.2.2. Photoactivation of Transition Metal Complexes

The work here on $[\text{Ru}(\text{bpy})_2(\text{NA})_2]^{2+}$ serves to highlight the significance of *structure-dynamics-function* relationships, with particular emphasis here, on the design of more efficacious photochemotherapeutic agents. Many avenues of study remain in the development of these potential prodrugs. Firstly it is apparent from this study that the degree of solvent caging must be further investigated. Whilst it sounds inviting to use a bifurcated method of attack, in which

the photoactivated complex has a reactive core, *i.e.* a solvated Ru complex, and releases bioactive ligands (caged delivery), it may be that by adding a large bioactive leaving group, L, the lowered quantum yield of activation becomes detrimental to the overall efficacy. For complexes of the type $[\text{Ru}(\text{bpy})_2(\text{L}')(\text{L}'')]^{2+}$ we may complete similar TA studies to evaluate the relation of the size of L with activation quantum yield.

A second important task to address is the method of activation. The ‘photodynamic window’ is a region in the electromagnetic spectrum, where the transmission through biological tissue is highest, and covers the range of 650 to 850 nm.¹¹ Whilst the single photon absorption cross-sections of transition metal complexes in the UV/blue visible region are sizable, they do not absorb strongly in the red and near-infrared regions, *e.g.* $[\text{Ru}(\text{bpy})_2(\text{NA})_2]^{2+}$ has a visible absorption maximum at 445 nm and no absorption >650 nm. While redesign of the complex may aid in the red shifting of the absorption spectra; swapping bpy for alternative bidentate type ligands, such as 1,10-phenanthroline or 2,2'-biquinoline¹², this method may alter the energies of key electronic states and significantly decrease the activation quantum yield.

Another approach is to use two-photon absorption induced activation. Two-photon absorption has the advantages of higher tissue penetration depth¹³ and access to the excited states of several transition metal complexes within the therapeutic window. For example, a square-planar platinum(II) complex with derivatized pyridine ligands was shown to undergo two-photon-induced ligand substitution with 600–740 nm light¹⁴ with much of the insight into the activation pathway revealed through theory. It is hoped that two-photon excitation TA studies of photoactive complexes will contribute to the understanding of the dynamics involved and explore this avenue further.

5.3. Bibliography

- (1) Roberts, G. M.; Stavros, V. G. *Chem. Sci.* **2014**, 5, 1698.
- (2) Staniforth, M.; Stavros, V. G. *Proc. R. Soc. A* **2013**, 469, 20130458.

- (3) Karsili, T. N. V.; Wenge, A. M.; Harris, S. J.; Murdock, D.; Harvey, J. N.; Dixon, R. N.; Ashfold, M. N. R. *Chem. Sci.* **2013**, *4*, 2434.
- (4) Karsili, T. N. V.; Wenge, A. M.; Marchetti, B.; Ashfold, M. N. R. *Phys. Chem. Chem. Phys.* **2014**, *16*, 588.
- (5) Livingstone, R. A.; Thompson, J. O. F.; Iljina, M.; Donaldson, R. J.; Sussman, B. J.; Paterson, M. J.; Townsend, D. *J. Chem. Phys.* **2012**, *137*, 184304.
- (6) Dixon, R. N.; Oliver, T. A. A.; Ashfold, M. N. R. *J. Chem. Phys.* **2011**, *134*, 194303.
- (7) Chatterley, A. S.; Young, J. D.; Townsend, D.; Żurek, J. M.; Paterson, M. J.; Roberts, G. M.; Stavros, V. G. *Phys. Chem. Chem. Phys.* **2013**, *15*, 6879.
- (8) King, G. A.; Oliver, T. A. A.; Dixon, R. N.; Ashfold, M. N. R. *Phys. Chem. Chem. Phys.* **2012**, *14*, 3338.
- (9) Young, J. D.; Staniforth, M.; Dean, J. C.; Roberts, G. M.; Mazzoni, F.; Karsili, T. N. V.; Ashfold, M. N. R.; Zwier, T. S.; Stavros, V. G. *J. Phys. Chem. Lett.* **2014**, *5*, 2138.
- (10) Hadden, D. J.; Roberts, G. M.; Karsili, T. N. V.; Ashfold, M. N. R.; Stavros, V. G. *Phys. Chem. Chem. Phys.* **2012**, *14*, 13415.
- (11) Moser, J. G. *Photodynamic Tumor Therapy* **1998**, 1.
- (12) Wachter, E.; Heidary, D. K.; Howerton, B. S.; Parkin, S.; Glazer, E. C. *Chem. Commun.* **2012**, *48*, 9649.
- (13) Wang, X.-Q.; Chen, J.-Y.; Mi, L.; Wang, P.-N. *Appl. Phys. Lett.* **2009**, 95.
- (14) Zhao, Y.; Roberts, G. M.; Greenough, S. E.; Farrer, N. J.; Paterson, M. J.; Powell, W. H.; Stavros, V. G.; Sadler, P. J. *Angew. Chem., Int. Ed.* **2012**, *51*, 11263.

Appendix A: List of Abbreviations

BBO	β -barium borate
bpy	2,2'-bipyridine
BS	beam splitter
CASSCF.....	complete active space self-consistent field
CCD	charge-couple device
CI	conical intersection
CT	charge transfer
DCM	4-(dicyanomethylene)-2-methyl-6-(4-dimethylaminostyryl)-4H-pyran
DFG	difference frequency generation
DFT	density functional theory
DR.....	diffusive recombination
eBE	electron binding energy
ECP	effective core potential
ESA.....	excited state absorption
F.....	filter
FWHM.....	full width at half maximum
GR.....	geminate recombination
GSB.....	ground state bleach
GSR.....	ground state recovery
GVD.....	group velocity dispersion
HOMO	highest occupied molecular orbital
IC	internal conversion
ID.....	internal diameter
IET.....	intermolecular energy transfer
IR.....	infrared
IRF.....	instrument response function
ISC.....	intersystem crossing
IVR	intramolecular vibrational energy redistribution
JT.....	Jahn-Teller
L.....	lens (Chapter 2) or leaving group (elsewhere)
LUMO	lowest unoccupied molecular orbital
MA	mono-aquation
MC	metal-centred
MCP.....	multichannel plate
MECP	minimum energy crossing point
MLCT	metal-to-ligand charge transfer
NA.....	pyridine-3-carboxamide (nicotinamide)
ND.....	neutral density
OPA	optical parametric amplifier
OPG.....	optical parametric generation

OD	optical density or outer diameter
PCI.....	pentacoordinate intermediate
PCM.....	polarizable continuum model
PDT	photodynamic therapy
PEC	potential energy cuts
PES.....	potential energy surface
py	pyridine
RMS.....	root mean square
RR.....	retroreflector
SCG.....	supercontinuum generation
SFG.....	sum frequency generation
SHG	second harmonic generation
SM.....	spherical mirror
SP.....	square pyramid
TA.....	transient absorption
TAS.....	transient absorption spectrum (spectra)
TBP	trigonal bipyramid
TD.....	time-dependent
TDM	transition dipole moment
TRPEL.....	time-resolved photoelectron imaging
UV.....	ultraviolet
UV/Vis.....	ultraviolet/visible
VET	vibrational energy transfer
WKB.....	Wentzel-Kramers-Brillouin
WLC	white light continuum
ZPE.....	zero-point energy
$\lambda/2$ WP	half-wave plate

Appendix B: Chapter 3 Methodology

Gas Phase Methods

2-methoxyphenol (98%, Sigma-Aldrich) was placed in a cartridge mounted within the body of an Even-Lavie pulsed valve¹ and introduced into the spectrometer using helium (3 bar) as a carrier gas. The valve temperature was regulated at 60 °C. After passing into the main interaction chamber the molecular beam was intersected by co-propagating UV pump and probe pulses produced from the fundamental output of a 1 kHz Ti:Sapphire laser system (Spectra-Physics, Spitfire XP). The pump beam (267 nm, 0.1 μ J/pulse) was provided by the third harmonic of this output. The probe beam (305 nm, 0.9 μ J/pulse) was generated by twice frequency doubling the signal beam output from an optical parametric amplifier (Spectra Physics, OPA-800C). Thin BBO crystals were used as the non-linear medium. Pump-probe temporal delay was controlled using a linear translation stage running under PC control. The two beams were combined on a dichroic mirror and focussed into the spectrometer using a 25 cm fused silica lens.

Pump-probe ionisation of the sample took place between the electrodes of an electrostatic lens set-up optimised for velocity-map imaging.² A 40 mm MCP/P47 phosphor screen detector was used in conjunction with a CCD camera (640 \times 480 pixels) to image the resulting photoelectrons. A pump-probe cross correlation of 160 ± 20 fs was obtained directly from non-resonant ($1 + 1'$) ionisation of pyrrole and energy calibration data was obtained from three-photon, non-resonant ionisation of xenon. Pump-probe delays between -500 fs and $+500$ fs were sampled in 50 fs increments with a further 20 exponentially increasing steps taken out to $+100$ ps. At each repeatedly sampled delay position, pump alone and probe alone images were also recorded for background subtraction.

Theoretical Calculations

Using the MolPro 2010.1 computational package³ the minimum energy geometry of the ground state guaiacol molecule was optimised using complete active space self-consistent field (SA4-CASSCF) coupled with a contracted aug-cc-pVTZ basis set. Extra sets of even tempered *s* and *p* diffuse functions were added to the oxygen atoms (ratio=2) in order to describe the Rydberg-valence coupling more effectively. The choice of active space was heavily dependent on the O-Me and O-H ring substituents and after careful testing, an optimal active space of 12 electrons in 11 orbitals was chosen as a compromise between accuracy and computational expense. These orbitals comprised the three π bonding and three π^* anti-bonding Hückel type orbitals centred on the phenyl moiety, the p_x lone pair centred on the oxygen atoms of the O-Me and O-H groups, the σ and σ^* orbitals centred around the O-H moiety and the 3*s* Rydberg orbital centred on the oxygen atom of the O-H group.

Unrelaxed (rigid body) potential energy scans were then computed along the O-H bond extension coordinate ($R_{\text{O-H}}$) using the same basis set as above, but with the more accurate method: complete active space with second order perturbation theory (CASPT2). These CASPT2 calculations were based on a SA4-CASSCF reference wavefunction for both the **A** and **B** conformations and utilised the same active space as that used for the CASSCF calculations. Since the ground state optimised geometry favours the syn conformation, all other internal degrees of freedom were fixed during the scan along $R_{\text{O-H}}$. The PE scans for the **B** conformer, along $R_{\text{O-H}}$, required a 180° rotation of the CCOH dihedral, after which the potential energy was calculated as a function of O-H bond stretch in the normal way with all other internal degrees of freedom fixed at the ground state CASSCF geometry.

Bibliography

- (1) Even, U.; Jortner, J.; Noy, D.; Lavie, N.; Cossart-Magos, C. *J. Chem. Phys.* **2000**, *112*, 8068.
- (2) Eppink, A. T. J. B.; Parker, D. H. *Rev. Sci. Instrum.* **1997**, *68*, 3477.
- (3) Werner, H. J.; Knowles, P. J.; Knizia, G.; Manby, F. R.; Schütz, M.; Celani, P.; Korona, T.; Lindh, R.; Mitrushenkov, A.; Rauhut, G.; Shamasundar, K. R.; Adler, T. B.; Amos, R. D.; Bernhardsson, A.; Berning, A.; Cooper, D. L.; Deegan, M. J. O.; Dobbyn, A. J.; Eckert, F.; Goll, E.; Hampel, C.; Hesselmann, A.; Hetzer, G.; Hrenar, T.; Jansen, G.; Köppl, C.; Liu, Y.; Lloyd, A. W.; Mata, R. A.; May, A. J.; McNicholas, S. J.; Meyer, W.; Mura, M. E.; Nicklass, A.; O'Neill, D. P.; Palmieri, P.; Pflüger, K.; Pitzer, R.; Reiher, M.; Shiozaki, T.; Stoll, H.; Stone, A. J.; Tarroni, R.; Thorsteinsson, T.; Wang, M.; Wolf, A. *MOLPRO, version 2010.1, a package of ab initio programs* **2010**.

Appendix C: Chapter 4 Theory

Computational Methodology

The ground state geometries of complexes **1**, **2** and the $[\text{Ru}(\text{bpy})_2(\text{NA})]^{2+}$ PCI were optimized using density functional theory (DFT). Analytical Hessian evaluation confirmed the nature of the optimized geometries as minima. Several different functionals and basis sets were compared (PBE0,¹ M06L,² CAM-B3LYP³ and B3LYP^{4,5}). In particular, regarding basis sets the use of non-, quasi-, and fully relativistic effective core potentials (ECPs) was investigated in conjunction with the cc-pVTZ valence basis on the metal and non-metals, respectively.⁶ It was found that such basis set effects on geometry and electronic spectroscopy were relatively minor compared to the choice of functional. As such, a non-relativistic SDD 28 electron ($1s^2 2s^2 2p^6 3s^2 3p^6 3d^{10}$) ECP was used for the Ru centre, while the cc-pVTZ basis set⁷ was selected for the remaining C, N, O and H atoms. The electronic spectroscopy (singlet and triplet excitations) of **1**, **2** and the PCI was subsequently modelled with time-dependent density functional theory (TD-DFT), using the same basis set. For the functional, by far the best comparison with experimental UV/Vis spectra was found to be the B3LYP functional. A polarizable continuum model (PCM) was used to model the effects of solvation in H_2O .

To investigate the excited state reaction pathways in the PCI species, which determine the subsequent relaxation mechanism following light absorption, complete active space self-consistent field (CASSCF) calculations were performed. An active space was chosen consisting of the five 4d orbitals of the Ru centre, plus a corresponding set with an extra radial node in the Ru–N internuclear region to allow for dynamic electron correlation in the dative bonds.⁸⁻¹⁰ Alternative schemes including quasi-natural orbital approaches, such as those discussed in Refs 11 and 12, were also performed at selected geometries to ensure the active space description was balanced and stable. Generally, these two schemes gave very similar results although the quasi-natural orbital approach was more problematic both in terms of convergence and

characterization of the metal centred components, due to initial strong orbital mixing. Given the size of the systems under investigation, and the associated computational expense, the basis sets used for CASSCF calculations were a non-relativistic SDD 28 electron ($1s^2 2s^2 2p^6 3s^2 3p^6 3d^{10}$) ECP basis for the ruthenium; the 4-31G basis for carbon, oxygen, and nitrogen; and the STO-3G basis for hydrogen. This basis was calibrated (at the ground state geometry of the PCI) against a larger basis consisting of the same metal centred part, plus the 6-31G(d) basis for the non-metals. Geometrical effects in using the larger basis were very small. For calculations in the singlet and triplet manifolds many-electron configuration state function (CSF) bases were used, corresponding to $\langle \hat{S}_z \rangle = 0, \langle \hat{S}^2 \rangle = 0$ and $\langle \hat{S}_z \rangle = 1, \langle \hat{S}^2 \rangle = 2$, respectively. For calculations of singlet/triplet interactions a Slater determinant many-electron basis with $\langle \hat{S}_z \rangle = 0$ was used. The orbital rotation derivatives were neglected in solving the coupled-perturbed multi-configurational self-consistent field (MCSCF) equations in geometry optimizations involving state-averaged orbitals. Gaussian09¹³ was used for DFT and TD-DFT calculations, while Gaussian03¹⁴ was used for CASSCF calculations.

TD-B3LYP Calculation Results

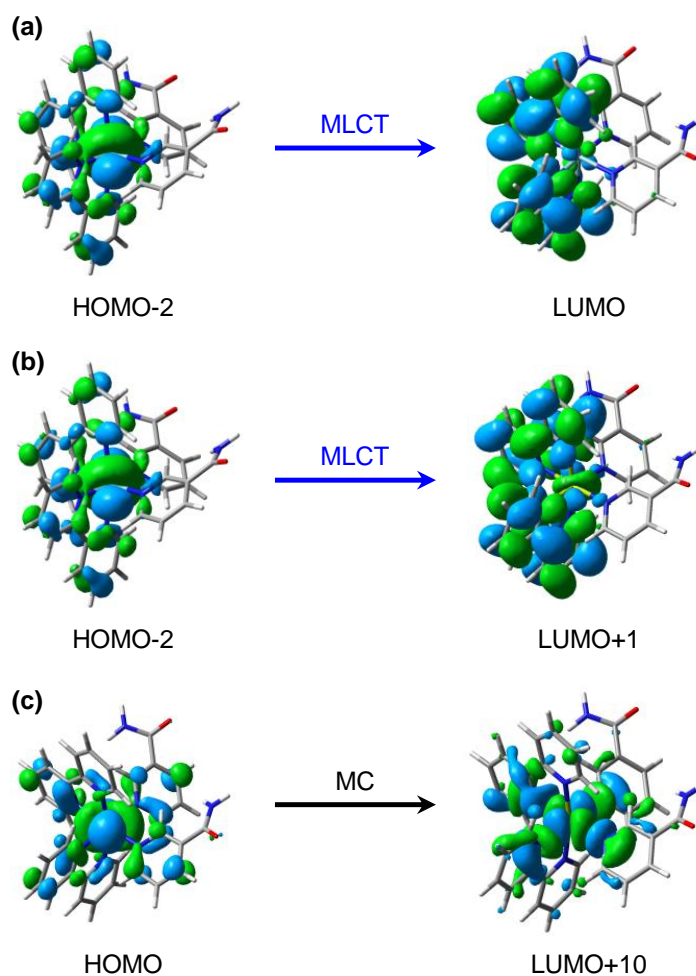


Figure C.1 | Calculated (major) orbital transitions associated with (a, b) the $^1\text{MLCT}/^3\text{MLCT}$ states and (c) $^1\text{MC}/^3\text{MC}$ states for complex **1** using the TD-B3LYP method – see Table C.1

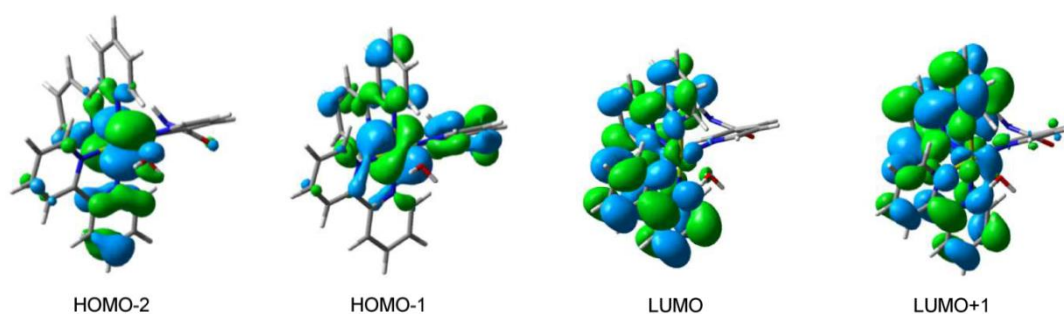


Figure C.2 | Calculated molecular orbital involved in the (major) orbital transitions associated with the $^1\text{MLCT}/^3\text{MLCT}$ states of the $\text{cis-}[\text{Ru}(\text{bpy})_2(\text{NA})(\text{H}_2\text{O})]^{2+}$ (**2**) photoproduct - see Table C.1 for details. Calculations were performed at the TD-B3LYP/cc-pVTZ-SDD level of theory.

Table C.1 | Calculated vertical excitation energies (ΔE), transition wavelengths and associated oscillator strengths (f) for significant triplet and singlet electronic excitation transitions in complexes **1** and **2**, using TD-B3LYP with an SDD 28 electron ECP (Ru) and cc-pVTZ (H, C, O and N) basis set. Major molecular orbital transitions and their relative contributions (%) to a given state are also provided (L = LUMO and H = HOMO) together with vertical energy differences (δE) between significant states in **1** (see Figure C.1 for orbital transitions in **1**). Central wavelengths for the experimentally observed absorption bands of **1** and **2**, assigned predominantly to the ‘bright’ $^1\text{MLCT}$ state(s), are also given (*cf.* Figure 4.1).

	State/Parameter			TD-B3LYP/cc-pVTZ-SDD (+H ₂ O PCM) ^b			Experiment
	Character	Transition ^a	% a	ΔE / eV	λ / nm	f	λ / nm
<i>cis</i> -[Ru(bpy) ₂ (NA) ₂] ²⁺ (1)	$^3\text{MLCT}$	L+1 \leftarrow H-2 (L+1 \leftarrow H-2)	56 (56)	2.64 (2.66)	470 (465)	-	~435
	$^3\text{MLCT}$	L \leftarrow H-2 (L \leftarrow H-2)	64 (64)	2.71 (2.73)	458 (454)	-	
	$^1\text{MLCT}$	L \leftarrow H-2 (L \leftarrow H-2)	65 (66)	2.90 (2.90)	428 (428)	0.0891 (0.1175)	
	^3MC	L+10 \leftarrow H (L+10 \leftarrow H)	58 (52)	2.94 (3.00)	422 (413)	-	
	$^1\text{MLCT}$	L+1 \leftarrow H-2 (L+1 \leftarrow H-2)	62 (62)	3.04 (3.04)	408 (408)	0.0487 (0.0782)	
	^1MC	L+10 \leftarrow H (L+10 \leftarrow H)	48 (48)	3.56 (3.61)	348 (343)	0.0024 (0.0077)	
		δE [$^1\text{MLCT}$ - $^3\text{MLCT}$]		0.19 (0.17)			
<i>cis</i> -[Ru(bpy) ₂ (NA)(H ₂ O)] ²⁺ (2)	$^3\text{MLCT}$	L \leftarrow H-2 (L \leftarrow H-2)	38 (41)	2.47 (2.46)	501 (502)	-	~470
	$^3\text{MLCT}$	L+1 \leftarrow H-1 (L+1 \leftarrow H-2)	61 (49)	2.53 (2.51)	490 (494)	-	
	$^1\text{MLCT}$	L \leftarrow H-2 (L \leftarrow H-2)	51 (49)	2.92 (2.86)	425 (433)	0.0974 (0.1294)	
	$^1\text{MLCT}$	L+1 \leftarrow H-1 (L+1 \leftarrow H-2)	42 (47)	3.03 (2.99)	409 (414)	0.0282 (0.0464)	

^aMajor orbital transition associated with electronic excitation. ^bAll values in parentheses are for TD-B3LYP/cc-pVTZ-SDD calculation results including a H₂O PCM.

Bibliography

- (1) Adamo, C.; Barone, V. *J. Chem. Phys.* **1999**, *110*, 6158.
- (2) Zhao, Y.; Truhlar, D. G. *J. Chem. Phys.* **2006**, *125*, 194101.
- (3) Yanai, T.; Tew, D. P.; Handy, N. C. *Chem. Phys. Lett.* **2004**, *393*, 51.
- (4) Becke, A. D. *J. Chem. Phys.* **1993**, *98*, 5648.
- (5) Stephens, P. J.; Devlin, F. J.; Chabalowski, C. F.; Frisch, M. J. *J. Phys. Chem.* **1994**, *98*, 11623.
- (6) McKinlay, R. G.; Paterson, M. J. *J. Phys. Chem. A* **2012**, *116*, 9295.
- (7) Dunning, T. H. *J. Chem. Phys.* **1989**, *90*, 1007.
- (8) Paterson, M. J.; Blancafort, L.; Wilsey, S.; Robb, M. A. *J. Phys. Chem. A* **2002**, *106*, 11431.
- (9) Worth, G. A.; Welch, G.; Paterson, M. J. *Mol. Phys.* **2006**, *104*, 1095.
- (10) Mckinlay, R. G.; Żurek, J. M.; Paterson, M. J. *Adv. Inorg. Chem.* **2010**, *62*, 351.
- (11) Żurek, J. M.; Paterson, M. J. *J. Phys. Chem. A* **2012**, *116*, 5375.
- (12) Żurek, J. M.; Paterson, M. J. *J. Chem. Phys.* **2012**, *137*, 034308.
- (13) Gaussian 09, Revision A.02, Frisch, M. J.; Trucks, G. W.; Schlegel, H. B.; Scuseria, G. E.; Robb, M. A.; Cheeseman, J. R.; Scalmani, G.; Barone, V.; Mennucci, B.; Petersson, G. A.; Nakatsuji, H.; Caricato, M.; Li, X.; Hratchian, H. P.; Izmaylov, A. F.; Bloino, J.; Zheng, G.; Sonnenberg, J. L.; Hada, M.; Ehara, M.; Toyota, K.; Fukuda, R.; Hasegawa, J.; Ishida, M.; Nakajima, T.; Honda, Y.; Kitao, O.; Nakai, H.; Vreven, T.; Montgomery, J. A., Jr.; Peralta, J. E.; Ogliaro, F.; Bearpark, M.; Heyd, J. J.; Brothers, E.; Kudin, K. N.; Staroverov, V. N.; Kobayashi, R.; Normand, J.; Raghavachari, K.; Rendell, A.; Burant, J. C.; Iyengar, S. S.; Tomasi, J.; Cossi, M.; Rega, N.; Millam, N. J.; Klene, M.; Knox, J. E.; Cross, J. B.; Bakken, V.; Adamo, C.; Jaramillo, J.; Gomperts, R.; Stratmann, R. E.; Yazyev, O.; Austin, A. J.; Cammi, R.; Pomelli, C.; Ochterski, J. W.; Martin, R. L.; Morokuma, K.; Zakrzewski, V. G.; Voth, G. A.; Salvador, P.; Dannenberg, J. J.; Dapprich, S.; Daniels, A. D.; Farkas, Ö.; Foresman, J. B.; Ortiz, J. V.; Cioslowski, J.; Fox, D. J.; Gaussian, Inc., Wallingford CT, 2009.
- (14) Gaussian 03, Revision D.01, Frisch, M. J.; Trucks, G. W.; Schlegel, H. B.; Scuseria, G. E.; Robb, M. A.; Cheeseman, J. R.; Montgomery, Jr., J. A.; Vreven, T.; Kudin, K. N.; Burant, J. C.; Millam, J. M.; Iyengar, S. S.; Tomasi, J.; Barone, V.; Mennucci, B.; Cossi, M.; Scalmani, G.; Rega, N.; Petersson, G. A.; Nakatsuji, H.; Hada, M.; Ehara, M.; Toyota, K.; Fukuda, R.; Hasegawa, J.; Ishida, M.; Nakajima, T.; Honda, Y.; Kitao, O.; Nakai, H.; Klene, M.; Li, X.; Knox, J. E.; Hratchian, H. P.; Cross, J. B.; Bakken, V.; Adamo, C.; Jaramillo, J.; Gomperts, R.; Stratmann, R. E.; Yazyev, O.; Austin, A. J.; Cammi, R.; Pomelli, C.; Ochterski, J. W.; Ayala, P. Y.; Morokuma, K.; Voth, G. A.; Salvador, P.; Dannenberg, J. J.; Zakrzewski, V. G.; Dapprich, S.; Daniels, A. D.; Strain, M. C.; Farkas, O.; Malick, D. K.; Rabuck, A. D.; Raghavachari, K.; Foresman, J. B.; Ortiz, J. V.; Cui, Q.; Baboul, A. G.; Clifford, S.; Cioslowski, J.; Stefanov, B. B.; Liu, G.; Liashenko, A.; Piskorz, P.; Komaromi, I.; Martin, R. L.; Fox, D. J.; Keith, T.; Al-Laham, M. A.; Peng, C. Y.; Nanayakkara, A.; Challacombe, M.; Gill, P. M. W.; Johnson, B.; Chen, W.; Wong, M. W.; Gonzalez, C.; and Pople, J. A.; Gaussian, Inc., Wallingford CT, 2004.